ΕΘΝΙΚΟ ΜΕΤΣΟΒΙΟ ΠΟΛΥΤΕΧΝΕΙΟ
Εργαστήριο Ατμοκινητήρων & Λεβήτων
Τομέας Θερμότητας της Σχολής Μηχανολόγων Μηχανικών

ΔΙΠΛΩΜΑΤΙΚΗ ΕΡΓΑΣΙΑ

Techno-economic assessment of solar driven Organic Rankine Cycle using medium to high grade heat sources, with the use of a genetic algorithm optimization

Τεχνο-οικονομική αξιολόγηση ηλιακά τροφοδοτούμενου Οργανικού Κύκλου Rankine για πηγές θερμότητας μέσης και υψηλής θερμοκρασίας μέσω γενετικού αλγορίθμου βελτιστοποίησης

Του Φοιτητή
Νικολάου Α. Φωστιέρη

Επιβλέπων

Καρέλλας Σωτήριος, Καθηγητής,
Σχολή Μηχανολόγων Μηχανικών, ΕΜΠ

Αθήνα, Σεπτέμβριος 2019

Περίληψη

Δεδομένων των αυξανόμενων περιβαλλοντικών ανησυχιών γύρω από τις συμβατικές τεχνολογίες παραγωγής ενέργειας από ορυκτά καύσιμα καθίσταται επιτακτική η ανάγκη αύξησης της εισχώρησης των ανανεώσιμα εκκινούμενων αποκεντρωμένων συστημάτων. Προς αυτήν την κατεύθυνση, η ηλιακή ενέργεια αποτελεί μια άκρως ανταγωνιστική επιλογή, δεδομένης της αφθονίας της σε πολλές περιοχές.

Η εν λόγω μελέτη πραγματεύεται την σύζευξη του οργανικού κύκλου Rankine με την ηλιακή ενέργεια για εφαρμογές μικρής κλίμακας, μέσης και υψηλής θερμοκρασίας. Στόχος της μελέτης είναι η βελτιστοποίηση της διάταξης και η αξιολόγηση της ενεργειακής και οικονομικής απόδοσης του συστήματος για πιθανή εφαρμογή σε πέντε ευρωπαϊκές πόλεις. Η βελτιστοποίηση πραγματοποιήθηκε με τη χρήση ενός γενετικού αλγορίθμου πολλαπλών στόχων.

Σύμφωνα με τα αποτελέσματα, οι παραβολικοί δίσκοι επιτυγχάνουν την βέλτιστη ενεργειακή επίδοση, ενώ οι συλλέκτες παραβολικού κατόπτρου εμφανίζουν τη βέλτιστη οικονομική απόδοση. Η μέγιστη ενεργειακή απόδοση που καταγράφηκε από τη βελτιστοποίηση ήταν της τάξης του 10.5%-11.0% για βορειότερες περιοχές, με βέλτιστα εργαζόμενα μέσα το κυκλοπεντάντιο και το κυκλοεξάνιο. Από την άλλη πλευρά, αναφορικά με την οικονομική απόδοση, το κόστος της παραγόμενης ενέργειας ελαχιστοποιείται για τις νοτιότερες περιοχές, λόγω και του υψηλού ηλιακού δυναμικού αυτών, παραμένοντας ωστόσο σχεδόν 1.5 φορά μεγαλύτερο από το τρέχον κόστος πώλησης της ηλεκτρικής ενέργειας.

Abstract

Given the rising environmental concerns towards the fossil fuel-based power technologies, there is a growing need for an increased penetration of renewable driven decentralized systems. Within this scope, solar energy is a competitive solution thanks to its abundance.

This study discusses the coupling of solar energy with Organic Rankine Cycle (ORC) for low scale applications at medium to high temperature grade. The goal of this assessment was to optimize the configuration and evaluate its energetic and economic performance in five different European cities.

The system optimization was conducted based on a multi-objective genetic algorithm. Parabolic Dish Collectors (PDCs) yield higher energy efficiency, whereas Parabolic Trough Collectors (PTCs) are linked to financially more profitable results. The maximum total energy efficiency in an annual base was around 10.5%-11% for northern locations with Cyclopentane and Cyclohexane to be the best performing working fluids. On the other hand, with respect to system economics, the cost of the produced energy is minimized for southern locations with the minimum value to be at least around 1.5 times higher than the current commercial cost of energy.

Preface

By submitting my Undergraduate Thesis and therefore completing my studies at the National Technical University of Athens, I would like to thank the people that helped me during the period of my studies.

Firstly, I would like to thank my Thesis Supervisor, Professor Sotirios Karellas, for his tutoring and for the cooperation we had during the final semester. Additionally, I would like to thank PhD candidate Tryfon Roumpedakis for his guidance throughout the semester and for offering me quality feedback, at every stage of this study.

Finally, I would also like to acknowledge the people who were close to me during these years and mostly I would like to thank my family for supporting me and providing me with everything necessary, throughout my studies and during my lifetime in general.

Table of contents

List of Figures

List of Tables

Nomenclature

A	*Surface*	$[m^2]$
C	*Cost*	[€]
C_p	*Specific heat*	$[J/kgK]$
D	*Diameter*	$[m]$
D_h	*Hydraulic diameter*	$[m]$
Ex	*Exergy*	$[W]$
ff	*Filling factor*	$[-]$
G	*Mass velocity*	$[kg/m^2s]$
H	*Height*	$[m]$
h	*Specific enthalpy*	$[J/kg]$
I	*Direct irradiance*	$[W/m^2]$
i	*Discount rate*	[%]
k	*Thermal conductivity*	$[W/mK]$
L_{loc}	*Longitude*	$[deg]$
L_{st}	*Longitude of the standard time meridian*	$[deg]$
M	*Mass*	$[kg]$
$\dot{m}$	*Mass flow rate*	$[kg/s]$
N	*Rotational speed*	$[rpm]$
n	*Investment lifetime*	$[years]$
Nu	*Nusselt number*	$[-]$
p	*Pressure*	$[Pa]$
Pr	*Prandlt number*	$[-]$
Q	*Power*	$[W]$
Re	*Reynolds number*	$[-]$
r_p	*Pressure ratio*	$[-]$

s	*Specific entropy*	$[J/kgK]$
T	*Temperature*	$[K]$
U_l	*Heat loss coefficient*	$[W/m^2K]$
V	*Volume*	$[m^3]$
$\dot{V}$	*Volumetric flow rate*	$[m^3/s]$
V_s	*Volumetric displacement*	$[m^3/rev]$
W	*Work*	$[W]$
x	*Dryness*	$[-]$

Greek Symbols

a	*Heat transfer coefficient*	$[W/m^2K]$
β	*Tilt angle*	$[deg]$
η	*Efficiency*	$[-]$
θ	*Incidence angle*	$[deg]$
ξ	*Darcy's friction coefficient*	$[-]$
ρ	*Density*	$[kg/m^3]$
τ	*Torque*	$[Nm]$
φ	*Latitude*	$[deg]$

Subscripts

amb	*Ambient*
b	*Direct*
c	*Cold*
ch	*Channel*
col	*Collector*
$cond$	*Condenser*
el	*Electrical*
$evap$	*Evaporator*
exp	*Expander*

f	*Working fluid*
gen	*Generator*
h	*Hot*
i	*Hour value*
in	*Inlet*
$iorc$	*Intermediate ORC system*
is	*Isentropic*
$mech$	*Mechanical*
n	*Perpendicular*
nom	*Nominal*
$pump$	*Pump*
rec	*Recuperator*
sol	*Solar*
st	*Storage tank*
sub	*Subcooling*
sup	*Superheating*
T	*Tilted*
th	*Thermal*

Abbreviations

$CAPEX$	*Capital Expenditures*
HTF	*Heat Transfer Fluid*
$LCoE$	*Levelized Cost of Energy*
$OPEX$	*Operating Expenses*
ORC	*Organic Rankine Cycle*
PDC	*Parabolic Dish Collectors*
PTC	*Parabolic Trough Collectors*

Chapter 1. Introduction

1.1. Water-steam Rankine cycle

The thermodynamic Clausius-Rankine cycle is the main cycle model used in power generation applications. The largest part of the world's energy is produced through this water-steam power cycle [1].

The fluid used in the cycle is water, which in the cycle's simplest configuration undergoes four basic processes as is shown in the figure below.

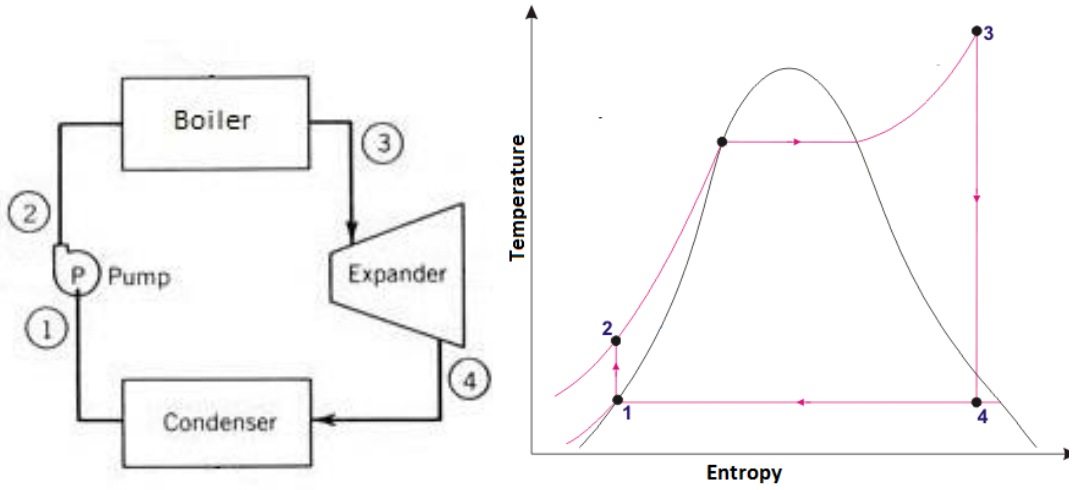

(a) (b)

Figure 1.1: (a) Ideal Rankine cycle and (b) the corresponding Temperature-entropy (T-s) diagram

Following the numbering of the above figure, the processes that constitute the ideal Rankine cycle are [2]:

- Process 1-2: Isentropic compression. The saturated water which corresponds to point 1 (Figure 1.1), is in state of low temperature and pressure and enters the pump in which this process takes place. The pump raises the pressure of the working fluid, exiting as subcooled water and with a temperature slightly higher than the previous one (excessively shown in the figure). This process requires an energy input, in order for the pump to operate, which may be considered negligible compared to the energy input of process 2-3.
- Process 2-3: Isobaric heating. The high-pressure subcooled water flows towards the boiler where the heating step takes place. The boiler is in fact a heat exchanger which can be divided in three parts [3]. At first in the Economizer the water is being preheated until it reaches its liquid saturated state. Then, in the Evaporator the saturated water absorbs the required amount of latent heat, in a process of constant temperature, until it reaches a saturated vapor state. Finally, in the Superheater the saturated vapor is being superheated up to the desired temperature which

corresponds to the point 3 in Figure 1.1. The heat supplied to the boiler by the combustion of the fuel is the energy input of the cycle.

- Process 3-4: Isentropic expansion. The superheated vapor (point 3) enters the steam turbine to be expanded. The steam turbine reduces the temperature and the pressure of the working fluid producing mechanical work on its shaft which is then converted into electricity by the coupled generator. The exit of the turbine is a water and steam mixture of low moisture content (point 4), whereas in some cases it is possible to remain in condition of superheated steam.
- Process 4-1: Isobaric condensation. The exiting stream from the expander is supplied to the condenser where the working fluid returns to its initial state of saturated liquid (point 1) in order for the cycle to complete. The condenser, similarly to the boiler, is a heat exchanger in which the water steam mixture is cooled by a secondary cooling circuit (usually water) and the heat is eventually rejected to the environment via a cooling tower.

The aforementioned processes form the ideal Rankine cycle. However, the working cycle applied in real thermal plants does not consist of ideal reversible processes [1]. As a result, the compression and the expansion (processes 1-2 and 3-4) are not isentropic, but can be studied by taking into consideration the isentropic efficiency of the pump and the turbine, respectively. Furthermore, the isobaric heat exchange in the boiler and the condenser (processes 2-3 and 4-1) are not performed in a constant pressure, as in both cases a pressure drop takes place, dependent on the design and the function of its components.

As mentioned, this is the conventional configuration of the water-steam Rankine cycle, which in most cases is modified properly to enhance its thermal efficiency. The improvements concern the alteration of the thermodynamic characteristics of the water and steam in each stage and can be achieved either by changing the working conditions or by adding auxiliary components to the plant.

The main modification that increases the efficiency is the elevation in the mean temperature of the working fluid during the heating step (process 2-3) [3]. This temperature level can be raised by increasing the temperature of the steam that exits the superheater (point 3) as it is shown below in Figure 1.2a. However, the highest temperature that the produced vapor can reach is limited by the durability of the turbine's blades' materials.

Alternatively, the mean heating temperature can be raised by increasing the pressure ratio of the compression performed by the pump as shown on Figure 1.2b. This can be achieved by augmenting the pressure of the working fluid inside the boiler which leads to an increased enthalpy drop and thus a higher energy production. It can also be attained by reducing the condensation pressure which leads to the reduction of the heat that is rejected to the environment.

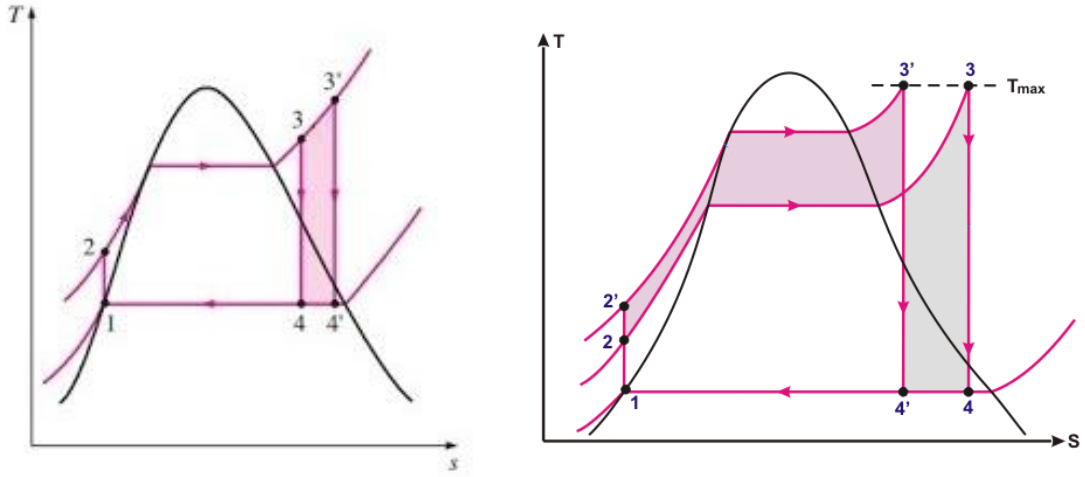

(a) (b)

Figure 1.2: Temperature-entropy (T-s) diagram of improved Rankine cycle with (a) higher final temperature and (b) higher final pressure

Finally, the cycle's efficiency can be improved by additional plant components. The most common practices include steam reheating and liquid water preheating. In the first case, the superheated vapor is partly expanded in the turbine up to a specific pressure and then is reheated until it reaches a temperature close to the superheating temperature. After that, it is fully expanded up to the low pressure of the cycle. In the preheating a small part of the expanded steam is used to raise the temperature of the feeding water reducing in that way the required heat input supplied to the economizer. The processes that take place in a modified cycle can be observed in the Figure 1.3 below, in which the working fluid is preheated in two stages and also reheated.

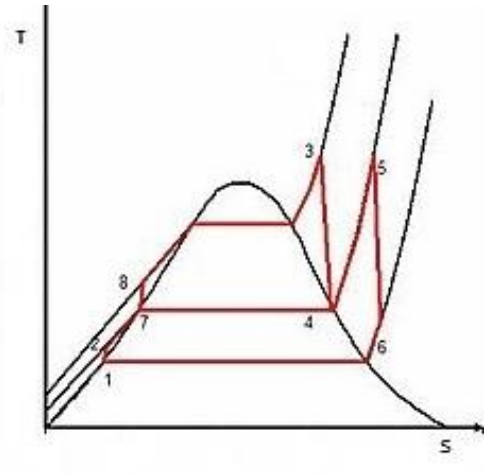

Figure 1.3: Temperature-entropy (T-s) diagram of improved Rankine cycle with reheating and preheating

In a conventional steam Rankine cycle the operating conditions that characterize its function are the low and the high pressures and the maximum temperature of the water. Typical values for the high pressure are around 150 bar (in some applications of supercritical cycle it can go up to 300 bar), whereas the low pressure can sink up to 0.01 bar. Regarding the temperature of the vapor entering the turbine there is an upper limit set at about 600 ^{o}C [4]. Concerning the efficiency of these plants, most of them are operating within a range of 33-40%, whereas some modern plants may reach efficiencies of up to 45% [4].

1.2. Organic Rankine cycle

A modification of the Rankine cycle can be applied in many cases, by using a different working fluid instead of water. The cycle that uses organic fluids and performs the basic processes of the Clausius-Rankine cycle is called Organic Rankine Cycle (ORC). The ORC's main advantages against the conventional steam Rankine Cycle are its flexibility and its capacity to exploit various energy sources of wide temperature range. In that way, it is possible to exploit low and medium temperature heat sources and develop small scale decentralized plants that produce electricity, heat or cooling [2].

The principles applied in ORC are the same as described above. A liquid is pumped from the low to the high pressure and is then directed to a heat exchanger. There, heat is transferred to the fluid which vaporizes, however without reaching the highly superheated condition of the steam in the regular Rankine cycle. After the evaporator the working fluid enters an expander in which it releases its energy to produce mechanical work, which subsequently is converted to power. The configuration of the ORC plant is simpler than the conventional steam cycle, in which the most common additional component used is a recuperator after the expander to preheat the feeding liquid entering the evaporator, as illustrated in the figure below [5].

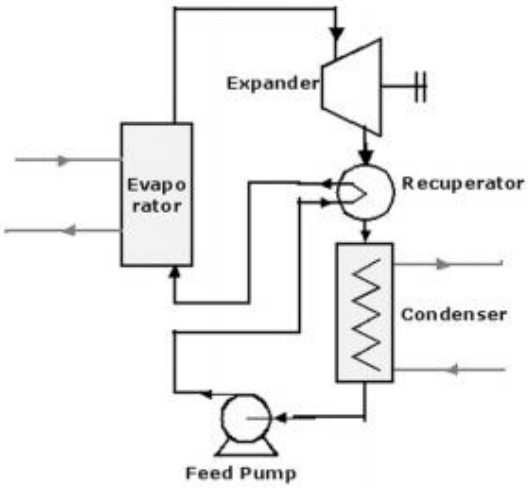

Figure 1.4: ORC system with recuperator [5]

The ORC technology is highly developing lately due to its contribution to the minimization of the CO_2 emissions in the energy sector. The restrictions on the release of greenhouse gases in the atmosphere encourage the decrease of the total power consumption deriving from fossil fuels. This can be achieved by shifting the power production to industries by using their exhaust gases or to individual energy producers for local consumption (through combined heat and power generation), as well as by reinforcing the power production based on renewable energy sources [5].

The total installed capacity of ORC plants is estimated around 2.7-3 GW distributed in bigger and smaller autonomous units worldwide [6]. The majority of these are driven from geothermal plants, heat recovered from exhaust gases (waste heat recovery), small-scale biomass powered units and Concentrated Solar Power (CSP) systems. The evaporation temperature and the critical point of the used organic fluids are much lower compared to the corresponding characteristics of the steam, decreasing the required temperature to perform the fluid's evaporation [7]. Thus, with the ORC it is technically and financially feasible to use lower temperature heat sources which could not be used efficiently in the water-steam cycle.

The largest portion of the ORC market belongs to the geothermal plants that can be developed also as multi-MW large-scale plants [6]. Moreover, residual hot gases that until now remain unused and are rejected to the environment as thermal losses from gas turbines, diesel engines and industrial thermal processes (e.g. in cement, petrochemical industry, metallurgy) could be a potential heat source for an ORC system, increasing in that way the total power production or covering the energy needs of the industrial process. Finally, power production in ORC systems can be realized via biomass driven plants [7].

Concerning the CSP systems, they consist of a number of concentrated solar collectors coupled with an ORC system. The concentrated collectors, contrariwise to the commonly used in domestic applications static collectors, direct the solar irradiance to a specific surface or point which absorbs it as a whole. In that way, they can reach medium and high temperature levels (higher than 150 ^{o}C and in some specific cases can go up to 1200 ^{o}C) [8]. The cycle can be adjusted for a wide range of temperatures, by selecting the appropriate working fluid that optimizes the thermodynamic behavior of the unit [9].

Parabolic troughs, parabolic dish, solar tower systems, and even linear Fresnel collectors which work in a lower temperature interval can be used [5, 8]. The collected irradiance from the collectors is used in order to heat up the organic fluid either directly in a direct vapor generation (DVG) system, or by using an intermediate fluid to transfer the heat to the working fluid of the cycle (HTF system) [9]. The latter configuration can be used also as a method to store heat during the day, in a thermal storage tank, and to prolong the operating time of the solar driven ORC system during the night as well [7].

1.2.1 Working fluids

The selection of the working fluid used in an ORC system is one of its most crucial characteristics that needs to be taken into consideration in order to match the thermodynamic needs of the unit and achieve the maximum thermal efficiency.

The main categorization of the organic fluids is done based on the slope of the saturated vapor line on the Temperature-entropy (T-s) diagram [9]. The organic substances that have a negative value of this slope have a T-s diagram similar to the water's. In general they have lower molecular mass [10] and are characterized as "wet fluids". Others that have a nearly vertical saturated vapor curve and moderate molecular mass are known as "isentropic fluids", whereas fluids with a positive slope and a higher molecular mass are classified as "dry fluids", as shown below in Figure 1.5.

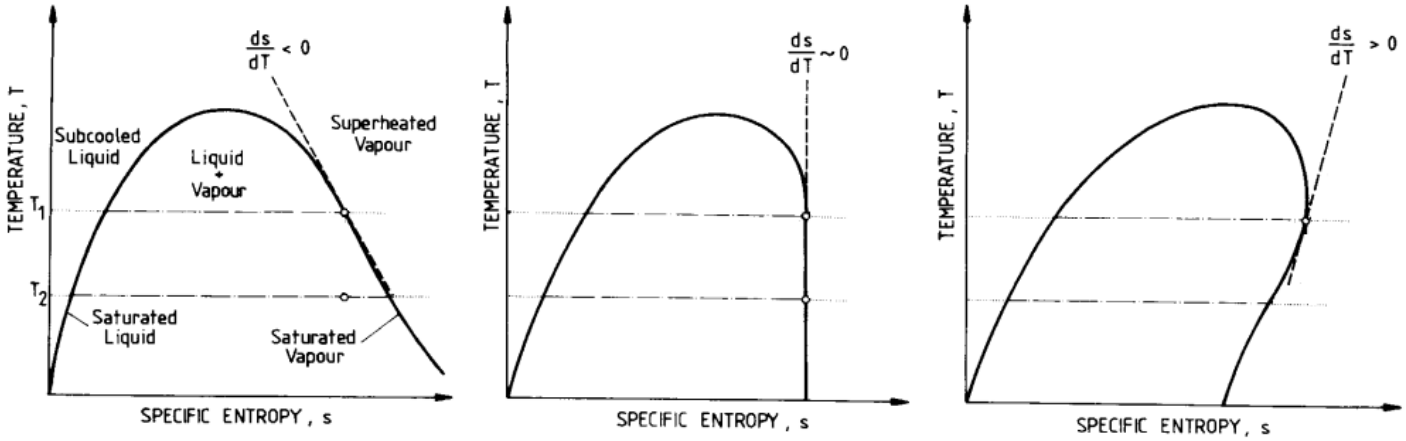

(a) (b) (c)

Figure 1.5: Classification of organic working fluids based on their Temperature-entropy (T-s) diagram (a) wet (b) isentropic and (c) dry fluid [11]

The main difference between these working fluids is their behavior in the expansion process, which affects the state of the produced vapor. As it can be observed in the above figure, in case of a dry fluid in a state of saturated vapor, the expansion process ends in a state of superheated vapor, meaning that inside the expander there is at no point a mixture of liquid and vapor. The same conclusion can be deduced in case the fluid is isentropic and enters the expander in a state of saturated or slightly superheated vapor. However, in a wet fluid, the expansion of a saturated vapor ends in a state of liquid-vapor mixture, where there have formed droplets of liquid, which affect the function of the expander and decrease its efficiency and durability [10]. Taking into consideration that the minimum dryness fraction at the outlet of the turbine is 85% [11], it is necessary in case of wet working fluids to superheat the produced vapor in order to avoid high liquid fractions inside the expander. As a result, ORC systems with wet fluids should be coupled with high temperature heat sources.

The selection of the most suitable working fluid takes into consideration many parameters that have to do not only with its thermodynamic behavior, but also with its chemical structure, its physical and environmental properties.

Concerning the thermodynamic efficiency, the fluid's critical point, as well as its evaporation point are two of the most important properties that need to be taken into account. The thermal efficiency of the ORC is maximized at the affinity of the critical point [10]. Thus, depending on the available heat source and its temperature level, the fluids that are expected to correspond better can be defined.

Another thermodynamic characteristic of the fluid is the width of its T-s curve and hence the entropy difference between the saturated liquid and vapor [5]. The wider the curve, the higher the vaporization enthalpy leading to higher latent heat, which means that more energy can be absorbed by the fluid, minimizing in that way the size of the installation [7].

Another aspect of key importance is the fluid's vapor density. A fluid that has lower vapor density leads to higher volume flow rates and subsequently increases the size of the components, which augments the cost of the unit as well [5, 10]. Additionally, desired properties of an organic fluid are the low viscosity and the high thermal conductivity. In that way, the pressure losses in the heat exchangers due to friction are decreased, whereas the heat transfer coefficient is higher, reducing the size and thus the overall costs.

One of the most important parameters during the selection process is the environmental behavior of the organic fluids. The key concerns inherent with the use of organic fluids is the depletion of the ozone layer and the global warming. In order to classify the organic fluids with respect to the aforementioned issues there are two indexes, the Ozone Depleting Potential (ODP) and the Global Warming Potential (GWP). The first one expresses the degradation to the ozone layer caused by the fluid and the latter the heat that these greenhouse gases trap in the atmosphere compared to the corresponding value caused by CO_2 [5, 10]. Finally, there are certain restriction regarding the fluids' safety. That concerns their flammability and toxicity, in order to prevent health risks or any kind of accident in case of leakage [10].

Finally, apart from pure substances, an alternative is the substitution of the organic fluids with zeotropic mixtures. These mixtures perform their phase change under variable temperature, keeping although their pressure constant as it is observed in the Figure 1.6 [11]. This property reduces the temperature difference between the two streams in the heat exchangers (evaporator and condenser) and hence increases the exergetic efficiency of the system [10].

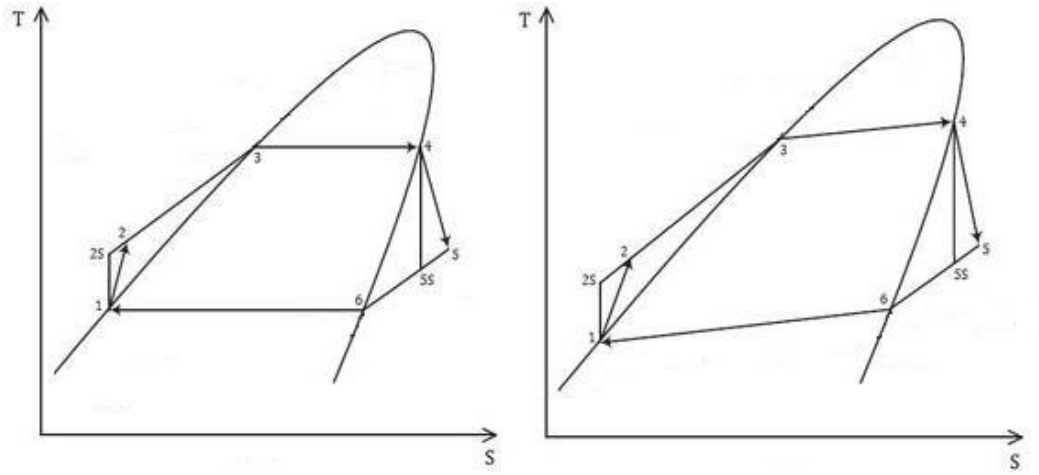

(a) (b)

Figure 1.6: Comparison of ORC working with (a) pure organic fluid and (b) azeotropic mixture [12]

Given the above, it is obvious that the selection of the working fluid is an additional parameter that needs to be determined in the configuration of the thermodynamic cycle. Hence, it inserts a degree of freedom in the technical implementation of the unit that does not exist in the conventional Rankine cycle [13]. In that way, the ORC systems become more easily adjustable to the available heat sources facilitating at the same time the selection of their components.

1.2.2 Supercritical cycle

Apart from the already described sub-critical cycle, the supercritical ORC is an alternative with high thermodynamic interest, which has been investigated as an alternative that could be also applied in heat sources of higher temperature level.

The difference of this cycle is that the fluid reaches a higher-pressure level and the heating process takes place at a state that exceeds its critical point as shown in Figure 1.7. As a result, during the heat transfer from the source to the organic fluid, the latter does not undergo a phase change in which it evaporates gradually, as happens in the subcritical cycle, but the state changes from liquid to supercritical fluid when it reaches a pseudo-critical temperature, around which its thermodynamic properties vary vastly depending on the temperature and pressure [14, 15]. The supercritical cycle is executed much easier in an ORC compared to the conventional water-steam cycle, because the water's critical point is at around 220 bar, whereas for organic fluids this value could be at around 50 bar. Hence, the material's durability issues are less in ORC and the performance of the key components is rather stable and efficient.

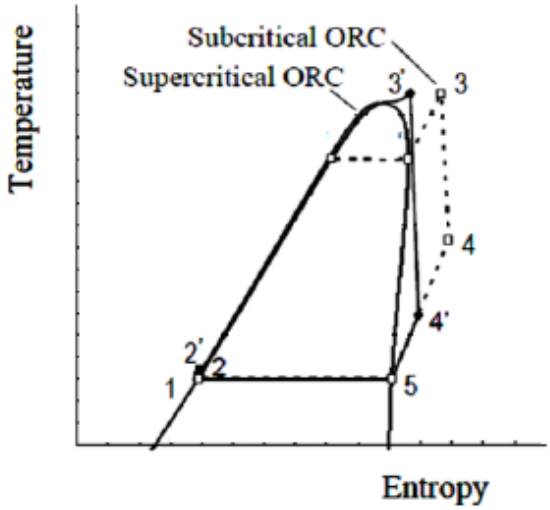

Figure 1.7: Temperature-entropy diagram for sub- and super-critical ORC

The main advantage that this alternative offers is the higher thermal efficiency that can be achieved. As it can be observed from the figure above, the mean temperature in which the heating process takes place is higher in a supercritical cycle, which leads to lower temperature difference between the two streams inside the heat exchanger and thus to lower exergy destruction and higher thermal and exergetic efficiency [15, 16].

However, the implementation of one such system requires several modifications in the selection of its components. The main difference with the subcritical unit includes the heat exchangers design which due to the higher applied pressures needs to be more robust to withstand the developed stresses. Another aspect that should be taken into consideration is its thermal efficiency. Because of the aforementioned lower temperature difference of the two streams, heat is not transferred so efficiently to the working fluid compared to the subcritical cycle requiring a larger heat transfer area. These two factors increase the cost of the whole unit. Karellas et al. [15] in a study for a supercritical ORC that uses waste heat, concluded that the rise of the installation costs is not disproportional to the rise of the plant's efficiency.

Therefore, the supercritical cycle is an alternative that should be examined in order to optimize the unit from a techno-economic viewpoint. Because of the higher temperature of the fluid throughout the heating process, it is an option mainly for heat sources that have the capacity to transfer heat at a higher temperature.

1.3. Bibliographic review of studies on ORC

The last years there has been a lot of research on the energy field, investigating various alternative methods for energy production, cogeneration and mainly the exploitation of renewable energy sources. Many studies focus on ORC systems driven by various energy sources. Below there is a brief review of some notable theoretical assessments on solar ORC plants of medium and/or high grade [8].

Delgado-Torres and Garcia Rodriguez [9] performed a theoretical analysis on the performance of an ORC supplied by the heat of stationary solar panels. They investigated the efficiency of the unit considering twelve different working fluids, three types of collectors (FPC, CPC, ETC) for both cases of heat transfer (DVG and HTF) and for two configurations with and without the use of a regenerator. They concluded that, as expected, the maximum efficiency can be reached in a DVG system that includes a regenerator. For each type of collector, the fluid that provides the optimum thermal efficiency was identified as well as the overall optimum of all the alternative scenarios. This consists of evacuated tube collectors (ETC) coupled with isopentane as a working medium. This configuration had as evaporation and condensation temperatures 129 ^{o}C and 30 ^{o}C, respectively. Considering a total solar irradiance equal to G=1000 W/m^2, the proposed system achieved a thermal efficiency equal to 16.4% and an overall solar efficiency up to 8.51%.

Solar power as a heat source for ORC systems has been also highly investigated in case of the development of seawater desalination systems. Delgado-Torres and Garcia Rodriguez have examined alternative ORC configurations in order to implement this type of systems, focusing on a medium temperature interval, which have also been used by Penate et al. [17] in order to be coupled with the desalination unit.

The plant [18, 19] consists of a simple ORC cycle in which several types of fluids were examined, with evaporation temperatures between 235-300 ^{o}C and a maximum cycle temperature up to 400 ^{o}C. Similar to the previous studies, the thermal and the total solar efficiency was calculated in two configurations of a DVG system with/without regenerator. Additionally, the solar collectors used for the model were parabolic trough collectors (PTCs) of two different types receiving a direct solar irradiance equal to G_b=850 W/m^2. The results were extracted for multiple maximum cycle temperatures starting from zero superheating up to a superheating of around 100 ^{o}C. The main conclusion concerning the efficiency improvement methods was that the introduction of a regenerator increased the thermal efficiency around 20% much higher than the increase caused by a vapor superheating of 100^{o}C, which offered an increase of around 14%. The accumulating results show an optimum value of the thermal efficiency for toluene as working fluid and a maximum cycle temperature of 380 ^{o}C, while the corresponding condensation temperature is 35 ^{o}C. The achieved cycle efficiency is 31.78%, whereas the total solar efficiency is equal to 22.35%.

They further examined this system with the same characteristics but applying a conventional HTF system instead of the DVG [20]. The results were similar to their previous work with a slight decrease in the maximum temperature due to the intermediate heat transfer system. The optimal result reached a thermal efficiency of 30.3% and a corresponding total solar efficiency of 20.58%, achieved for a maximum temperature equal to 337.3 ^{o}C.

Bruno et al. [21] developed a model of a solar driven ORC aiming at optimizing the thermal efficiency of the system. The designed plant included a regenerator and the case studies involved the utilization of three types of collectors, FPCs, ETCs and PTCs receiving a total mean solar radiance equal to G=800 W/m^2. However, due to the low outlet temperature of the first two, the authors focused mainly on the PTCs, which also gave the best results. The optimization process intended to define the appropriate level of superheating that increased the cycle efficiency adequately so as to compensate the decrease in the efficiency of the solar collectors. By evaluating several possible working fluids, the review concluded that the optimal total efficiency was equal to 21.44%, whereas the cycle's efficiency equal to 32.19%. These values were reached by using N-propylbenzene as working medium at a maximum cycle temperature equal to 377.3 ^{o}C.

Quoilin et al. [22] performed also a theoretical investigation on a solar ORC system using parabolic trough collectors (PTCs). They examined the thermodynamic behavior of a plant using a recuperator and an intermediate fluid for heat transfer, which received total solar irradiance equal to G=800 W/m^2. Due to the tradeoff between the cycle's and the collectors' efficiency, they defined the optimal final temperature of the cycle and performed the simulation in an interval around this temperature for four fluids. The final results showed a maximum overall efficiency for Solkatherm (SES36), with a maximum temperature of 169 ^{o}C. The cycle's efficiency is 13.1%, whereas the overall 7.9%. However, this fluid requires the highest expander swept volume which leads to bigger components and thus increases the overall cost of the unit. Hence, they concluded that from a techno-economic aspect the most profitable alternative is R245fa, which had an ORC efficiency equal to 11.2% and a total 6.9%.

Desai et al. [23] analyzed a solar driven ORC system, by examining two alternative configurations concerning the type of the used collectors. They developed two theoretical models of a regenerative ORC, utilizing linear Fresnel linear reflectors (LFRs) and PTCs and assuming that the received irradiance corresponds to the solar data of India. The comparison of the working fluids was conducted by examining twelve possible fluids and by fixing the maximum temperature of the cycle. In the case of LFR the fluid entered the turbine as saturated liquid with temperature equal to 170 ^{o}C, whereas for the PTC system it was superheated up to 210 ^{o}C. In terms of thermodynamics, the optimal efficiency was achieved using toluene and was equal to 19.21% for the LFR and 20.97% for the PTC, respectively. However, the optimization procedure took under consideration financial factors as well, and thus based on the levelized cost of energy (LCoE), the most appropriate choice was R113, with efficiency equal to 17.68% and 20.07% respectively.

Pikra et al. [24] focused on developing a model for power production through a CSP system with PTCs, designed to be implemented at remote areas in Indonesia. The system consists of the collectors which transfer heat to an intermediate thermal tank, used as thermal storage,

and then via a HTF system to the ORC. They chose from four alternative fluids based on their thermodynamic properties and concluded that for evaporation pressure equal to 10.18 bar and condensing temperature equal to 40 ^{o}C the most suitable medium is R123. For a mean solar irradiance equal to G=324 W/m^2, the maximum evaporation temperature reached up to 200 ^{o}C and the thermal efficiency achieved was 10.63%, whereas the respective solar efficiency was 4.67%.

Calise et al. [25] worked on an innovative solar ORC system which uses evacuated tube solar collectors (ETCs) in order to reach operating temperatures that are usually achieved with concentrating collectors. The unit included a regenerative cycle using an intermediate thermal storage tank which via a HTF system drives the ORC. The authors simulated the annual behavior of the system and its efficiency taking into consideration the fluctuations in the available solar radiation throughout the year, using meteorological data for the city of Naples. The ORC working with n-pentane as organic fluid yielded a thermal efficiency varying between 9-10%, depending on the maximum temperature of the oil which reached up to 180-230 ^{o}C respectively.

Patil et al. [26] evaluated the thermal and economic performance of a concentrating solar ORC unit with thermal storage. They studied a plant based on PTCs which transferred the absorbed heat to a thermal energy storage (TES) system and subsequently through a glycerol HTF to the working fluid. They selected the medium which corresponds better to the maximum temperature of the cycle and at the same time minimizes the overall cost of the unit. The selected fluid is isobutane and enters the expander with maximum temperature and pressure equal to 270 ^{o}C and 60 bar respectively, achieving a thermal ORC efficiency equal to 20.3%.

Another simulation of a solar driven system using concentrating PT collectors, was executed by Chacartegui et al. [27]. They focused on two different layouts based on the intermediate heat transfer circuit. The first one, characterized as direct uses the same oil as HTF and storage medium, whereas the indirect one utilizes two different fluids for the thermal storage and transfer. Based on the developed temperature on the solar collectors, the authors did a screening of the available fluids and finally selected and analyzed the cycle with three alternatives, that had the required critical temperature and thermal stability on the desired range. For each of these fluids they examined the efficiency with and without superheating the produced vapor, as well as including a recuperator or not. The maximum result for a solar direct normal irradiance equal to 700 W/m^2, was achieved by toluene which had an increase of around 4% due to the recuperative cycle. For the optimal cycle, the maximum temperature is 367 ^{o}C (with 65 ^{o}C superheating) in 33.5 bar and the condensing temperature 55 ^{o}C. As for the accomplished efficiency, the thermal cycle reached a 31.5% with a total solar efficiency equal to 23.3%. The distinction between the direct and the indirect system did not affect these values, since for all the working fluids both systems had almost the same efficiency.

Nafey and Sharaf [28] investigated as well a solar driven ORC system aiming at coupling it with a reverse osmosis desalination unit. Their research included the computational optimization of the cycle with three different types of collectors, Flat plate collectors (FPCs), Compound

parabolic concentrators (CPCs) and Parabolic trough collectors (PTCs) and for various working media for a DVG system. However, in the first two cases they provided heat at a low temperature range (lower than 150 ^{o}C). For PTCs, four different fluids, that had the appropriate critical point to perform at the desired temperature range, were evaluated and among them the optimal efficiency was achieved by toluene. Subsequently, the authors further calculated the performance and the exergy efficiency of the cycle in case of a 20 ^{o}C superheating of the vapor. The results showed a cycle's efficiency equal to 26.0% and a corresponding exergy equal to 14.1% for maximum temperature and pressure 320 ^{o}C and 32.78 bar, respectively. These results are slightly higher than the ones yielded in case of saturated vapor. The aforementioned review was extended by the authors [29] in order to examine thermo-economically the desalination system by evaluating three different configurations used to perform the reverse osmosis. Based on the previous research they applied their calculations on a PTC system with DVG in which the working fluid was again toluene. The difference in this study had to do with the maximum developed temperature of the cycle which was slightly higher. For solar radiation equal to 850 W/m^2, as previously, the superheating temperature was 340 ^{o}C for the same evaporating pressure, leading to a much higher thermal efficiency equal to 32.6%.

Casati et al. [30] worked also on an ORC driven by a CSP plant of small to medium capacity, using PTCs. Apart from the thermal study of the plant, the authors mainly focused on the implementation of an innovative system for direct thermal storage, in which the same organic fluid is used as working and storage medium. As for the selected fluid, they chose to investigate the family of siloxanes which are usually used in applications of this temperature range. By performing a preliminary analysis of the thermodynamic cycle, they checked the behavior of the four alternative fluids and concluded that D4 is the most suitable choice. The simulation of the cycle coupled with the TES system was performed for maximum pressure equal to 14.2 bar, whereas the maximum temperature was 312.7 ^{o}C, with the fluid entering the expander in a state of saturated vapor. As for the condensation temperature, it was chosen relatively high at 80 ^{o}C while the direct normal irradiation at 850 W/m^2. The calculated thermal efficiency was 25.1% and by taking into consideration the efficiency of the solar collectors as well the total efficiency was 18.0%.

Kumar and Shukla [31] analyzed a solar ORC system providing results for higher maximum temperature levels of the fluid's vapor. As for the organic fluid, they investigated the behavior of benzene, which performed the cycle of a superheating system, without including the medium's regeneration. The system consists of PTCs, which transfer heat to a receiver used as a reservoir of the intermediate HTF and then to the organic medium which is evaporated and then superheated reaching a maximum temperature equal to 458 ^{o}C at an evaporation pressure of 25.33 bar. The authors examined the variation of the temperature of the fluid entering the expander with varying boiler inlet temperature and concluded that they are almost independent, with a very slight fluctuation of the first for a high range of the latter. Finally, they found that the thermal efficiency of the Rankine cycle can reach values up to 48.8% for the same conditions.

Alvi et al. [32] worked on a thermodynamic model of a solar ORC focusing on the comparison of two thermal storage systems. The first one used water as an HTF and the solar energy was

transferred indirectly to the working fluid, whereas in the second system took place a direct energy transfer using the working fluid as HTF as well, as shown in the figure below. In both cases R245fa was selected as the most appropriate medium for the ORC cycle, which did not include any preheating. The results were extracted in an annual basis, by calculating the produced power and the system's efficiency under different weather conditions. The data showed a great difference between the two configurations with the direct system yielding an efficiency more than three times greater than the corresponding value of the indirect. The overall annually mean system's efficiency (for the direct heat transfer) was approximately 8%, varying from 7.5% during winter up to 8% during summer. For the hottest week of the year and for temperature levels close to 390 ^{o}C, the total solar efficiency reached up to 11.5% for the direct and close to 4.0% for the indirect system.

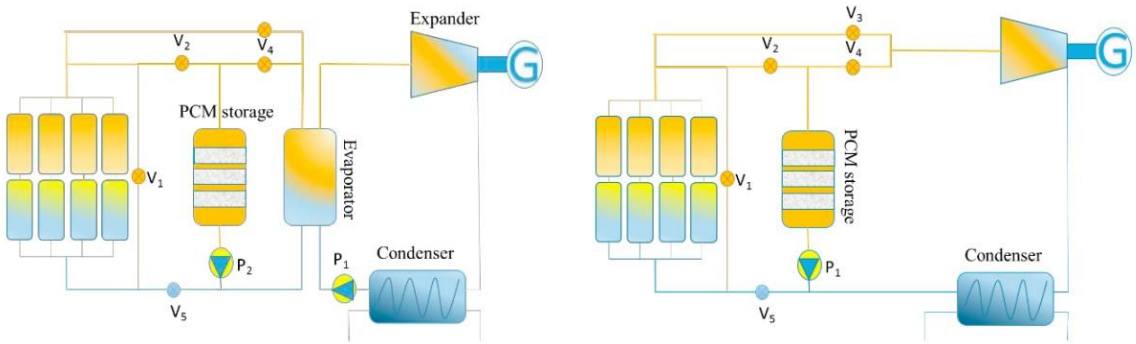

Figure 1.8: Schematic of the systems investigated by Alvi et al.[32]

Another study on a solar driven ORC which received thermal energy with the use of concentrating solar collectors was carried out by Ferrara et al. [33]. They analyzed the thermodynamic behavior of three alternative working fluids, comparing the total solar efficiency of the plant for different configurations of an HTF system aiming at identifying the optimal result. The efficiency was calculated for every fluid in three cases, at first for a conventional ORC ending at a saturated vapor state, subsequently they added a superheating process and finally they inserted a regenerator. The acquired data showed that for every fluid the superheating contributed slightly to the efficiency increase (at a range between 4%-13% of the saturated case), whereas the corresponding increase for the system that included both the superheating and the regenerator was much higher (between 43%-67% of the simple superheated case). Finally, the optimal result was achieved by using acetone as working medium, which for a maximum temperature and pressure equal to 390 ^{o}C and 29.85 bar and for the condensation temperature fixed at 40 ^{o}C yielded a maximum total efficiency of 17.8%. For the case of acetone, they examined further the possibility of implementing a supercritical cycle, by inserting a much higher compression of the fluid and also a reheating process. By iterative calculations they defined the optimal upper pressure at 100 bar and for the same maximum cycle's temperature attained an efficiency of 19.9%.

Apart from the previous study, there are also other cases in which a supercritical cycle of the fluid is implemented. In this context, Xu et al. [34] developed a model for a DVG system, in a regenerative cycle, receiving energy from linear Fresnel reflectors (LFRs) and performing the cycle above the critical pressure of the working fluid. The review focused on evaluating the performance of six potential organic media with critical temperatures between 180 ^{o}C and 350 ^{o}C and pressures in a range between 27 and 42 bar. At first, they examined the change in the efficiency of the ORC and the collectors as the expander inlet temperature is modified and defined the temperature that yields the maximum overall result for each fluid. Subsequently, they calculated the corresponding efficiency for the subcritical cycle as well and compared all the alternative cases in order to identify the optimum working medium. Cyclohexane had the best result both for the thermal and the overall efficiency in the subcritical and the supercritical cycle. For the subcritical, with expander inlet conditions at 281.9 ^{o}C and 40.45 bar the calculated ORC efficiency is 22.8% and the overall one 16.34%, whereas for the supercritical, with 350 ^{o}C and 48.9 bar the respective values were 28.0% and 19.65%. In all the cases the solar irradiance is considered equal to 800 W/m^2.

Bellos and Tzivanidis [35] examined a power production hybrid system which received thermal energy from two energy sources. The studied configuration consists of a recuperative HTF system, in which the heat storage tank, apart from the concentrating solar collectors (PTCs), is coupled with a waste heat recovery system transferring heat to the lower (colder) part of the tank. Hence, the latter contributes only to the preheating of the working fluid, whereas the evaporation takes place due to the heat transferred from the collectors. The study inspects the behavior of four alternative working fluids. For each one of them is defined the appropriate saturation temperature which gives the maximum energy production and hence efficiency of the plant. From the selected media and for solar irradiance equal to 800 W/m^2, toluene appeared to have the most profitable result with a thermal efficiency of 30.6% and a total system's equal to 19.7%, achieved for maximum cycle's temperature of 280 ^{o}C.

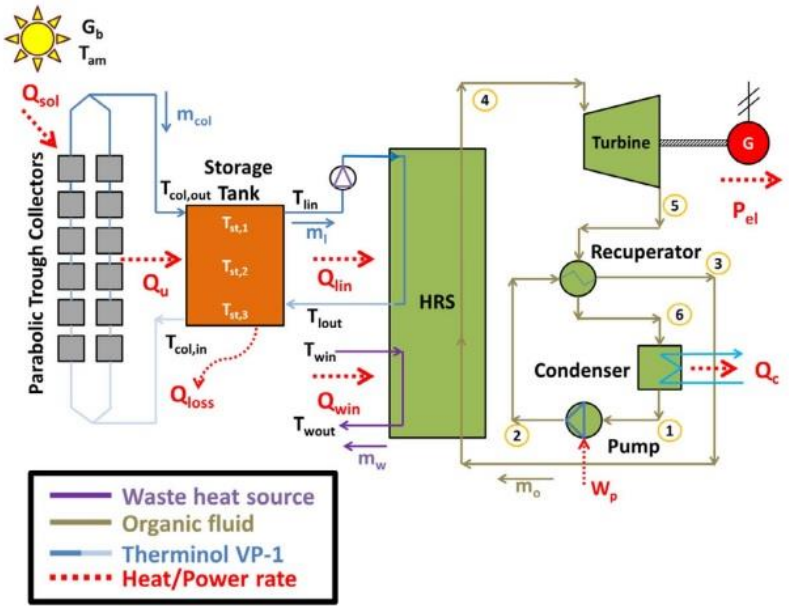

Figure 1.9: Schematic of the system investigated by Bellos et al.[35]

Another review of a solar ORC system coupled with a desalination process was carried out by Sharaf et al. [36]. They focused on comparing the ORC power production technology with a direct exploitation of the thermal energy provided by the collectors in order to perform the water's desalination. As far as the ORC configuration is concerned, they worked on a solar field consisting of PTCs coupled with an HTF system using Therminol-VP1 as heat transfer oil and using a recuperator for the preheating of the organic medium. Concerning the working fluid, they chose toluene as the most appropriate for the selected working temperature range and the maximum expander inlet temperature was fixed at 200 ^{o}C. For these working conditions and for a mean solar radiation equal to 252 W/m^2, the developed model gave a total power production efficiency equal to 16.6%, corresponding to a thermal cycle's efficiency equal to 23.8%.

Following the same logic as in the previous study, they extended the analysis by adjusting the system's characteristics to a higher temperature range [37]. With the same type of collectors, working fluid and intermediate heat transfer system, they increased the vapor's maximum temperature up to 300 ^{o}C. For these conditions the ORC efficiency rose to 30.3%, yielding a total solar efficiency equal to 21.1%, confirming thus the significant improve of the system's response.

Finally, a review of the alternative working fluids used in ORC was done by Maraver et al. [38], focusing on a high temperature cycle without examining exclusively solar energy as heat source. This study examined a poly-generation system including a desalination process and simulated the unit's function for various organic media. At first, they performed a preliminary screening of the available organic fluids presenting their properties (mainly critical point) for around hundred substances (without including any fluid mixtures). Subsequently they excluded those that did not fulfill the necessary environmental restrictions or that were not appropriate for the current application, selecting mainly dry fluids with a critical temperature above 180 ^{o}C, that could respond properly in a high temperature heat source. The remaining 33 fluids that were not discarded were modeled on a saturated cycle in order to calculate their thermal efficiency. From the examined fluids the optimal ORC efficiency was achieved by Dodecamethylcyclohexasiloxane (D6) and was equal to 30.5% with top temperature 368 ^{o} C at a pressure of 9 bar. However, for this fluid (as well as for siloxanes in general) the condensing pressure is low, leading also to low densities and requiring larger components which increases the cost of the plant. Hence, they concluded that techno-economically the most appropriate solutions would be Octamethyltrisiloxane (MDM) with efficiency equal to 22.5% at 289.3 ^{o}C or Fluorobenzene which gives 18.8% at 266.1 ^{o}C and have also acceptable densities.

All the above studies are summarized in the table below, in which the maximum temperature of the cycle, the working fluid and the acquired efficiency of the system are listed.

Table 1.1: Bibliographic review of studies on solar ORC systems

Maximum cycle temperature (°C)	Reference	Working fluid	Thermal efficiency (%)	Total conversion efficiency (%)	Heat source
145	Delgado-Torres and Garcia Rodriguez [9]	Isopentane	16.4	8.51	Solar power (ETC)
169	Quoilin, Orosz et al. [22]	Solkatherm (SES36)	13.1	7.9	Solar power (PTC)
170	Desai et al. [23]	R113	17.68	-	Solar power (LFR)
200	Pikra et al. [24]	R123	10.63	4.67	Solar power (PTC)
200	Sharaf et al. [36]	Toluene	23.8	16.6	Solar power (PTC)
210	Desai et al. [23]	R113	20.07	-	Solar power (PTC)
180-230	Calise et al. [25]	N-pentane	9-10	-	Solar power (ETC)
270	Patil et al. [26]	Isobutane	20.26	-	Solar power (PTC)
280	Bellos and Tzivanidis [35]	Toluene	30.61	19.7	Solar power (PTC)
281.9	Xu et al. [34]	Cyclohexane	22.77	16.34	Solar power (LFR)
289.29	Maraver et al. [38]	MDM	22.49	-	-
300	Sharaf et al. [37]	Toluene	30.29	21.11	Solar power (PTC)
312.7	Casati et al. [30]	D4	25.1	18	Solar power (PTC)
320	Nafey and Sharaf [28]	Toluene	26	-	Solar power (PTC)
340	Nafey et al. [29]	Toluene	32.64	-	Solar power (PTC)
350 (supercritical cycle)	Xu et al. [34]	Cyclohexane	27.95	19.65	Solar power (LFR)
367	Chacartegui et al. [27]	Toluene	31.5	23.3	Solar power (PTC)

367.95	Maraver et al. [38]	D6	30.53	-	-
377.3	Bruno et al. [21]	N-propylbenzene	32.19	21.44	Solar power (PTC)
380	Delgado-Torres and Garcia Rodriguez [18]	Toluene	31.7	22.35	Solar power (PTC)
390	Ferrara et al. [33]	Acetone	-	17.8 (subcritical cycle) 19.9 (supercritical cycle)	Solar power (PTC)
390	Alvi et al. [32]	R245fa	-	11.5	-
458	Kumar and Shukla [31]	Benzene	48.84	-	Solar power (PTC)

1.4. Thesis scope

As already mentioned, the modelling of an ORC system and its coupling with solar collectors is a topic of sufficient interest. However, the competitiveness of this configuration is still vague. The scope of this study is to address the following:

- How can a solar driven ORC system be modelled?
- How is performed the sizing of an ORC system?
- Which are the energetic benefits/drawbacks of the realization of a solar driven ORC?
- Is the solar ORC techno-economically feasible using medium to high grade heat sources?
- Which is the optimal combination of working fluid and type of solar collector?
- How is the economic feasibility of a solar ORC varying in different countries?

Chapter 2. Solar system

2.1. Solar collectors

The solar collectors are the main components of the solar system and constitute the heat source used in this study. A solar collector is in fact a heat exchanger that absorbs the irradiance emitted by the sun and converts it to thermal energy, in case of solar thermal systems, or electric energy in photovoltaic applications [39].

The thermal energy absorbed by the solar collectors is transferred to the working fluid, which depending on the type of the collector and the maximum achieved temperature can be air, water, thermal oil or other organic fluid [40]. The heat carried by the fluid can be exploited for domestic applications (hot water, heating) or in sorption solar cooling systems [41], or can be stored in thermal energy storage tanks for future use [39].

Collectors are mainly divided into two categories based on their absorbing area (Figure 2.1): concentrating and non-concentrating. In non-concentrating collectors the whole intercepting area is used as absorber (concentration ratio equal to 1), engaging both the direct and the indirect solar irradiance. In most cases they remain stationary, without altering their slope based on the sun's position and are mostly used in low temperature applications (roughly up to 150 ^{o}C) [40]. The most common types of non-concentrating collectors are Flat plate collectors (FPCs), used also in case of hybrid PVT systems, and Evacuated tube collectors (ETCs).

On the contrary, in concentrating collectors only the sun's direct radiation is utilized. Mirrors of large aperture area focus and reflect the sunlight onto a receiver with a much smaller area, in which the absorption takes place (concentration ratio higher than 1), resulting in a higher heat flux and leading to much higher working temperatures [40, 42]. Furthermore, in most cases they include a sun-tracking system, which rotates the collecting area properly, by changing its tilt angle according to the sun's position, aiming at a perpendicular incidence of the solar beams to the collector and maximizing the absorbed solar irradiance [43]. In this category belong the Compound parabolic collectors (CPCs), trough collectors (parabolic, cylindrical), Fresnel reflectors (linear, circular), Parabolic dish collectors (PDCs) as well as solar towers.

In this study the operation of an ORC system in a medium to high working temperature range is studied, hence only concentrating collectors will be examined. From the available concentrating collectors, Parabolic trough collectors (PTC) and Parabolic dish collectors (PDC) are selected and modeled, since they are the two most common alternatives that respond effectively in the examined temperature interval (between 150-250 ^{o}C).

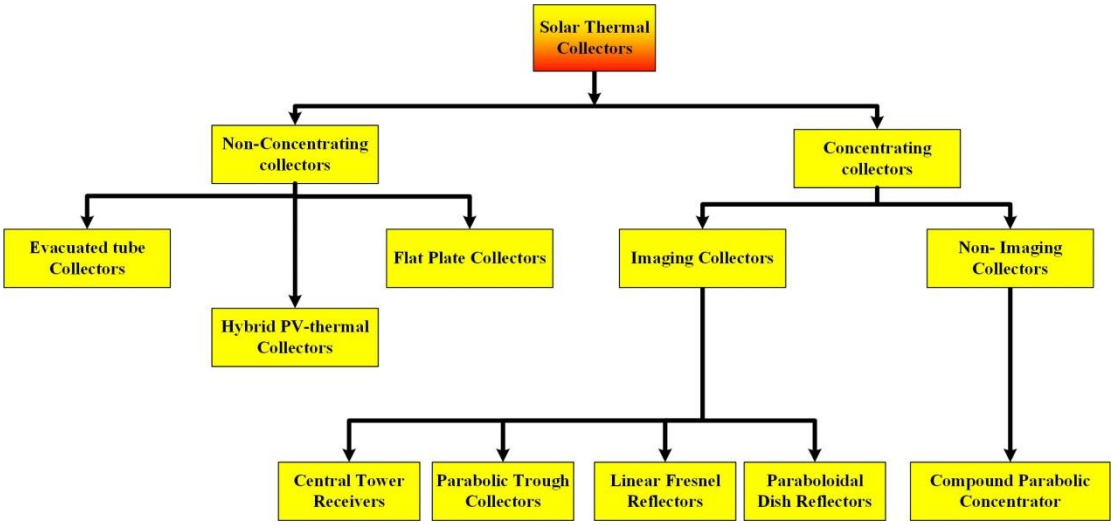

Figure 2.1: Classification of solar collectors

The studied and modeled heat source system that feeds the ORC circuit consists of two main subsystems, the solar collectors and the heat transfer circuit, which are connected by the heat storage tank as it is shown below in the figure.

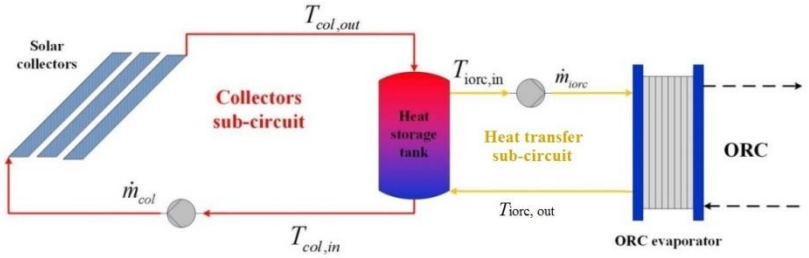

Figure 2.2: Representation of the heat source solar system

For both solar sub-circuits the selected heat transfer fluid (HTF) is the same and is chosen based on the maximum working temperatures. Hence the utilization of a thermal oil is necessary. The two most common alternatives for the intermediate heating system are Therminol D-12 and Therminol VP-1 and the working temperature range for both of them is presented in the figure below. Since the reached temperature may exceed 250 ^{o}C, the selected fluid is Therminol VP-1, which will be used in every case in the rest of the study.

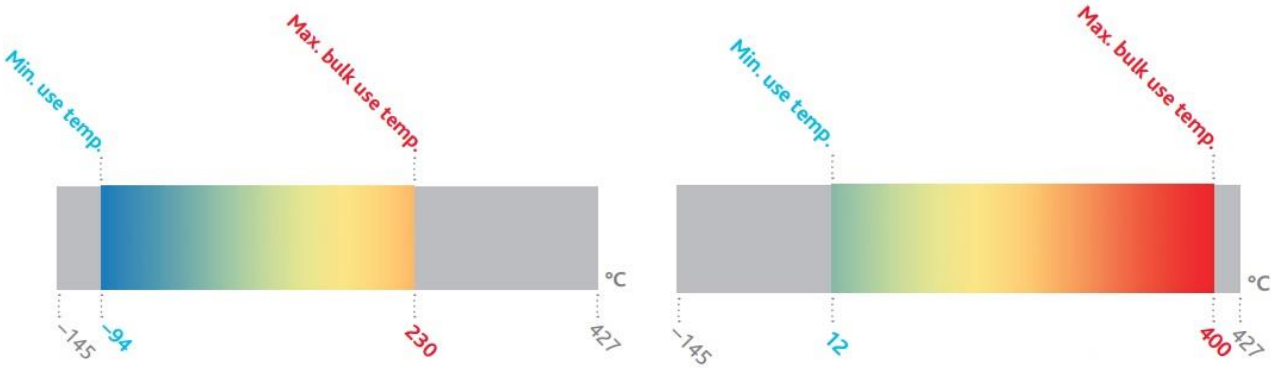

(a) (b)

Figure 2.3: Working temperature range for heat transfer fluids (a) Therminol D-12 [44] and (b) Therminol VP-1 [45]

2.2. Solar collectors modelling

2.2.1 Calculation of the collectors' tilt angle

As it was mentioned before, in this study only Parabolic trough (PTC) and Parabolic dish collectors (PDC) will be studied. Both these types are concentrating collectors and therefore in most cases they are not stationary, but supported with a sun tracking system in order to maximize the accumulated solar energy.

PTCs have the shape of a parabola in two dimensions and extend to a straight line in the third one. They are mostly coupled with one-axis tracking system, in which they are fixed with respect to the north-south axis and rotating around an axis with the direction of east-west. The beams are reflected from the aperture area of the collector to the focal line of the parabola where they are absorbed by a cylindrical receiver, which is placed in a straight line aligned on the east-west direction as well. PDCs have the shape of a full parabola in three dimensions and therefore the solar irradiance is focused on the focal point of the parabola where the absorber is placed. Consequently, their tracking mechanism is designed providing motion in both axes, achieving in that way an incidence angle perpendicular to the collector's surface.

Although the two-axes mechanism is more effective in terms of irradiance absorption, its design, manufacture and installation is much more complicated compared to the single axis system causing a disproportional increase in the unit's cost [46]. Hence, it was decided to implement a one axis tracking system in both of the examined cases of solar collectors.

Since the system contains concentrating collectors, the collectors' tilt angle needs to maximize the direct irradiance received by the tilted surface. Direct irradiance (I_b) is the part of the solar radiation that reaches the earth's surface directly from the sun without undergoing any kind of scattering or dispersion in the atmosphere. The direct irradiance received by a horizontal surface is indicated as I_b; for a surface that is perpendicular to the solar beam the direct

irradiance is indicated as I_{bn} and in case of any other tilted surface as I_{bT}. The direct irradiance of a tilted surface derives from the equation below.

$$I_{bT} = I_{bn} \cos\theta \quad (2.1)$$

with θ to be the incidence angle of the direct irradiance at the surface.

As described previously, I_{bT} should be maximized. For I_{bn}, the data are provided by the energy simulation program EnergyPlus [47], which has database with the annual climatological conditions for various cities. Along with I_{bn} the database contains values of the ambient temperature (T_{amb}), throughout a year, that will be used later for the calculation of the collectors' efficiency. It was decided to study the function of the system in five European cities: Athens, Madrid, Rome, Brussels and Berlin, located in various latitudes across Europe, in order to examine the unit's performance in regions with different geographic and climatic conditions.

Using the analysis from Antonopoulos [39], is calculated in Matlab the appropriate angle β that yields the maximum absorbed direct irradiance on annual basis using an hourly step.

For applying the series of equations, it is necessary to define some geographical data for the selected cities that are going to be examined. These are the location's latitude (ϕ), the longitude (L_{loc}) and the longitude of the standard time meridian (L_{st}) and are presented below in Table 2.1 for Athens, Madrid, Rome, Brussels and Berlin.

Table 2.1: Geographical data of the selected cities

	Athens	**Madrid**	**Rome**	**Brussels**	**Berlin**
Latitude (ϕ) (deg)	37.9	40.45	41.8	50.9	52.47
Longitude (L_{loc}) (deg)	23.73	-3.55	12.23	4.53	13.4
Longitude of standard meridian (L_{st})(deg)	30	15	15	15	15

The tilt angle β was bounded between -80° and 80°, leaving a 10° margin from the total vertical position of the collector. This constraint is set due to the collectors' geometry, preventing the contact of its surface with the ground which may cause damage to the system. The results for each city are presented in the Figure 2.4 below.

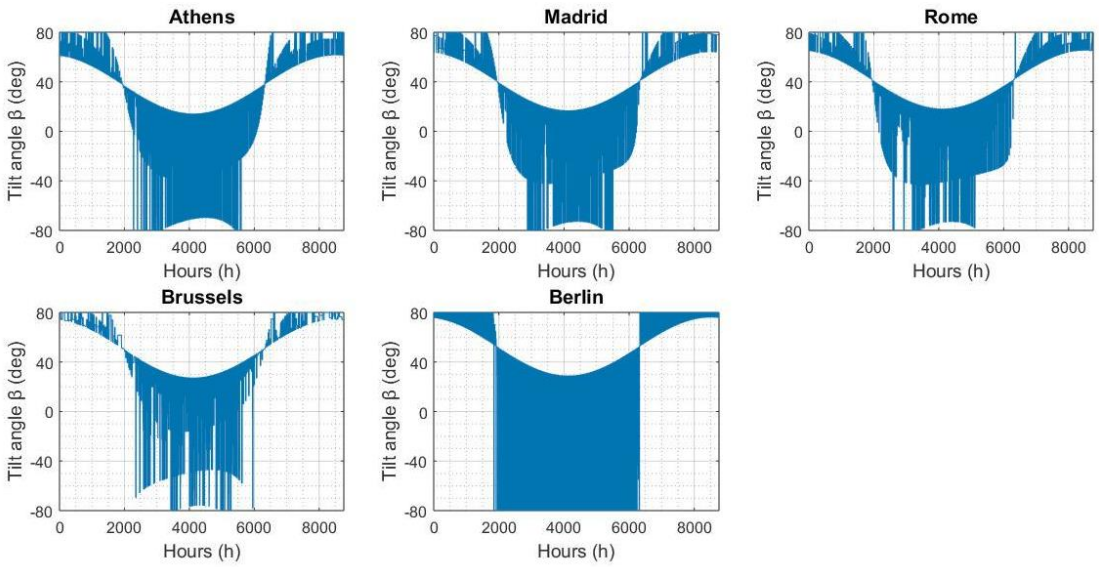

Figure 2.4: Optimal tilt angle of a one axis mechanism, for every hour of the year of each city

As illustrated in the diagrams, the optimal angle varies keenly based on the period of the year due to alteration of the sun's path in the sky. During the summer months, the sun is following a path from north-east to north-west, sliding at a greater height in the sky and resulting in negative and low positive values of the optimal angle β. On the contrary, during winter this movement starts from south-east and ends in south-west following a lower height in the horizon leading to high positive values of β.

Based on the calculated β and the data for I_{bn} acquired from EnergyPlus, the values of I_{bT} for every hour of the year are calculated and demonstrated in Figure 2.5.

The above described optimization process was repeated in order to find the optimal tilt angle of a stationary collector that maximizes the total annual accumulated direct irradiance. In that case is not needed the value of β that gives the optimum at each hour of the year, but the angle that remains constant and provides the maximum sum of I_{bT} in an annual basis.

The results are presented in the table below.

Table 2.2: Optimal tilt angle that maximizes I_{bT} for stationary collectors in each city

	Athens	**Madrid**	**Rome**	**Brussels**	**Berlin**
Optimal tilt angle (β opt) (deg)	29.25	33.25	34.35	40.59	39.05

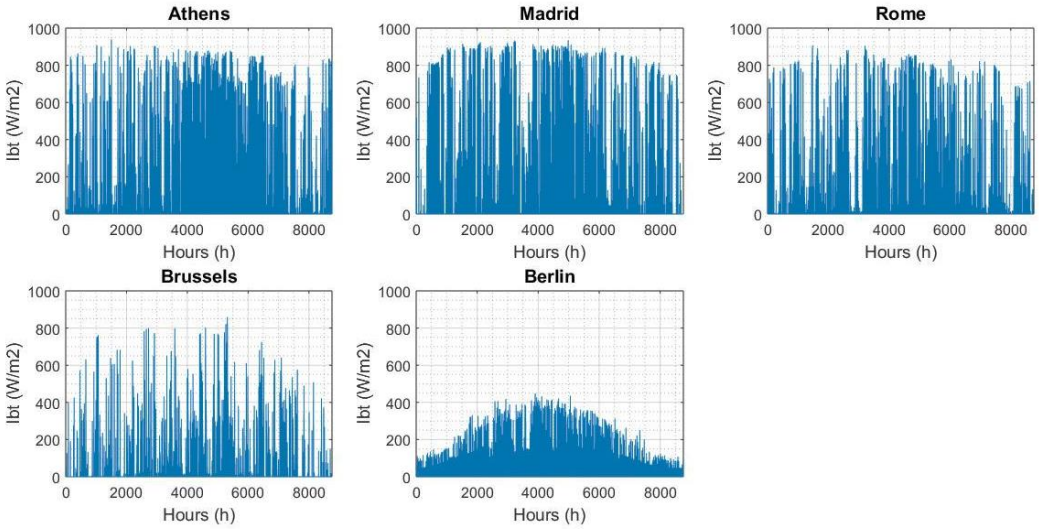

Figure 2.5: Maximum direct irradiance of a tilted surface, with one axis tracking system, for every hour of the year of each city

Comparing the results of the total annual received direct irradiance in case of an optimized stationary collector and a collector with a one axis tracking system, there is an increase of around 7.5% for the studied cities.

This additional amount of the received irradiance justifies the implementation of a simple one axis tracking system that does not affect drastically the complexity of the system and thus without causing a severe increase in its cost.

2.2.2 Specification of the collectors' thermal efficiency

The calculations up to this point defined the direct irradiance incident to the collector's surface. However, the collector absorbs only a portion of I_{bT} and turns it into thermal energy that is further transferred to the ORC system. In order to compute the exploitable thermal energy, the collector's thermal efficiency should be estimated.

The solar collectors' efficiency can be modelled using empirical polynomial expressions that correlate the change in the efficiency with the solar irradiance and the temperature difference between the fluid in the collectors' circuit and the ambient temperature.

The most commonly used equation is of first degree concerning the temperature difference as shown below in equation (2.2):

$$\eta_{col} = c_0 - c_1 \frac{T_{col} - T_{amb}}{I_b} = c_0 - c_1 \frac{\Delta T}{I_b} \qquad (2.2)$$

With

T_{col} being the average temperature of the fluid circulating in the collectors' system,

T_{amb} the ambient temperature provided by the database as already mentioned,

$I_b = I_{bT}$ the already computed received direct solar irradiance (it is used for concentrating solar collectors which are examined in our case, whereas for static non-concentrating collectors the total irradiance is used instead)2,

c_0, c_1 are constants that are defined numerically or experimentally depending on the examined collector.

In order to estimate these parameters, the results of various studies are taken into consideration.

Parabolic trough collectors (PTCs):

There are several studies that focused on extracting linear equations in the form of equation (2.2), whose results are presented below in the table.

Table 2.3: Constants for the efficiency of PTCs

c_0	c_1 ($\frac{W}{m^2K}$)	Reference	c_0	c_1 ($\frac{W}{m^2K}$)	Reference
0,76	0,22	Ferreira et al. [48]	0.658	0.683	Coccia et al. [49]
0,700664	0,8659	Sotte [50]	0,5214	0,1006	Yilmaz et al. [51]
0,69	0,39	Arasu et al. [52]	0,5608	2,468	Venegas-Reyes et al. [53]
0,673	0,2243	Kasaeian et al. [54]	0,5586	2,227	Jaramillo et al. [55]
0,66	0,233	Murphy et al. [56]	0,5523	2,0099	Brooks et al. [57]
0,65	0,382	Hurtado et al. [58]	0,543	0,189	Hau et al. [59]
0,642	0,441	Kalogirou et al. [60]	0,5381	0,201	Brooks et al. [57]
0,638	0,387	Kalogirou [61]	0,523	0,383	Subramani et al. [62]
0,6224	2,368	Jaramillo et al. [63]			

Furthermore, there are also, in the bibliography, equations of second degree considering the aforementioned temperature difference.

Cabrera et al. [64] use the following equation that gives the collectors' efficiency

$$\eta_{col} = 0.68 - 0.4\frac{T_{col}-T_{amb}}{I_b} - 0.0015\frac{(T_{col}-T_{amb})^2}{I_b} = 0.68 - 0.4\frac{\Delta T}{I_b} - 0.0015\frac{\Delta T^2}{I_b}$$ [65]

Whereas Zadeh et al. [66] present and apply the equation given by Dudley et al. [67]

$$\eta_{col} = 0.733 - 0.00007276(T_{col} - T_{amb}) + 0.0496\frac{T_{col}-T_{amb}}{I_b} - 0.000691\frac{(T_{col}-T_{amb})^2}{I_b}$$

$$\eta_{col} = 0.733 - 0.00007276(\Delta T) + 0.0496\frac{\Delta T}{I_b} - 0.000691\frac{(\Delta T)^2}{I_b}$$

All the above models are shown below in the figures, in which is presented the change in the efficiency as the temperature difference varies, assuming that the direct irradiance has a fixed value equal to 800 W/m^2.

Based on the aforementioned equations, two separate groups of lines are distinguished. The first one that is shown in more detail in the Figure 2.6 below, consists of graphs that have a high slope, yielding relatively low efficiencies for high temperature differences. These graphs correspond to models developed for specific experimental setups in a narrow temperature range and therefore cannot be applied reliably in this study.

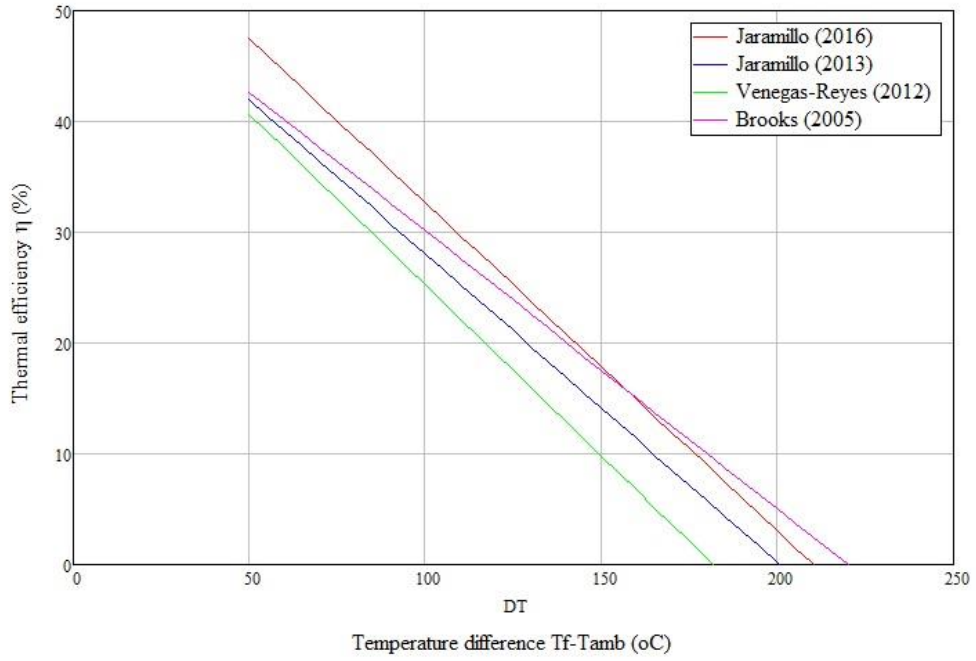

Figure 2.6: Thermal efficiency of PTCs

From the curves, shown in Figure 2.7 Dudley's equation was extracted from an experimental study for Sandia National Laboratory and has been confirmed and used extensively as a reference by various researchers, such as Forristall (2003) [68], Hachicha et al. (2013) [69], Moloodpoor et al. (2019) [70]. However, this model is valid in cases that the solar irradiance is relatively high (values tested in this model vary around 800-1000 W/m^2) and the results produced in lower ranges give rather high thermal efficiencies.

Hence, since this study examines the overall annual behavior of the collectors and thus the solar irradiance varies vastly, finally is selected the equation produced by Kasaeian et al. [54] equation (2.3), which is close to Dudley's for direct irradiance equal to 800 W/m^2, but also in accordance with the rest of the developed models.

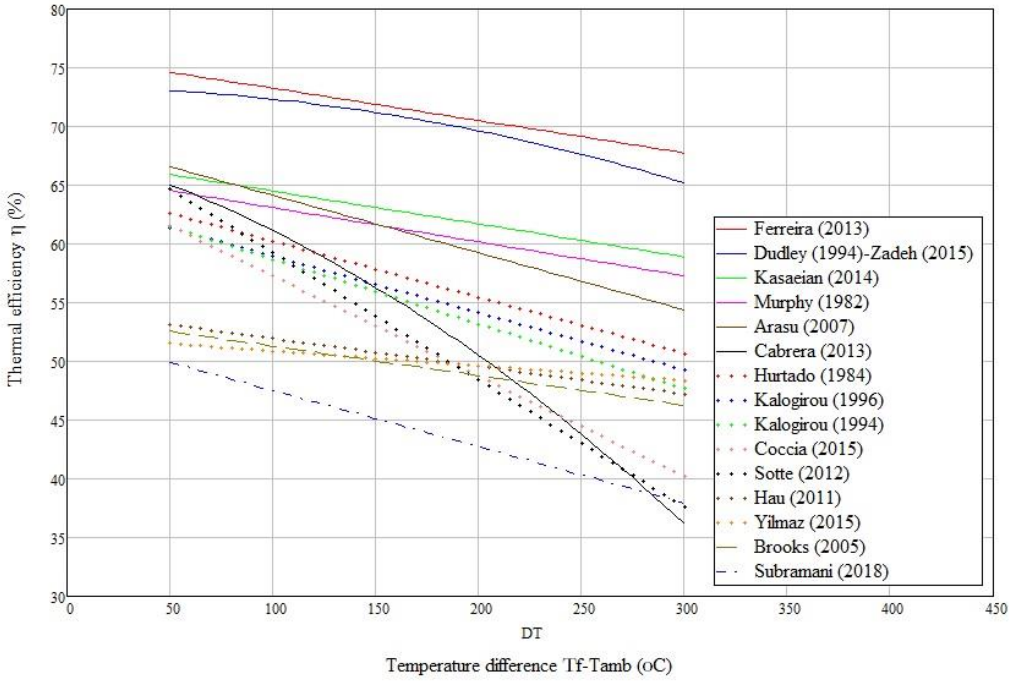

Figure 2.7: Thermal efficiency of PTCs

$$\eta_{col.PTC} = 0.673 - 0.2243 \frac{T_{col} - T_{amb}}{I_b} \quad (2.3)$$

Parabolic disc collectors (PDCs):

Concerning the parabolic dish concentrators, there have been less studies (mainly experimental) investigating the variation of the thermal efficiency with respect to the aforementioned temperature difference. Wu et al. [71], as well as Moradi et al. [72] developed and validated models that calculate the collectors' thermal efficiency from the collectors' temperature, which are shown below in Figure 2.8. However, the produced temperature difference in these cases reaches really high levels, which are not applied in cases of ORC systems and could be coupled probably with the conventional water Rankine cycle.

Similar to parabolic troughs, there are some linear equations in the form of equation (2.2) as shown in the table.

Table 2.4: Constants for the efficiency of PDCs

c_0	c_1 (W/m^2K)	Reference
0.82	0.22	Ferreira et al. [48]
0.7053	1.2503	Loni et al. [73]
0.653	2.1264	Loni et al. [73]

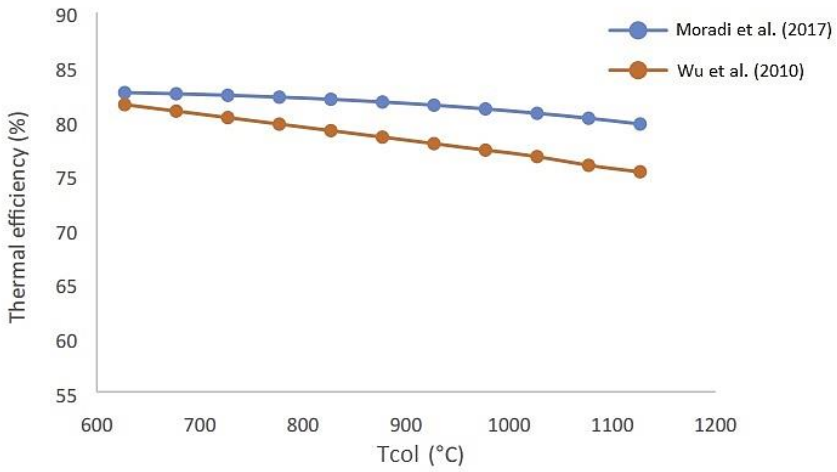

Figure 2.8: Thermal efficiency of PDCs

Furthermore, Bianchini et al. [74] concluded that a polynomial expression as described below could be applied in a parabolic dish system and Stefanovic et al. [75] developed a numerical model describing the collectors' efficiency.

$$\eta = 0{,}456 - 0{,}8\frac{DT}{I_b} - \frac{0.014DT^2}{I_b}$$

These models are presented below in Figure 2.9. From these alternative curves Loni's first curve is chosen (equation 2.4), since it is the only one validated both experimentally and numerically and also gives results close to the rest of the available diagrams.

$$\eta_{col.PDC} = 0.7053 - 1.2503\frac{T_{col} - T_{amb}}{I_b} \qquad (2.4)$$

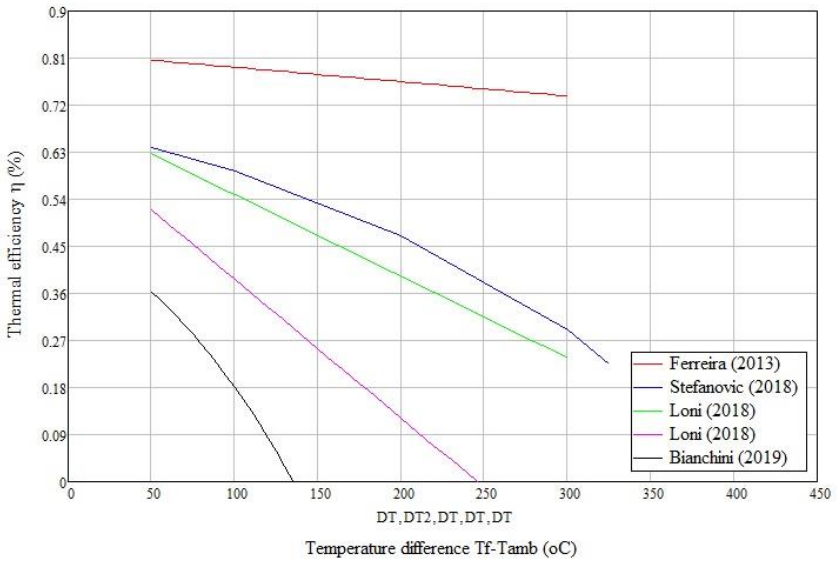

Figure 2.9: Thermal efficiency of PDCs

2.3. Heat storage tank

The fluctuations and the unpredictability of the received solar energy, as well as the mismatch between the availability of the thermal energy and the consumption needs, require a system in order to stabilize the operation of the ORC system. Because of that, the incorporation of a heat storage tank into the system becomes necessary.

The storage period depends on the tank's dimensions, the heat capacity of the storage fluid, as well as the tank's insulation and the ambient temperature. Additionally, a heat storage unit offers a more stable function of the evaporator, since it introduces thermal inertia between the solar and the ORC circuit and absorbs the energy spikes in case of non-regular climate conditions [41].

The developed model for the thermal energy storage (TES) system is based on the assumption of the thermal stratification of the tank [76]. The tank is considered to be separated into horizontal zones inside each of which the storage fluid has a uniform temperature. Every zone inside the cylindrical vessel has the same height and thus containing the same volume of fluid. Between the zones heat and mass transfer phenomena take place which contribute to its final temperature stratification, leading to higher temperatures at the top of the tank (first zone) which gradually decrease and reach their minimum value at the bottom (last zone).

Assuming that the tank consists of n zones, as shown below in Figure 2.10, for each zone the mass and energy balance equations are satisfied [77].

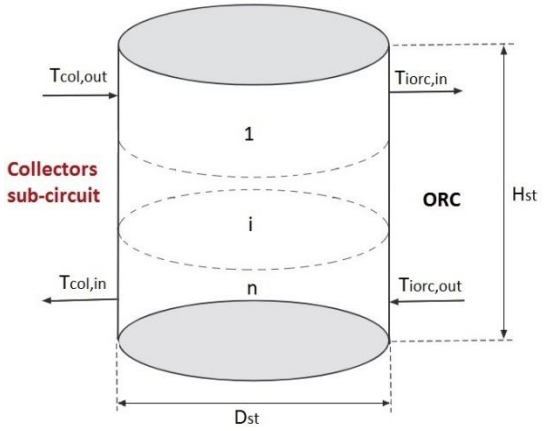

Figure 2.10: Representation of the heat storage tank

Mass balance:

Due to the equal volume of each zone and supposing that the density is constant in the whole tank (negligible density difference between the zones), does not give any significant result.

$$\frac{dm}{dt} = \dot{m}_{in} - \dot{m}_{out} = 0 \quad (2.5)$$

Energy balance:

$$\frac{dQ}{dt} = Q_{in} - Q_{out} - Q_{loss} \quad (2.6)$$

For totally n temperature zones at time t, the energy balance equations are:

- For the first zone, $j = 1$:

$$\frac{M_{st}}{n} C_p \frac{\left(T_{st}(t,1) - T_{st}(t-1,1)\right)}{\Delta t} = \dot{m}_{col} C_{p,colout}\left[T_{col,out} - T_{st}(t,1)\right] +$$

$$+\dot{m}_{iorc} C_{p,iorcout}\left[T_{st}(t,2) - T_{st}(t,1)\right] - U_l A_{st}(1) \cdot \left[T_{st}(t,1) - T_{amb}\right] \quad (2.7)$$

- For the intermediate zones, $j = (2, \dots, n-1)$:

$$\frac{M_{st}}{n} C_p \frac{\left(T_{st}(t,j) - T_{st}(t-1,j)\right)}{\Delta t} = \dot{m}_{col} C_{p,colout}\left[T_{st}(t,j-1) - T_{st}(t,j)\right] +$$

$$+\dot{m}_{iorc} C_{p,iorcout}\left[T_{st}(t,j+1) - T_{st}(t,j)\right] - U_l A_{st}(j) \cdot \left[T_{st}(t,j) - T_{amb}\right] \quad (2.8)$$

- For the last zone, $j = n$:

$$\frac{M_{st}}{n} C_p \frac{\left(T_{st}(t,n) - T_{st}(t-1,n)\right)}{\Delta t} = \dot{m}_{col} C_{p,colout}\left[T_{st}(t,n-1) - T_{st}(t,n)\right] +$$

$$+\dot{m}_{iorc} C_{p,iorcout}\left[T_{iorc,out} - T_{st}(t,n)\right] - U_l A_{st}(n) \cdot \left[T_{st}(t,n) - T_{amb}\right] \quad (2.9)$$

In the above equations:

M_{st} is the total mass of the TES system and is equal to $M_{st} = \rho V_{st}$, with V_{st} being the total volume of the tank,

$T_{st}(t,j)$ is the temperature of the j zone at time t,

Δt is the examined time interval,

$\dot{m}_{col}$, $\dot{m}_{iorc}$ being the mass flow rate of the collectors' sub-circuit and the intermediate heat transfer sub-circuit respectively,

$T_{col,out}$ is the temperature of the fluid exiting the collectors,

$T_{iorc,out}$ is the returning temperature of the heat transfer circuit which is the hot stream of the ORC evaporator, as shown in Figure 2.2,

U_l is the heat loss coefficient for the storage tank and

C_p is the specific heat of the fluid.

Concerning the calculation of the tank's zones' surface the following equations are applied:

- For the first and last zone $j = 1$ and $j = n$:

$$A_{st}(1) = A_{st}(n) = \pi \frac{D_{st}^2}{4} + \pi D_{st} \frac{H_{st}}{n} \quad (2.10)$$

- For the intermediate zones, $j = (2, \dots, n-1)$:
  $A_{st}(j) = A_{st}(n) = \pi D_{st} \frac{H_{st}}{n}$ (2.11)

With D_{st} and H_{st} being the tank's diameter and height, respectively.

By defining the parameters in the above equations (2.7-2.9) for each temperature zone, a $n \times n$ tridiagonal system of equations is formed which is solved in Matlab and defines the values of each zone's temperature. The temperature of the first zone (top of the tank) is assumed to be equal to the temperature of the stream that returns to the intermediate ORC circuit ($T_{iorc,in}$), whereas the temperature of the last zone (bottom of the tank) is equal to the temperature of the stream that returns to the collectors ($T_{col,in}$).

The above described model calculates the temperature for n zones of the stratified storage tank. However, the temperature of the streams entering the tank ($T_{col,out}$ and $T_{iorc,out}$) are imposed externally as inputs by the solar and the ORC system, respectively. Due to that, in case $T_{iorc,out}$ has a high value, the temperature inside the tank does not decrease gradually, but there are some layers in its bottom with higher temperature values compared to their upper layers. In order to deal with this issue, it was assumed that when this happens the warmer fluid rises upwards and the colder one slides downwards, ending in a completely mixed zone with uniform temperature, equal to the mean temperature of the two initial zones, estimation does not affect severely the accuracy of the model [78].

In order to determine the appropriate number of distinct thermal zones the produced result has to be checked for various number of layers, in order to define the minimum value that does not disturb its precision. For the examined case the temperatures entering the tank are set equal to $T_{col,out} = 200\,^{o}C$ and $T_{iorc,out} = 150\,^{o}C$ and the ambient temperature $T_{amb} = 25^{o}C$. In the Figure 2.11a below is shown the variation of the temperatures exiting the tank for several number of zones. Moreover, using as reference the results produced for 50 layers, it is calculated and presented in Figure 2.11b the relative error induced for each number of zones.

By considering the maximum acceptable relative error equal to 0.2%, the final number of zones is selected to be equal to 25, which will be used in all cases for the rest of this study.

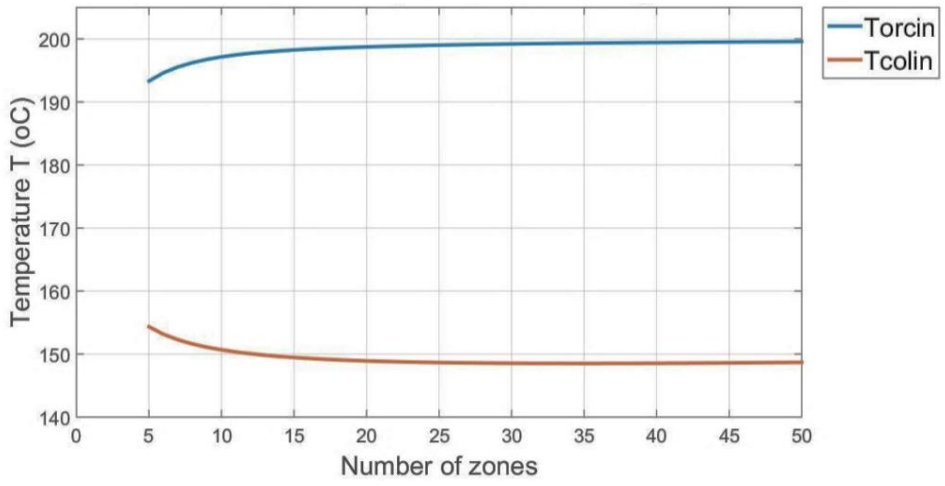

(a)

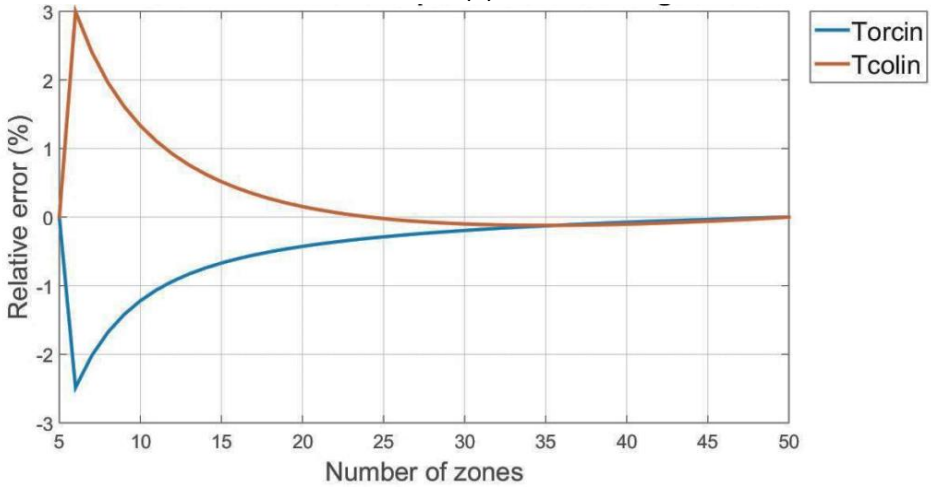

(b)

Figure 2.11: (a) Variation of exit temperature and (b) induced relative error for various number of temperature zones in the storage tank

As explained in Paragraph 2.1, for both of the sub-circuits belonging to the solar loop, shown in Figure 2.2, the selected heat transfer fluid is the same and is chosen to be Therminol VP-1. Consequently, the fluid filling the storage tank and used in the aforementioned calculations is also Therminol VP-1, whose properties depend on its temperature and derive from the technical datasheet [45].

2.4. Operation of solar system

In order to simplify the model of the total solar ORC system and evaluate the response of each sub-system independently, is examined the operation of the collectors' loop, including the intermediate heat transfer system, in an annual base for each of the selected cities and for both types of collectors. At this stage, without using the developed model for the ORC system which will be described in the next chapter, and by assuming some values for the collectors, such as their total surface, the dimensions of the storage tank and the mass flow rate of the heat transfer fluid in the two sub-circuits, the fluid's temperature in each point of the system was defined as well as the panels' efficiency and the power that they produce.

Concerning the collectors:

- The total surface of the solar collectors was chosen to be $A_{col} = 50\ m^2$, for both PTCs and PDCs,
- As for the nominal mass flow rate of the collectors' circuit, it was calculated based on the above total surface and using the equation (2.12) [79]:
  $\dot{m}_{col} = 0.02\ \cdot A_{col} = 1\ kg/s$ (2.12)

Concerning the intermediate heat transfer circuit:

- The mass flow rate at the intermediate system that leaves the storage tank and feeds the ORC's evaporator was chosen to be slightly lower than $\dot{m}_{col}$ in order to achieve a higher temperature difference at the two ends of the stream allowing a more effective stratification in the storage tank. Thus, $\dot{m}_{iorc} = 0.8\ kg/s$.

Concerning the storage tank:

- The total volume of the tank was estimated by using common formulas as shown in equation (2.13) [79]:
  $V_{st} = \frac{A_{col}}{30} = 1.67\ m^3$ (2.13)
- For the dimensions of the cylindrical tank that are used to compute the surface of every of the distinguished temperature zones, as described by the equations (2.10-2.11) the diameter of the vessel is chosen to be $D_{st} = 0.8\ m$. The corresponding height derives from the equation (2.20) since the other values are already known:
  $H_{st} = \frac{V_{st}}{\pi \cdot \frac{D_{st}^2}{4}} = 3.32\ m$ (2.14)
- The heat loss coefficient from the tank to the environment is selected to be equal to $U_l = 0.5 \frac{W}{m^2 K}$, which is a typical value for an insulated tank [80].

The implementation of the model is based on the independent operation of the collectors' loop and the intermediate heat transfer loop, both of which are coupled or decoupled from the total system depending on the prevailing conditions.

In order to describe this calculation process, i refers to a random time of the year.

Operation of the collector loop: Depending on the value of I_{bT}.

In case $I_{bT} = 0$:

There is no energy supply from the sun and thus there is no heat transferred to the storage tank. The collectors' loop is disengaged and the corresponding mass flow rate equal to 0, $\dot{m}_{col,i} = 0$. Accordingly, zero values are assigned for the thermal efficiency and the produced power, $\eta_{col,i} = 0$, $Q_{col,i} = 0$.

At this case the temperature of the fluid exiting the collectors is equal to the temperature of the entering stream, therefore

$T_{col,out,i} = T_{col,in,i}$ (2.15)

In case $I_{bT} > 0$:

The collector absorbs the received energy and heats up the fluid that ends up at the top of the storage tank. The mass flow rate at the first circuit has its nominal value, $\dot{m}_{col,i} = 1\ kg/s$.

The calculation of the collectors' thermal efficiency derives from equation (2.2), with constants that are specified for each type of collector equations (2.3-2.4), as it was described in the previous paragraphs. This calculation requires the value of $T_{col,i}$, which is the average temperature of the inlet and outlet stream equation (2.16).

$$T_{col,i} = \frac{T_{col,in,i} + T_{col,out,i}}{2} \quad (2.16)$$

However, the outlet temperature is the parameter that needs to be defined and thus at this point is not known and therefore, a loop should be initiated in order to estimate it.

At first, is supposed that the outlet temperature is equal to the inlet one, $T_{col,out,i} = T_{col,in,i}$. By using the equation (2.2) is computed the thermal efficiency $\eta_{col,i}$ and by applying the definition of the collectors' efficiency, it can be determined the absorbed power, as shown by the equation (2.17) below:

$$\eta_{col,i} = \frac{Q_{col,i}}{A_{col} \cdot I_{bT,i}} \Rightarrow Q_{col,i} = \eta_{col,i} \cdot A_{col} \cdot I_{bT,i} \quad (2.17)$$

This power is transferred to the fluid in order to heat it up, producing the temperature raise that needs to be calculated. Hence, by applying the following equation (2.18):

$$Q_{col,i} = \dot{m}_{col} \cdot C_{p,col} \cdot \left(T_{col,out,i} - T_{col,in,i}\right) \Rightarrow T_{col,out,i} = T_{col,in,i} + \frac{Q_{col,i}}{\dot{m}_{col} \cdot C_{p,col}} \quad (2.18)$$

in which $\dot{m}_{col}$ is already known and for the heat capacity is considered to be constant and equal to the one corresponding to the already known $T_{col,in,i}$, since the difference in its value along the fluid's circuit is negligible for the resulting temperature shift.

In that way, from equation (2.18) derives a new value for $T^{new}_{col,out,i}$, different from the initial guess. Using this last value and applying again the equations (2.16), (2.2), (2.17), (2.18) the thermal efficiency is recalculated, the absorbed power and the outlet temperature respectively. This iterative procedure continues and these parameters are renewed until $T_{col,out,i}$ converges with an acceptable relative error, which was set to be 0.01%.

$$\left|\frac{T^{new}_{col,out,i} - T_{col,out,i}}{T_{col,out,i}}\right| < 0.01\% \quad (2.19)$$

Furthermore, in some cases, although the solar irradiance may be positive, when applying equation (2.2) for the computation of the collectors' efficiency, the latter may take negative values. That happens when the direct solar radiation (I_{bT}) has a rather small value which makes the second term of the equation relatively high, resulting in a negative sign of the efficiency. Under these circumstances, it was supposed that the collectors are unable to receive any heat from the sun, thus they are decoupled from the system. The mass flow rate,

their efficiency and the power take zero values, $\dot{m}_{col,i} = 0$, $\eta_{col,i} = 0$, $Q_{col,i} = 0$ and the outlet temperature is equal to the inlet one:

In a similar way to the collectors, of the operation of the intermediate circuit that transfers the heat to the ORC was modeled. It was considered that this system operates and fluid circulates towards the evaporator, in cases its maximum temperature is higher than a temperature limit ($T_{threshold}$). This maximum temperature ($T_{iorc,in}$) is equal to the stream exiting from the storage tank and entering the circuit and as it has already been mentioned is equivalent to the temperature of its first zone (T_{stor}^{1}).

Since the ORC system has not yet been modeled, it is assumed that when the circuit is open, the evaporator absorbs a constant amount of energy (Q_{iorc}), which is imposed externally and represents the load of the ORC.

Regarding the specification of the threshold temperature ($T_{threshold}$) and the absorbed heat (Q_{iorc}), it was decided to preserve them constant for all the examined cities, in order to perform a similar analysis allowing the comparison of the system in different locations. At a first approach and since is investigated the performance of the system in a medium to high temperature range, is selected $T_{threshold} = 180^{o}C$ and $Q_{iorc} = 40\ kW$.

Operation of the intermediate heat transfer loop: Depending on the value of $T_{threshold}$.

In case $T_{stor}^{1} < T_{threshold}$:

There is not adequate amount of thermal energy in order to drive the ORC and therefore the heat transfer loop remains closed and its mass flow rate is equal to 0, $\dot{m}_{iorc,i} = 0$. The power absorbed in this case is obviously 0 as well, whereas the outlet temperature of this sub-circuit is equal to the inlet one.

With the outlet temperatures of both the collectors and the intermediate circuits already defined, the function of the storage tank can be solved as described in the previous paragraph and returns the temperature at all its layers. From the top and the bottom layer derive the temperature that enters the collectors ($T_{col,in,i+1}$) and the heat transfer circuit ($T_{iorc,in,i+1}$) the next moment of the calculation, which are used as an input for the calculations of the following hour.

In case $T_{stor}^{1} \geq T_{threshold}$:

The thermal oil circulates transferring heat from the storage tank to the evaporator with a mass flow rate equal to its nominal value, $\dot{m}_{iorc,i} = 0.8\ kg/s$. As it is already mentioned the absorbed heat ($Q_{iorc,i}$) is already known and has a constant value depending on the examined city.

Based on this parameter and by applying a simple energy balance is defined also the temperature of the stream exiting the circuit:

$$Q_{iorc,i} = \dot{m}_{iorc} \cdot C_{p,iorc} \cdot \left(T_{iorc,in,i} - T_{iorc,out,i}\right) \Rightarrow T_{iorc,out,i} = T_{iorc,in,i} - \frac{Q_{iorc,i}}{\dot{m}_{iorc} \cdot C_{p,iorc}} \quad (2.20)$$

in which the heat capacity ($C_{p,iorc}$) is considered to be constant and equal to the one corresponding to $T_{iorc,in,i}$.

Subsequently, is followed the same procedure with the previous case by using the tank's function and computing $T_{icol,in,i+1}$ and $T_{iorc,in,i+1}$.

Based on these conditions (one for each sub-loop), derive four cases concerning the operation of the solar system. Finally, apart from these four basic cases that are examined in order to solve the system, there is another condition that needs to be taken into consideration and has to do with the maximum acceptable temperature of the thermal oil in the stream exiting the collectors' loop. This limit is specified according to the operational range of the collectors as well as the behavior of the used synthetic oil.

Concerning PTCs, they are mostly used in applications in which the maximum temperature can reach values up to 400 ^{o}C at their focal line [40, 81]. However, in cases of small and medium units their usual maximum working temperature lies around 250 ^{o}C, without exceeding 300^{o}C [82]. On the contrary, in many case PDCs are coupled with a two axes tracking system and a point receiver enabling them to reach excessively high temperatures even beyond 1500^{o}C [83]. However, in most common applications an indicative operational temperature range is limited at around 500 ^{o}C. Another factor that induces limitations regarding the maximum temperature that the system can handle is the thermal stability and performance of the thermal fluid. As it was previously described and demonstrated in Figure 2.3 as well, Therminol VP1 operates optimally for temperatures up to $400^{o}C$. Bearing in mind the above restrictions, the temperature limit for PTCs is set at $T_{max,PTC} = 300^{o}C$, whereas for PDCs the constraint is determined by the intermediate fluid and thus set at $T_{max,PDC} = 400^{o}$. Hence, in case the collectors' outlet stream ($T_{col,out,i}$) has temperature that exceeds the aforementioned limits, the above temperature is imposed to be equal to its maximum acceptable value. With this value and according to equation (2.18) the collectors' absorbed heat ($Q_{col,i}$) is calculated and subsequently their thermal efficiency ($\eta_{col,i}$, equation (2.17)).

Based on the above analysis and the described procedure, a model was developed in Matlab that uses the meteorological data, the solar results deduced from them and the simulating functions of the solar collectors and the storage tank.

The results that derive from this model are presented below in Figure 2.12 and Figure 2.13. These figures illustrate the fluctuation of the temperature that exits the collectors' loop and the heat produced by the collectors respectively on an annual period using an hourly time step. In the figures, for each of the five selected cities is demonstrated indicatively the case of PTCs, since there is no notable difference in the results between the two types of collectors.

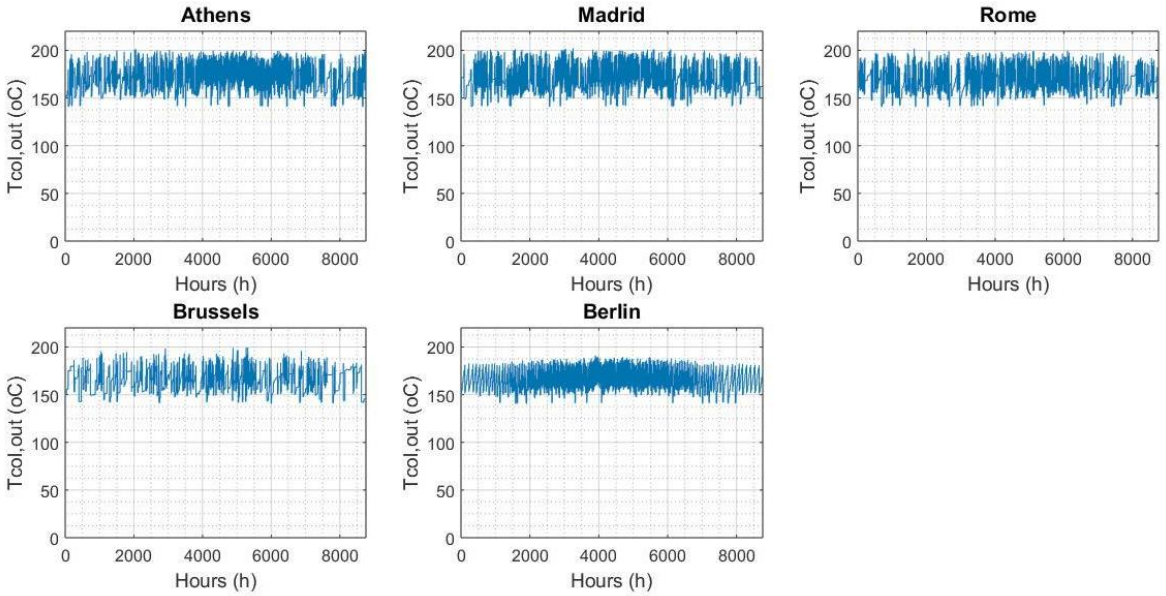

Figure 2.12: Temperature of the collectors' outlet stream in case of PTCs, for every hour of the year of each city

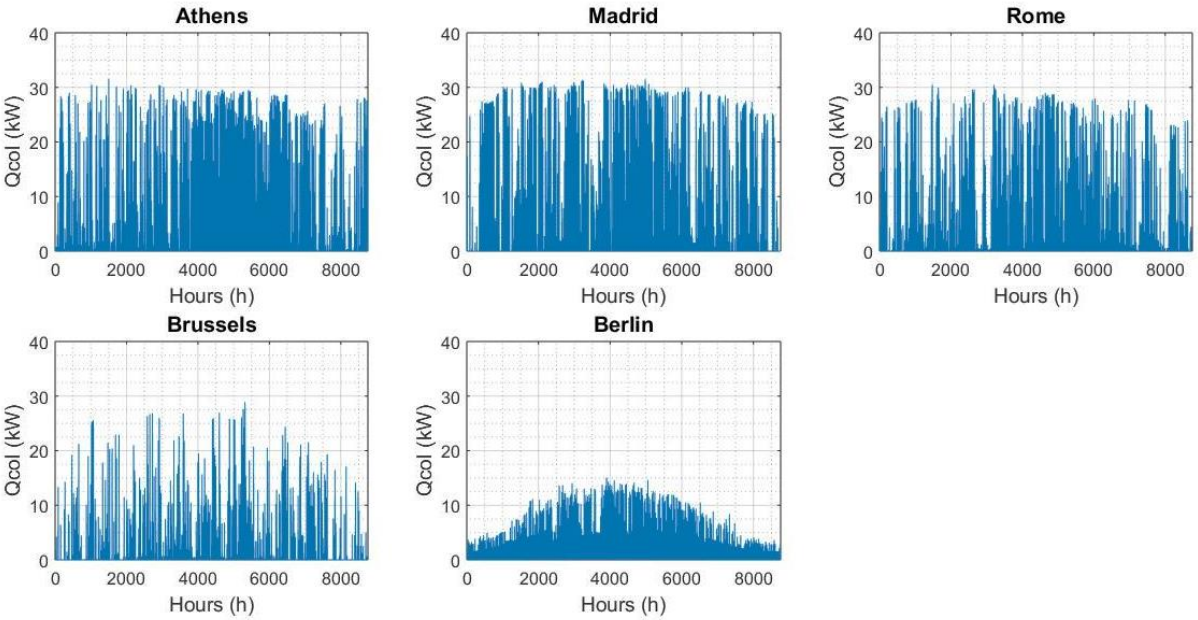

Figure 2.13: Heat absorbed by PTCs, for every hour of the year of each city

As shown in Figure 2.12 above, the upper limit that was set for the maximum allowed temperature does not affect the produced results. The values that were chosen for the constant parameters (mass flow rates, absorbed heat, collectors' surface etc.) do not insert a high temperature raise. However, the limit is set and might be applicable later in this study, since in the optimization process there will be examined the function and the performance of the whole system with respect to the variation of some of the selected parameters, which may generate different temperature profiles.

Furthermore, for the determined surface of the collectors the absorbed heat by the collectors is relatively low compared to the imposed value of the power that receives the ORC system, which is set equal to $Q_{iorc} = 40\ kW$, as depicted in Figure 2.13.

Consequently, it needs to be ensured that for every hourly point the sum of the total accumulated heat by the collectors up to this moment is greater than the corresponding sum of the total heat absorbed by the ORC system, which means that there is no logical fault inserted at the developed model due to the constant value of the absorbed power. This can be observed also from the Figure 2.14 below, that demonstrates the difference between these two described sums, which can be considered as the total stored heat of the system.

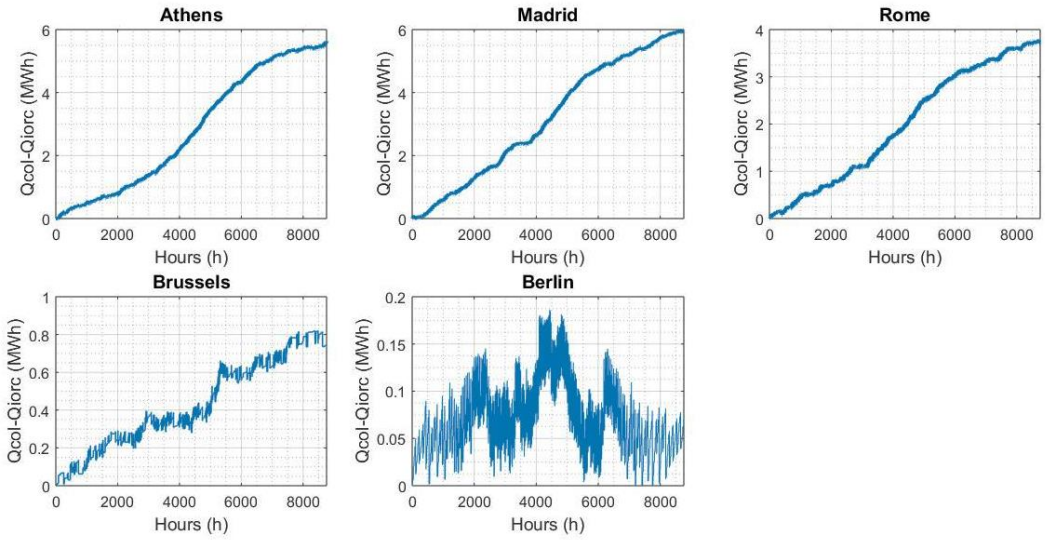

Figure 2.14: Total produced energy minus total consumed energy, for every hour of the year of each city

For the southern selected cities (Athens, Madrid, Rome) the solar irradiance and thus the accumulated energy is high enough to ensure that there is an increasing value of the stored energy. Nevertheless, for Brussels and Berlin because of the significantly lower solar potential, there is not enough total energy, leading to a higher fluctuation of the stored heat.

The whole modelling procedure regarding the collectors' system is described in the following flow chart:

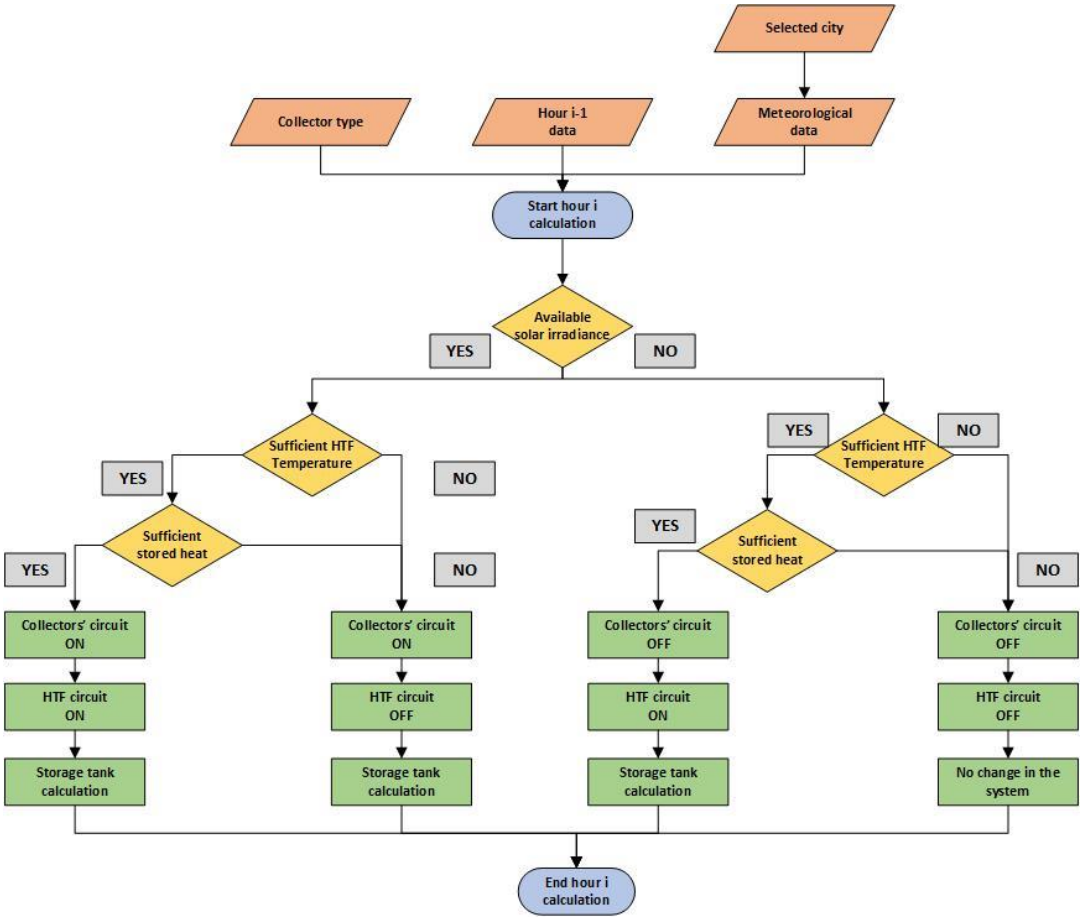

Figure 2.15: Flow chart of the solar collectors modelling procedure

Chapter 3. Organic Rankine Cycle (ORC)

3.1. ORC modelling

The configuration of an ORC unit, as well as its basic components and the process performed by each one of them have already been presented in Chapter 1. This chapter focuses on modelling separately the components that constitute the cycle, as well as the development of a code that simulates its operation.

The layout of the studied circuit is similar to Figure 1.4 and consists of the four basic parts (evaporator, expander, condenser, pump) of a typical Rankine cycle. Since in this study the working temperature range is relatively high for solar applications, it may be thermodynamically and economically profitable to insert a recuperator in order to increase the exploitation of the available heat and to increase the total thermal efficiency.

In the following Figure 3.1 is presented an indicative T-s diagram of an ORC system (with recuperator).

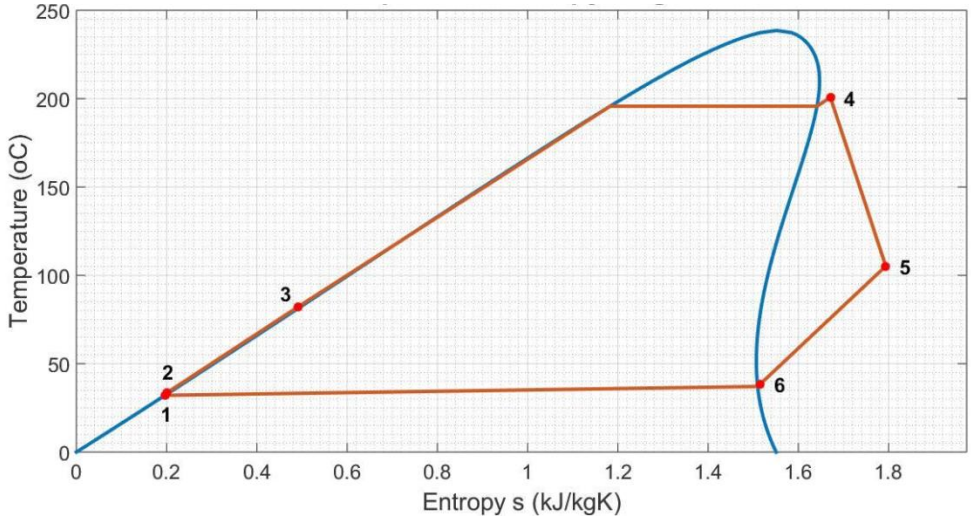

Figure 3.1: Indicative T-s diagram for an ORC system

In the following paragraphs are presented the models for the sizing of each one of the aforementioned components and the calculation of the thermodynamic processes that they perform.

3.2. Heat exchangers

Heat exchanger is a device that is used to transfer heat between two fluids at different temperatures. Based on the relative flow of the two fluids inside this component, they are distinguished to Parallel flow, Counterflow and Crossflow heat exchangers [84].

The most commonly selected type of heat exchanger used in a large range of applications is shell and tube heat exchanger, since it can perform effectively up to conditions of high pressure and temperature, as shown in Figure 3.2 , for fluids of either liquid or gaseous phase. This type of heat exchangers consist of a vessel (shell) in which cylindrical tubes are placed in a direction parallel to the shell's axis [85]. The hot fluid usually moves along the tubes, whereas the cold one flows around the tubes inside the shell, achieving the heat transfer. Depending on the application and the needed heat flow, the appropriate number of tubes is defined in order to obtain the exchange surface needed. They are used in industry in operating conditions that vary from high vacuum pressure up to 1000 bar, from cryogenic temperatures up to 1100 ^{o}C and in every desirable size [86]. However, since they are non-compact heat exchangers, they have higher spatial and cost requirements compared to the compact ones.

The second most widely used category of heat transfer devices is plate heat exchangers. They consist of a number of thin, usually rectangular, metal plates that are placed successively one after the other and form a plate pack that is held together in a frame, as shown in Figure 3.3. The pack is sealed around the edges with the use of elastomeric gaskets and along with the end covers are clamped together by bolts (gasketed PHE) [86]. The plates used in most heat exchangers are not completely smooth, but they form some kind of corrugations increasing in that way the exchange surface at both sides of each metal plate and enhancing the heat exchange between the two fluids [86].

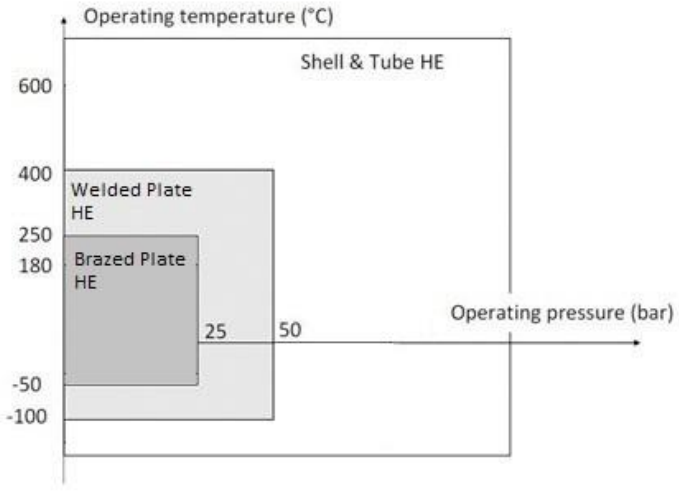

Figure 3.2: Heat exchangers working range

The main disadvantage of plate heat exchangers compared to shell and tube is their operation conditions that are subject to great restrictions contrary to the previous type, since the maximum pressure and temperature are limited to around 25 bar and 260 ^{o}C respectively (Figure 3.2). These limitations could be partially overcome by removing the plates' gaskets

and substitute them with a welded pair of plates (welded PHE). In that way the operating interval is broadened, but the disassembling flexibility is lost due to the welded sides [86].

Nevertheless, the main advantage of plate heat exchangers is their relatively high heat transfer coefficient compared to shell and tube. Because of that, their size could be much smaller leading to more compact and robust components with great spatial, weight and cost benefits mainly in case of small-scale configurations [87].

According to the aforementioned characteristics of each type of heat exchangers and since the developed operation conditions in our system do not reach high values, it was chosen to use plate heat exchangers.

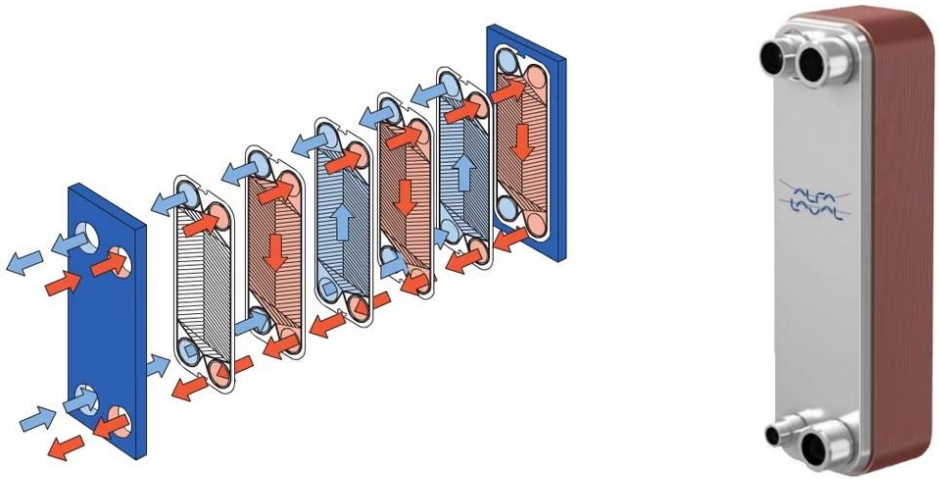

(a) (b)

Figure 3.3: (a) Representation of plate heat exchanger flow (b) Plate heat exchanger from Alfa Laval [88]

3.2.1 Evaporator modelling

I. Heat transfer surface calculation

The evaporator is coupling the solar collectors' circuit with the ORC system by transferring the acquired heat from the storage tank to the working fluid. Hence, its hot stream consists of the thermal oil Therminol VP1 that flows in the solar loop in a temperature range around 200^{o}C, as shown in the figures of the previous chapter that describes the heat source system. The evaporator's developed model aims at sizing the plate heat exchanger and calculating its main geometry as well as the heat transfer and pressure drop values of the process.

In order to perform these calculations, it is used as input of the function the thermodynamic values (temperature and pressure) of the cold stream (ORC fluid) both at its inlet and outlet and the specification of the selected working fluid. Furthermore, is required the inlet state of

the hot stream (Therminol VP1) as well as the mass flow rates in both sides of the heat exchanger ($\dot{m}_h$ and $\dot{m}_c$).

Since the properties of the cold stream are known the corresponding enthalpies (h_c^{in} and h_c^{out}) can be determined, using Coolprop database [89]. Similarly, for the hot stream's inlet is defined h_h^{in}.

With the mass flow rates already specified, the heat duty is specified and with an energy balance at the heat exchanger the following is extracted:

$$\dot{m}_c\left(h_c^{out} - h_c^{in}\right) = \dot{m}_h\left(h_h^{in} - h_h^{out}\right) \Rightarrow h_h^{out} = h_h^{in} - \frac{\dot{m}_c}{\dot{m}_h}\left(h_c^{out} - h_c^{in}\right) \quad (3.1)$$

with $$Q_{exch} = \dot{m}_c\left(h_c^{out} - h_c^{in}\right) = \dot{m}_h\left(h_h^{in} - h_h^{out}\right) \quad (3.2)$$

In which indices h and c are used for the hot and cold stream, respectively.

In order to proceed to the heat transfer analysis, some basic geometric characteristics of the plates have to be assumed. A typical plate heat exchanger is considered with chevron-bone plates whose values are presented in Table 3.1 below and can also be observed in the schematic in Figure 3.4.

Table 3.1: Basic common geometric characteristics of plate heat exchangers

Property	Value
Number of passes	$N_p = 1$
Plate thickness (mm)	$t = 0.7$
Chevron angle (deg)	$\beta = 60$
Pitch (mm)	$p = 2.5$
Plate amplitude (mm)	$a_{pl} = 1$
Corrugation pitch (mm)	$\Lambda = 7$

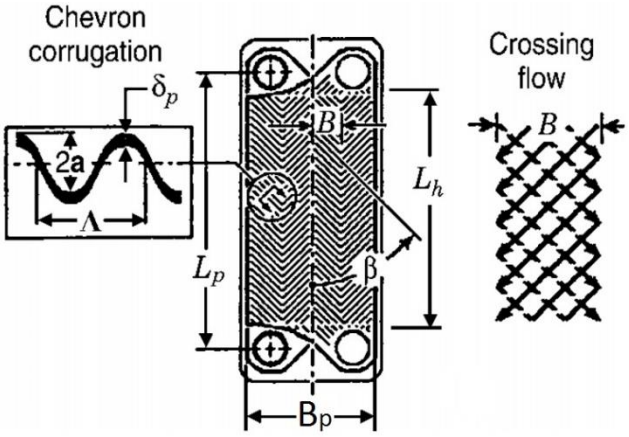

Figure 3.4: Geometrical parameters of a chevron plate [90]

Apart from the above considered typical values, the rest of the geometrical data required for the calculations derive from the technical datasheets of the commercial heat exchangers that were selected in order to be studied. Four commercial models from Alfa Laval are considered as alternatives for the system and are listed below in the table, along with their basic geometric data.

Table 3.2: Basic geometric characteristics of Alfa Laval plate heat exchangers for the evaporator

Model	Port diameter D_p (mm)	Vertical plate length L_p (mm)	Horizontal distance between nozzles B_p (mm)	Available number of plates (min-max)	Maximum mass flowrate (m^3/h)
AC30EQ [88]	20	269	95	4-120	8.8
AC70X [91]	20	466	111	4-124	14
AC112 [92]	20	519	191	10-300	51
CB200 [93]	40	624	324	10-230	128

In order to specify the required heat transfer surface and the corresponding number of plates the surface of a single plate needs to be determined. Ignoring the surface corrugations, the plain plate surface is equal to:

$$A_{ref} = L_p \cdot B_p \quad (3.3)$$

Whereas, the single plate heat transfer area which takes into consideration the corrugations:

$$A_p = A_{ref} \cdot \Phi \quad (3.4)$$

With Φ being the enlargement factor calculated as follows [94]:

$$\Phi = \frac{1}{6}\left(1 + \sqrt{1 + X^2} + 4\sqrt{1 + \frac{X^2}{2}}\right) \quad (3.5)$$

where $X = 2\,\pi \frac{a_{pl}}{\Lambda}$ (3.6)

The hydraulic diameter of the plate is given by the formula:

$$D_h = 4 \frac{a_{pl}}{\Phi} \quad (3.7)$$

On the other hand, the thermal conductivity of the plates' material, which are made of stainless steel, is equal to $k_w = 16.2 \frac{W}{mK}$.

Finally, it is crucial to compute the mass velocity of each fluid per stream and the corresponding value at the inlet and outlet ports.

For the channels (hot stream):

$$G_{ch,h} = \frac{\dot{m}_{ch,h}}{A_{ch}} \quad (3.8)$$

where $\dot{m}_{ch,h}$ is the mass flow rate of the hot stream per channel and $A_{ch,h}$ the channel's surface and derive from:

$$\dot{m}_{ch,h} = \frac{\dot{m}_h}{Ncp} \quad (3.9)$$

$$A_{ch} = 2 \cdot a_{pl} \cdot B_p \quad (3.10)$$

in which $\dot{m}_h$ is the already defined mass flow rate of the hot stream and N_{cp} the number of channels per pass and is equal to

$$N_{cp} = \frac{N_t - 1}{2 \cdot N_p} \quad (3.11)$$

with N_t the total number of plates in the heat exchanger that needs to be determined and N_p the number of passes as already mentioned.

For the ports (hot stream):

$$G_{port,h} = \frac{\dot{m}_h}{A_{port}} \quad (3.12)$$

where $\dot{m}_h$ is the total mass flow rate and

$$A_{port} = \pi \frac{D_p^2}{4} \quad (3.13)$$

the ports' cross section.

Similarly, the cold stream calculations are conducted.

The analysis of the heat exchanger focuses on calculating the heat transfer and the pressure drop, based on separating the heat transfer process in three distinguished zones, namely the economizer, the evaporator and the superheater. As shown in the Figure 3.5 , the economizer consists of the preheating of the fluid from the state of subcooled liquid until it reaches the evaporation temperature in state of saturated liquid. Subsequently, in evaporator takes place

the phase change process until the state of saturated gas and is followed by the superheater that raises the fluid's temperature above the boiling one.

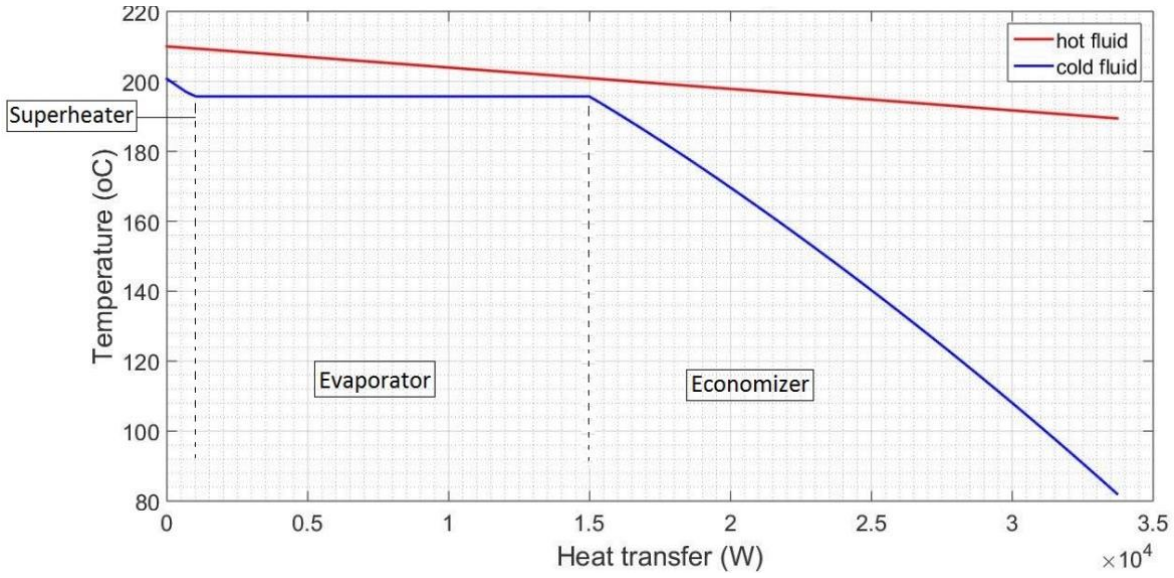

Figure 3.5: Heat-temperature diagram and evaporator's distinctive zones

In the cases of the pre- and super-heating, there is no phase change of the cold stream, hence only the initial and final states are taken into consideration. However, in the evaporation zone takes place the fluid's phase change and thus its properties are highly alternating depending on the quality. As a result, the middle zone is discretized in ten finite elements assuming a linear change of their quality as it increases from zero (saturated liquid) to one (saturated gas). Below is analyzed the developed model for each one of the distinctive parts of the evaporator.

Pre-heating:

Since this zone is solved as a single element, only the initial and final states of the two streams need to be defined, thus because the pressure is already known and equal to the evaporator's pressure (p_{evap}), their temperature and enthalpy should be calculated.

For the cold stream the inlet is equal to the evaporator's inlet, whereas for the outlet the pressure and the fluid's quality are known and the other values are specified:

$$h_{c,preheat}^{in} = h_{c}^{in} \quad (3.14)$$

$$h_{c,preheat}^{out} = h(p_{evap}, x = 0) \quad (3.15)$$

As for the hot stream, the output is equal to the total output of the evaporator and for the inlet is used an energy balance in the preheater:

$$h_{h,preheat}^{out} = h_{h}^{out} \quad (3.16)$$

$$Q_{preheat} = \dot{m}_c\left(h^{out}_{c,preheat} - h^{in}_{c,preheat}\right) = \dot{m}_h\left(h^{in}_{h,preheat} - h^{out}_{h,preheat}\right) \Rightarrow$$

$$h^{in}_{h,preheat} = h^{out}_{h,preheat} + \frac{\dot{m}_c}{\dot{m}_h}\left(h^{out}_{c,preheat} - h^{in}_{c,preheat}\right) \quad (3.17)$$

From the above values using Coolprop can be calculated the corresponding temperatures which will be used to compute the appropriate heat exchange surface. For that, is used the Logarithmic Mean Temperature Difference (ΔT_{lm}) method.

The logarithmic mean temperature difference is equal to:

$$\Delta T_{lm,preheat} = \frac{\left(T^{in}_{h,preheat} - T^{out}_{c,preheat}\right) - \left(T^{out}_{h,preheat} - T^{in}_{c,preheat}\right)}{\ln\left(\frac{T^{in}_{h,preheat} - T^{out}_{c,preheat}}{T^{out}_{h,preheat} - T^{in}_{c,preheat}}\right)} \quad (3.18)$$

Subsequently, in order to determine the heat transfer coefficients, the calculation of the Reynolds, Prandtl and Nusselt numbers is necessary. Before that is needed an initial estimation of the mean temperatures of the hot and cold fluid which will be used for the above numbers. Thus:

$$\bar{T}_{c,preheat} = \frac{T^{in}_{c,preheat} + T^{out}_{c,preheat}}{2} \quad (3.19)$$

$$\bar{T}_{h,preheat} = \frac{T^{in}_{h,preheat} + T^{out}_{h,preheat}}{2} \quad (3.20)$$

For the hot stream the Reynolds number derives from:

$$Re_{h,preheat} = \frac{G_{ch,h} \cdot D_h}{\mu_{h,preheat}} \quad (3.21)$$

For the Prandtl number:

$$Pr_{h,preheat} = \frac{\mu_{h,preheat} \cdot Cp_{h,preheat}}{k_{h,preheat}} \quad (3.22)$$

in which $\mu_{h,preheat}, Cp_{h,preheat}, k_{h,preheat}$ are the dynamic viscosity, the specific heat and the thermal conductivity of the hot fluid, respectively, that are computed using Coolprop for the mean conditions equation (3.20).

With these values, and by using the correlation of Donowski and Kandlikar [95], is calculated the Nusselt number:

$$Nu_{h,preheat} = 0.2875 \cdot Pr_{h,preheat}^{\frac{1}{3}} \cdot Re_{h,preheat}^{0.78} \quad (3.23)$$

and from that the total heat transfer coefficient for the hot side:

$$a_{h,preheat} = \frac{Nu_{h,preheat} \cdot k_{h,preheat}}{D_h} \quad (3.24)$$

Similarly, for the computations of the cold side are used the aforementioned equations for the corresponding values that characterize the cold stream. Thus, by combining equations

(3.21-3.24) and substituting equation (3.19) for the mean temperature, is defined the total heat transfer coefficient for the cold side, $a_{c,preheat}$.

Therefore, it is now possible to estimate the value of the overall heat transfer coefficient for the preheater:

$$U_{preheat} = \frac{1}{\frac{1}{a_{h,preheat}}+\frac{1}{a_{c,preheat}}+\frac{t}{k_w}+R_{f,h}+R_{f,c}} \quad (3.25)$$

in which $R_{f,h}$ and $R_{f,c}$ are the fouling resistances for the hot and cold side and have values equal to $R_{f,h} = R_{f,c} = 0.00017\frac{m^2K}{W}$ and t and k_w are already defined.

Finally, for the required heat transfer surface of the preheater:

$$Q_{preheat} = \Delta T_{lm,preheat} \cdot U_{preheat} \cdot A_{preheat} \Rightarrow$$

$$A_{preheat} = \frac{Q_{preheat}}{\Delta T_{lm,preheat} \cdot U_{preheat}} \quad (3.26)$$

Combining equations 3.17, 3.18, 3.25 and 3.26 derives the desired surface.

Evaporation:

As already mentioned, the analysis of the evaporation zone is based on its discretization in ten elements whose quality is changing linearly from state of saturated liquid (x=0 -outlet of the preheater) up to saturated gas (x=1 - inlet of superheater).

Thus for every element n the following applies: Since its quality is known both at the inlet and the outlet and the pressure (p_{evap}) is also known, its enthalpy in both sides can be calculated (the temperature is known and remains steady inside the two-phase region).

$$h_{c,vap}^{in}(n) = h(p_{evap}, x = x(n)) \quad (3.27)$$

$$h_{c,vap}^{out}(n) = h(p_{evap}, x = x(n+1)) \quad (3.28)$$

with n varying from 1 to 10 since there are ten elements and $x(1) = 0, x(11) = 1$.

Concerning the hot side, the outlet of the first element is equal to the inlet of the preheater that is already calculated:

$$h_{h,vap}^{out}(1) = h_{h,preheat}^{in} \quad (3.29)$$

And with an energy balance of the first element are defined the properties of the inlet of the first element which is also the outlet of the second one:

$$Q_{vap}(1) = \dot{m}_c\left(h_{c,vap}^{out}(1) - h_{c,vap}^{in}(1)\right) = \dot{m}_h\left(h_{h,vap}^{in}(1) - h_{h,vap}^{out}(1)\right) \Rightarrow$$

$$h_{h,vap}^{in}(1) = h_{h,vap}^{out}(2) = h_{h,vap}^{out}(1) + \frac{\dot{m}_c}{\dot{m}_h}\left(h_{c,vap}^{out}(1) - h_{c,vap}^{in}(1)\right) \quad (3.30)$$

Obviously, in that way starting from the first element successively are computed at first the outlet of each element as the inlet of the previous one:

$$h_{h,vap}^{out}(n) = h_{h,vap}^{out}(n-1) \quad (3.31)$$

And with an energy balance its inlet:

$$Q_{vap}(n) = \dot{m}_c\left(h_{c,vap}^{out}(n) - h_{c,vap}^{in}(n)\right) = \dot{m}_h\left(h_{h,vap}^{in}(n) - h_{h,vap}^{out}(n)\right) \Rightarrow$$

$$h_{h,vap}^{in}(n) = h_{h,vap}^{out}(n) + \frac{\dot{m}_c}{\dot{m}_h}\left(h_{c,vap}^{out}(n) - h_{c,vap}^{in}(n)\right) \quad (3.32)$$

Finally, with Coolprop is computed the corresponding temperatures of the hot stream.

Since all the required temperatures have been defined, equation (3.18) is used in order to calculate the logarithmic mean temperature difference for the evaporating zone ($\Delta T_{lm,vap}(n)$).

Regarding the hot side in which there is no phase change process and the fluid is simply cooled down in the same way that it took place in the preheater, the previous formulas are applied as well. From equations (3.20-3.24), are determined Reynolds, Prandtl and Nusselt numbers and finally the heat transfer coefficient of the hot side for each element ($a_{h,vap}(n)$).

However, for the cold side which undergoes a two-phase heating process, the equations used above are not applicable. Hence, equivalent values based on the quality of each element are calculated. For the equivalent mass flux per channel:

$$G_{ch,c,eq}(n) = G_{ch,c} \cdot \left[1 - x(n) + x(n) \cdot \sqrt{\frac{\rho_L}{\rho_g}}\right] \quad (3.33)$$

in which ρ_L and ρ_g are the densities of the saturated liquid and gas respectively.

The equivalent Reynolds number for the state of saturated liquid uses the dynamic viscosity for x=0 and derives from:

$$Re_{c,L} = \frac{G_{ch,c} \cdot D_h}{\mu_{c,L}} \quad (3.34)$$

Furthermore, is computed the equivalent Prandtl number of saturated liquid:

$$Pr_{c,L} = \frac{\mu_{c,L} \cdot Cp_{c,L}}{k_{c,L}} \quad (3.35)$$

Finally, the equivalent Boiling number needs to be defined:

$$Bo_{c,eq}(n) = \frac{\Delta T_{lm,vap}(n) \cdot U_{vap}(n)}{G_{ch,c,eq}(n) \cdot \left[h_{c,vap}^{out}(n) - h_{c,vap}^{in}(n)\right]} \quad (3.36)$$

Combining equations (3.34-3.36) and using the correlation of Yan and Lin [96] derives the Nusselt number:

$$Nu_{c,vap}(n) = 19.26 \cdot {Re_{c,L}}^{0.5} \cdot Bo_{c,eq}(n)^{0.3} \cdot {Pr_{c,L}}^{\frac{1}{3}} \quad (3.37)$$

and from that the total heat transfer coefficient for the cold side:

$$a_{c,vap}(n) = \frac{Nu_{c,vap}(n) \cdot k_{c,vap}}{D_h} \quad (3.38)$$

Therefore, using equation (3.25) is estimated the value of the overall heat transfer coefficient for the evaporation zone ($U_{vap}(n)$).

This procedure cannot be straightforward, since $U_{vap}(n)$ is used both in equations (3.25) and (3.36). So, a guess for the initial value for the heat transfer coefficient is needed and then the calculation is repeated imposing the derived $U_{vap}(n)$ again in equation (3.36), until it converges to the final result with negligible error.

Finally, for the required heat transfer surface of each element:

$$Q_{vap}(n) = \Delta T_{lm,vap}(n) \cdot U_{vap}(n) \cdot A_{vap}(n) \Rightarrow \; A_{vap}(n) = \frac{Q_{vap}(n)}{\Delta T_{lm,vap}(n) \cdot U_{vap}(n)} \quad (3.39)$$

With the calculated surface for each element derives the total desired surface for the evaporation zone:

$$A_{vap} = \sum A_{vap}(n) \quad (3.40)$$

Superheating:

For the superheating part the analysis is similar to the preheating one since the heat transfer takes place in a single phase and thus this zone is solved as a single element. The thermodynamic values of the inlet and outlet of both fluids are already known from the previous calculations as well as from the function's inputs. Thus:

$$Q_{supheat} = \dot{m}_c\left(h^{out}_{c,supheat} - h^{in}_{c,supheat}\right) = \dot{m}_h\left(h^{in}_{h,supheat} - h^{out}_{h,supheat}\right) \quad (3.41)$$

Following the same procedure and applying successively equations (3.18-3.25) $a_{c,supheat}$, $a_{h,supheat}$ and $U_{supheat}$ are defined.

Finally, is determined the required heat transfer surface for the superheater:

$$Q_{supheat} = \Delta T_{lm,supheat} \cdot U_{supheat} \cdot A_{supheat} \Rightarrow$$

$$A_{supheat} = \frac{Q_{supheat}}{\Delta T_{lm,supheat} \cdot U_{supheat}} \quad (3.42)$$

The total heat transfer surface needed is equal to the sum of the surface of the three zones that constitute the evaporator. Combining equations (3.26), (3.40), (3.42):

$$A_{evap} = A_{preheat} + A_{vap} + A_{supheat} \tag{3.43}$$

II. Pressure drop calculation

Apart from the heat transfer surface, the second value that characterizes the heat exchanger's operation is the pressure drop. The occurring reduction in pressure affects the exiting stream of the exchanger and thus alters the function of the following components requiring probably the adjustment of their operational conditions, especially for the pump and the expansion machines.

Similar to the heat transfer coefficients, the pressure drop expressions differ in case of single- and two-phase processes. Hence, different equations are applied for the case of the single phase pre- and super-heating zones compared with the two-phase evaporating zone.

Therefore, the pressure drop inside the channels of each part of the heat exchanger needs to be found. For the preheater, the Darcy's friction coefficient (ξ) is computed using the expression that gives [94]:

$$\frac{1}{\sqrt{\xi}} = \frac{\cos(\beta)}{\sqrt{018\cdot\tan(\beta)+0.36\cdot sin(\beta)+\frac{\xi_o}{\cos(\beta)}}} + \frac{1-\cos(\beta)}{\sqrt{\xi_1}} \tag{3.44}$$

In the above equation the parameters ξ_0 and ξ_1 are determined according to the Reynolds number [94]:

$$\xi_0 = \begin{cases} \frac{64}{Re}, & for\ Re < 2000 \\ (1.8 \cdot \log_{10} Re - 1.5)^{-2}, & for\ Re > 2000 \end{cases} \tag{3.45}$$

$$\xi_1 = \begin{cases} \frac{597}{Re} + 3.85, & for\ Re < 2000 \\ \frac{39}{Re^{0.289}}, & for\ Re > 2000 \end{cases} \tag{3.46}$$

With the friction factor specified the pressure drop is calculated by applying the equation of Focke [97]:

$$\Delta p_{ch} = \frac{\xi \cdot L_p}{D_h} \cdot \frac{\rho \cdot {v_{ch}}^2}{2} \tag{3.47}$$

in which v_{ch} is the fluid's velocity deriving from:

$$v_{ch} = \frac{G_{ch}}{\rho} \tag{3.48}$$

Applying the above for the cold and the hot stream of the preheater and the superheater, derive the channels' pressure drop $\Delta p_{c,ch,preheat}$, $\Delta p_{c,ch,supheat}$, $\Delta p_{h,ch,preheat}$ and $\Delta p_{h,ch,supheat}$. Furthermore, concerning the hot stream at the evaporation zone are applied the aforementioned as well to compute $\Delta p_{h,ch,vap}$.

For the cold stream and the evaporation zone the procedure remains the same but is needed alternative correlations for the estimation of the friction factors since the Darcy's equation is not applicable. For this purpose, the analysis of the zone is the same as previously by dividing it into ten elements. In each one of them is applied the equation below, similar to equation (3.47) in which Darcy's coefficient is substituted by the friction factor (f). For one element n of the zone:

$$\Delta p_{ch}(n) = \frac{f \cdot L_p}{D_h} \cdot \frac{\rho \cdot {v_{ch}}^2}{2} \tag{3.49}$$

The friction factor derives from different expressions according to the range within which lies the Reynolds number [96, 98]

$$f(n) = \begin{cases} 6.1 \cdot 10^4 \cdot Re_{c,eq}(n)^{-1.25}, \ \ for\ Re_{c,L}(n) < 750 \\ 6.947 \cdot 10^5 \cdot Re_{c,L}(n)^{-0.5} \cdot Re_{c,eq}(n)^{-1.109}, \ \ for\ Re_{c,L}(n) \geq 750\ and\ \ Re_{c,eq}(n) < 6000 \\ 31.21 \cdot {Re_{c,L}}^{-0.5} \cdot {Re_{c,eq}}^{0.04557}\ , otherwise \end{cases} \tag{3.50}$$

Based on the above are computed the pressure for each element of the cold stream in the evaporation zone and from that the total pressure loss:

$$\Delta p_{c,ch,vap} = \sum \Delta p_{c,ch,vap}(n) \tag{3.51}$$

Combining equations (3.47) and (3.51), is estimated the total pressure drop inside the channels of both streams:

$$\Delta p_{c,ch,tot} = \Delta p_{c,ch,preheat} + \Delta p_{c,ch,vap} + \Delta p_{c,ch,supheat} \tag{3.52}$$

$$\Delta p_{h,ch,tot} = \Delta p_{h,ch,preheat} + \Delta p_{h,ch,vap} + \Delta p_{h,ch,supheat} \tag{3.53}$$

The total calculation requires also to bear in mind the pressure losses at the ports of each stream whose value is [99]:

$$\Delta p_{port} = 0.75 \cdot \frac{G_{port}^2}{\rho} \tag{3.54}$$

Finally, the overall results:

$$\Delta p_{c,tot} = \Delta p_{c,ch,tot} + \Delta p_{c,port} \tag{3.55}$$

$$\Delta p_{h,tot} = \Delta p_{h,ch,tot} + \Delta p_{h,port} \tag{3.56}$$

The evaporator's sizing process relies on selecting one of the aforementioned examined commercial models of heat exchangers that are presented in Table 3.2, and defining the appropriate number of plates in order to meet both the heat transfer and pressure drop requirements.

The above models are classified from the smallest to the largest one, in the order shown in the table. Starting from the smallest one and with its minimum acceptable number of plates,

is calculated the available heat transfer surface. Additional plates are added to the heat exchanger and increase the surface, until it becomes equal or greater than the required transfer area which derives from equation (3.43). If the total surface is not sufficient for the maximum number of plates of a specific model of heat exchanger, the larger one is studied until there is the appropriate combination of model and number of plates.

Nevertheless, in order to terminate the iterative process, it is not enough to reach the adequate exchange area, but it is also set an upper limit for the acceptable pressure drop of both streams. For the evaporator this limit is decided to be 15 kPa.

In the end of this procedure the function gives as output the selected model of heat exchanger, the required number of plates, the exchange surface, the pressure drop of both streams and the pinch point of the evaporator.

3.2.2 Condenser modelling

I. Heat transfer surface calculation

A similar model to the one developed above for the evaporator will be used for the condenser as well. Compared to the previous case the working fluid will be on the hot side of the heat exchange whereas water flows in the cold stream. The analysis will follow the same steps, as previously, having as controlling variables for the dimensioning of the condenser a sufficient heat transfer surface and a restricted value for the pressure losses.

The inputs of the function are the thermodynamic values (temperature and pressure) of the hot stream (ORC fluid) both at inlet and outlet, the selected working fluid and the mass flow rates of the two fluids ($\dot{m}_h$ and $\dot{m}_c$). Moreover, the inlet on the cold stream is set to be at 20°C and 2 bar, which are typical values used for the cooling water.

From these values is determined the corresponding enthalpies using Coolprop (h_h^{in} , h_h^{out} and h_c^{in}) and subsequently with an energy balance the transferred heat as well as the cold stream's outlet:

$$\dot{m}_c\left(h_c^{out} - h_c^{in}\right) = \dot{m}_h\left(h_h^{in} - h_h^{out}\right) \Rightarrow h_c^{out} = h_c^{in} + \frac{\dot{m}_h}{\dot{m}_c}\left(h_h^{in} - h_h^{out}\right) \quad (3.57)$$

with $$Q_{exch} = \dot{m}_c\left(h_c^{out} - h_c^{in}\right) = \dot{m}_h\left(h_h^{in} - h_h^{out}\right) \quad (3.58)$$

The commercial models examined for the condenser, are from Alfa Laval and are the same ones presented above for the evaporator and shown in Table 3.2 along with an additional smaller model, since the heat duty is slightly lower in case of the condenser. These models are demonstrated in Table 3.3 below with their basic dimensions:

Table 3.3: Basic geometric characteristics of Alfa Laval plate heat exchangers for the condenser

Model	Port diameter D_p (mm)	Vertical plate length L_p (mm)	Horizontal distance between nozzles B_p (mm)	Available number of plates (min-max)	Maximum mass flowrate (m^3/h)
CB30 [100]	20	250	113	4-150	14
AC30EQ [88]	20	269	95	4-120	8.8
AC70X [91]	20	466	111	4-124	14
AC112 [92]	20	519	191	10-300	51
CB200 [93]	40	624	324	10-230	128

The geometry of the considered plate heat exchanger is the same as for the evaporator and the dimensions used in the following calculations derive from Table 3.1, and from the sequent equations (3.3-3.13).

In the same way as for the evaporator, the heat transfer process needs to be categorized according to the state of the hot stream and its phase changes. The executed methodology follows the path of the ORC fluid as it moves along the three separate zones, the de-superheating, the condensing and the subcooling zone. As shown in Figure 3.6, the de-superheater cools down the superheated liquid until it reaches the state of saturated gas (x=1), it then condenses inside the condensing part (x=0) and enters the subcooler which lowers the final temperature of the hot fluid.

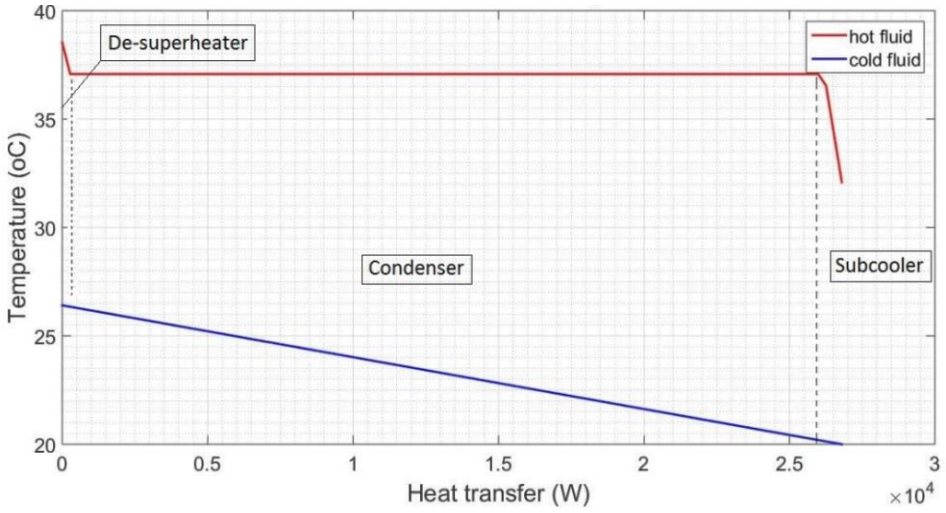

Figure 3.6: Heat-temperature diagram and condenser's distinctive zones

Based on the overall results of the condenser, is calculated firstly the de-superheater, whose output is used as an input for the condensing part which afterwards leads to the subcooler. Again, apart from the condensing part the other two regions carry out a single phase heat

transfer and thus they are handled as a single element. On the contrary, for the phase change region a discretization method is implemented, with ten elements that constitute the whole zone and have a linearly increasing quality.

<u>De-superheating:</u>

For this part, is known the hot stream's inlet, which is equal to the condenser's inlet, whereas in the outlet the fluid has a pressure equal to the whole condenser's pressure (p_{cond}) and an already defined quality, of saturated gas (x=1). Therefore:

$$h_{h,desup}^{in} = h_{h}^{in} \tag{3.59}$$

$$h_{h,desup}^{out} = h(p_{evap}, x = 1) \tag{3.60}$$

As for the cold stream, the output is equal to the total output of the heat exchanger and in order to define the inlet a simple energy balance can be performed:

$$h_{c,desup}^{out} = h_{c}^{out} \tag{3.61}$$

$$Q_{desup} = \dot{m}_c\left(h_{c,desup}^{out} - h_{c,desup}^{in}\right) = \dot{m}_h\left(h_{h,desup}^{in} - h_{h,desup}^{out}\right) \Rightarrow$$

$$h_{c,desup}^{in} = h_{c,desup}^{out} - \frac{\dot{m}_h}{\dot{m}_c}\left(h_{h,desup}^{in} - h_{h,desup}^{out}\right) \tag{3.62}$$

Since single phase transfer occurs, the same equations as for the evaporator's preheater (3.18-3.24) are applied and the overall heat transfer coefficient for the de-superheater is calculated:

$$U_{desup} = \frac{1}{\frac{1}{a_{h,desup}} + \frac{1}{a_{c,desup}} + \frac{t}{k_w} + R_{f,h} + R_{f,c}} \tag{3.63}$$

And the corresponding required heat transfer surface:

$$Q_{desup} = \Delta T_{lm,desup} \cdot U_{desup} \cdot A_{desup} \Rightarrow$$

$$A_{desup} = \frac{Q_{desup}}{\Delta T_{lm,desup} \cdot U_{desup}} \tag{3.64}$$

<u>Condensation:</u>

For the condensing region the hot stream's inlet state is at saturated gas (x=1 and de-superheater's outlet) and exits at saturated liquid (x=0 and inlet of subcooler). In every element there is an equal increase in the quality of the cold fluid and each element's output is the input for the next one.

Supposing an element n on the hot stream, in which are already known the quality both at the inlet and the outlet and the pressure (p_{cond}), its enthalpy in both sides can be computed:

$$h_{h,cond}^{in}(n) = h(p_{cond}, x = x(n)) \tag{3.65}$$

$$h_{h,cond}^{out}(n) = h(p_{cond}, x = x(n+1)) \quad (3.66)$$

with n varying from 1 to 10 since there are ten elements and $x(1) = 1, x(11) = 0$.

Concerning the cold side, the outlet of the first element is equal to the inlet of the de-superheater that is already calculated:

$$h_{c,cond}^{out}(1) = h_{c,desup}^{in} \quad (3.67)$$

And with an energy balance of the first element, are defined the properties of its inlet which is also the outlet of the second one. As demonstrated for the evaporator (equations 3.30-3.31) starting from the first element, successively are computed the states at both sides of all ten elements:

$$Q_{cond}(n) = \dot{m}_c\left(h_{c,cond}^{out}(n) - h_{c,cond}^{in}(n)\right) = \dot{m}_h\left(h_{h,cond}^{in}(n) - h_{h,cond}^{out}(n)\right) \Rightarrow$$

$$h_{c,cond}^{in}(n) = h_{c,cond}^{out}(n) - \frac{\dot{m}_h}{\dot{m}_c}\left(h_{h,cond}^{in}(n) - h_{h,cond}^{out}(n)\right) \quad (3.68)$$

For the cold side of the cooling water the same equations (3.18-3.24) are used once again for the heat transfer coefficient.

Regarding the two-phase region, is followed the same process with the evaporating one, but using a different correlation for the Nusselt number. The expressions for the equivalent mass flux and the liquid Reynolds and Prandtl numbers equations (3.33-3.35) are used.

Applying the correlation of Thonon [101] the Nusselt number is defined:

$$Nu_{h,cond}(n) = 1.564 \cdot 0.347 \cdot \frac{k_{h,cond}}{D_h} \cdot {Re_{h,eq}}^{-0.76} \cdot {Pr_{h,L}}^{\frac{1}{3}} \cdot {Re_{h,L}}^{0.653} \quad (3.69)$$

and from that the total heat transfer coefficient for the cold side $a_{h,cond}(n)$.

Therefore, using equation (3.25) is estimated the value of the overall heat transfer coefficient for the condensing element ($U_{cond}(n)$).

Finally, for the required heat transfer surface of each element:

$$Q_{cond}(n) = \Delta T_{lm,cond}(n) \cdot U_{cond}(n) \cdot A_{cond}(n) \Rightarrow \; A_{cond}(n) = \frac{Q_{cond}(n)}{\Delta T_{lm,cond}(n) \cdot U_{cond}(n)} \quad (3.70)$$

With the calculated surface for each element derives the total desired surface for the whole zone:

$$A_{cond} = \sum A_{cond}(n) \quad (3.71)$$

Subcooling:

In the subcooling part takes place a single phase change and an analysis similar to the de-superheating one. The thermodynamic values of the inlet and outlet of both fluids are already known from the previous zone, as well as from the function's inputs. Thus:

$$Q_{subcool} = \dot{m}_c\left(h^{out}_{c,subcool} - h^{in}_{c,subcool}\right) = \dot{m}_h\left(h^{in}_{h,subcool} - h^{out}_{h,subcool}\right) \quad (3.72)$$

Following the same procedure and applying successively equations (3.18-3.25) is defined $U_{subcool}$.

Finally, is determined the required heat transfer surface:

$$Q_{subcool} = \Delta T_{lm,subcool} \cdot U_{subcool} \cdot A_{subcool} \Rightarrow$$

$$A_{subcool} = \frac{Q_{subcool}}{\Delta T_{lm,subcool} \cdot U_{subcool}} \quad (3.73)$$

The total heat transfer surface needed is equal to the sum of the surface of the three zones that constitute the condenser. Combining equations (3.64), (3.71), (3.73):

$$A_{condenser} = A_{desup} + A_{cond} + A_{subcool} \quad (3.74)$$

II. Pressure drop calculation

The pressure drop assessment is based on the same principle applied in case of the evaporator. For the case of single phase change, thus for both streams of the de-superheater and subcooler and for the cold one in the condenser, the channels' pressure drop derives by using Thonon's friction factor [102]:

$$\xi = \begin{cases} 45.57 \cdot Re^{-0.67}, & for\ Re < 160 \\ 0.37 \cdot Re^{-0.172}, & for\ Re > 160 \end{cases} \quad (3.75)$$

With the friction factor specified and following the equations (3.47-3.48) is possible the calculation of the pressure drop (Δp_{ch}).

For the hot stream and the condensing zone, for every element is defined the friction factor according to the below formula and again using equation (3.49) to calculate (Δp_{ch}). For one element n of the zone [103]:

$$f(n) = Ge_3 \cdot {Re_{h,eq}}^{Ge_4} \quad (3.76)$$

With

$$Ge_3 = 3521.1 \cdot \left(\frac{\Lambda}{D_h}\right)^{4.17} \cdot \left(\frac{\pi}{2-\beta}\right)^{-7.75} \quad (3.77)$$

$$Ge_4 = 1.024 \cdot \left(\frac{\Lambda}{D_h}\right)^{0.0925} \cdot \left(\frac{\pi}{2-\beta}\right)^{-1.3} \quad (3.78)$$

Based on the above, derives the pressure for each element of the cold stream in the condensing zone and from that the total pressure loss similar to equation (3.51).

Combining the above results, the total pressure drops inside the channels of both streams are equal to:

$$\Delta p_{c,ch,tot} = \Delta p_{c,ch,desup} + \Delta p_{c,ch,cond} + \Delta p_{c,ch,subcool} \quad (3.79)$$

$$\Delta p_{h,ch,tot} = \Delta p_{h,ch,desup} + \Delta p_{h,ch,cond} + \Delta p_{h,ch,subcool} \quad (3.80)$$

Again, similar to the evaporator, the losses due to the ports of each stream (equation (3.54)) are added.

The condenser's sizing process is exactly the same with the evaporator's and has been already described in the previous paragraph. The strategy is to select the smallest commercial model of the available heat exchangers (Table 3.3) with the minimum number of plates that yields sufficient heat transfer surface to achieve the desired duty and inserts an acceptable pressure drop to the following components of the system (upper limit set at 10 kPa).

In the end of this procedure the function gives the selected model of heat exchanger, the required number of plates, the exchange surface, the pressure drop of both streams and the pinch point.

3.2.3 Recuperator modelling

I. Heat transfer surface calculation

As it has been already stated, since the ORC cycle works in relatively high temperatures it is important to study the thermal efficiency's enhancement with the implementation of a recuperator.

Since the outlet of the hot stream needs to be higher than the condenser's temperature, both streams of the recuperator do not undergo a phase change. Therefore, the analysis of this heat exchanger is simpler than the above two in which either one of the streams entered the two-phase region, as shown as well in the Q-T figure below.

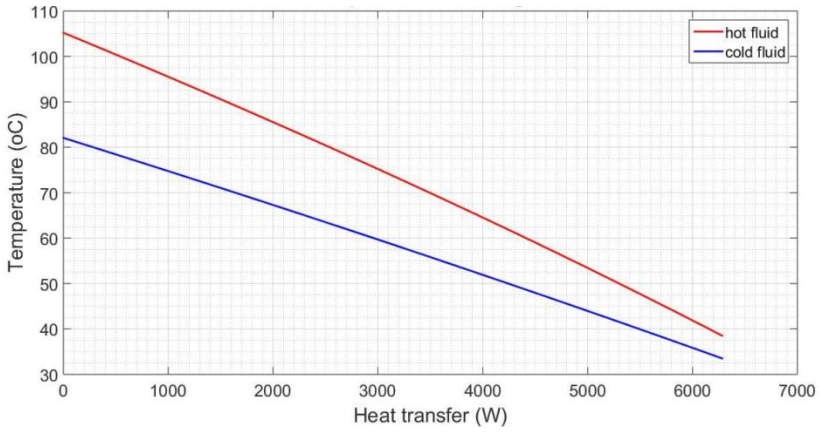

Figure 3.7: Heat-temperature diagram for recuperator

The developed function for the modelling uses as inputs the thermodynamic values (temperature and pressure) of the inlet of both streams (ORC fluid), the selected working fluid and the mass flow rates of the two fluids ($\dot{m}_h$ and $\dot{m}_c$). Furthermore, by setting a maximum pinch point is defined the outlet of the hot stream. By using these values and Coolprop it can be determined the corresponding enthalpies (h_h^{in} , h_h^{out} and h_c^{in}) and subsequently with an energy balance the transferred heat as well as the cold stream's outlet.

The selection process is done again by using as alternatives some commercial models from Alfa Laval. However, in case of a recuperator the required transfer heat is significantly lower than the corresponding for the evaporator and the condenser. Because of that, the considered models, whose characteristics and dimensions are presented in Table 3.4, are smaller than the previous ones.

Table 3.4: Basic geometric characteristics of Alfa Laval plate heat exchangers for the recuperator

Model	Port diameter D_p (mm)	Vertical plate length L_p (mm)	Horizontal distance between nozzles B_p (mm)	Available number of plates (min-max)	Maximum mass flowrate (m^3/h)
CB10 [104]	13	154	74	4-60	4.1
CB20 [105]	19	270	94	4-110	8.8
CB30 [100]	20	250	113	4-150	14
CB60 [106]	20	466	113	4-150	14

The geometry of the considered plate heat exchanger is the same as for the previous and their dimensions used in the following calculations derive from Table 3.1, and equations (3.3-3.13).

Since single phase transfer occurs, the same equations as for the previous single element zones (3.18-3.24) are applied for calculating the overall heat transfer coefficient for the recuperator:

$$U_{rec} = \frac{1}{\frac{1}{a_{h,rec}} + \frac{1}{a_{c,rec}} + \frac{t}{k_w} + R_{f,h} + R_{f,c}} \quad (3.81)$$

And the corresponding required heat transfer surface:

$$Q_{rec} = \Delta T_{lm,rec} \cdot U_{rec} \cdot A_{rec} \Rightarrow A_{rec} = \frac{Q_{rec}}{\Delta T_{lm,rec} \cdot U_{rec}} \quad (3.82)$$

II. Pressure drop calculation

Concerning the pressure drop, the calculations are based on the same correlations applied above. For both streams the channels' pressure drop derives by using Thonon's friction factor according to equation (3.75). With the friction factor specified and following the equations (3.47-3.48) is calculate the pressure drop (Δp_{ch}).

Finally, are included the losses due to the ports of each stream (equation (3.54)) and the overall results are:

$$\Delta p_{c,tot} = \Delta p_{c,ch,tot} + \Delta p_{c,port} \quad (3.83)$$

$$\Delta p_{h,tot} = \Delta p_{h,ch,tot} + \Delta p_{h,port} \quad (3.84)$$

The selection procedure is the same with the other heat exchangers. The function ends by defining the smallest of the considered commercial models (Table 3.4) with the minimum number of plates whose total surface covers the heat duty within an acceptable pressure drop range (upper limit set at 10 kPa).

In the end of this procedure the function gives the selected model of heat exchanger, the required number of plates, the exchange surface, the pressure drop of both streams and the recuperator's pinch point.

3.3. Pump

3.3.1 Diaphragm pump modelling

The next component that needs to be modeled is the pump in which enters the fluid when it exits the condenser, as shown in Figure 3.1. Concerning the outlet of the pump, that is either the inlet of the evaporator, in case of the simplest configuration of the cycle, or the inlet of the recuperator when sufficient heat can be used for the fluid's preheating as described previously.

The pump for the studied system is decided to be a positive displacement diaphragm pump, which is the most common choice in case of ORC systems. The main parts of a diaphragm pump are the driving shaft, the diaphragm and the check valves in suction and discharge sides,

as shown in Figure 3.8. below. As the shaft rotates a piston transfers the movement to the diaphragm which then compresses or decompresses the fluid existing inside the pump's main chamber. The flow is controlled by the two valves in the inlet and outlet of the pump. When the suction side's valve is open the fluid flows inside the chamber, while the piston recedes causing the diaphragm's deformation (Figure 3.8a). However, with the suction side sealed the piston displaces the diaphragm moving it back at its initial position and pushes the fluid out of the discharge port (Figure 3.8b).

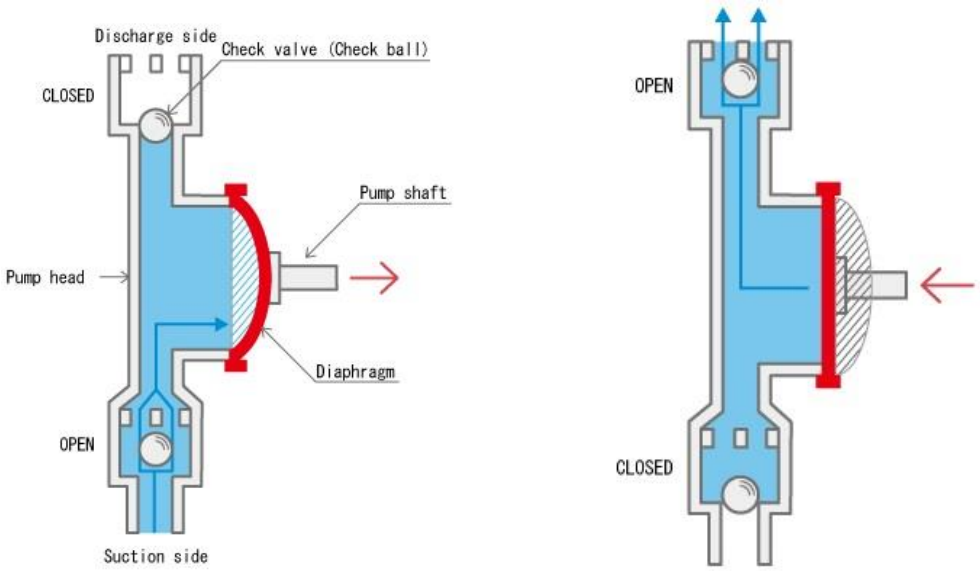

(a) (b)

Figure 3.8: (a) Suction and (b) discharge of a diaphragm pump

The finally selected commercially available pump is from Wanner Engineering, model Hydra Cell G25-E. Some basic parameters and characteristics of this pump are presented in Table 3.5 below, as they derive from its technical datasheet [107].

Table 3.5: Basic characteristics of Hydra Cell G25-E pump

Property	Value
Maximum flow rate (lt/min)	75.9
Maximum discharge pressure (bar)	69
Maximum inlet pressure (bar)	17
Maximum operating temperature (°C)	121

For the selected pump the manufacturer's datasheet provides a graph that correlates the volumetric flow rate with the rotational speed and is demonstrated below in Figure 3.9.

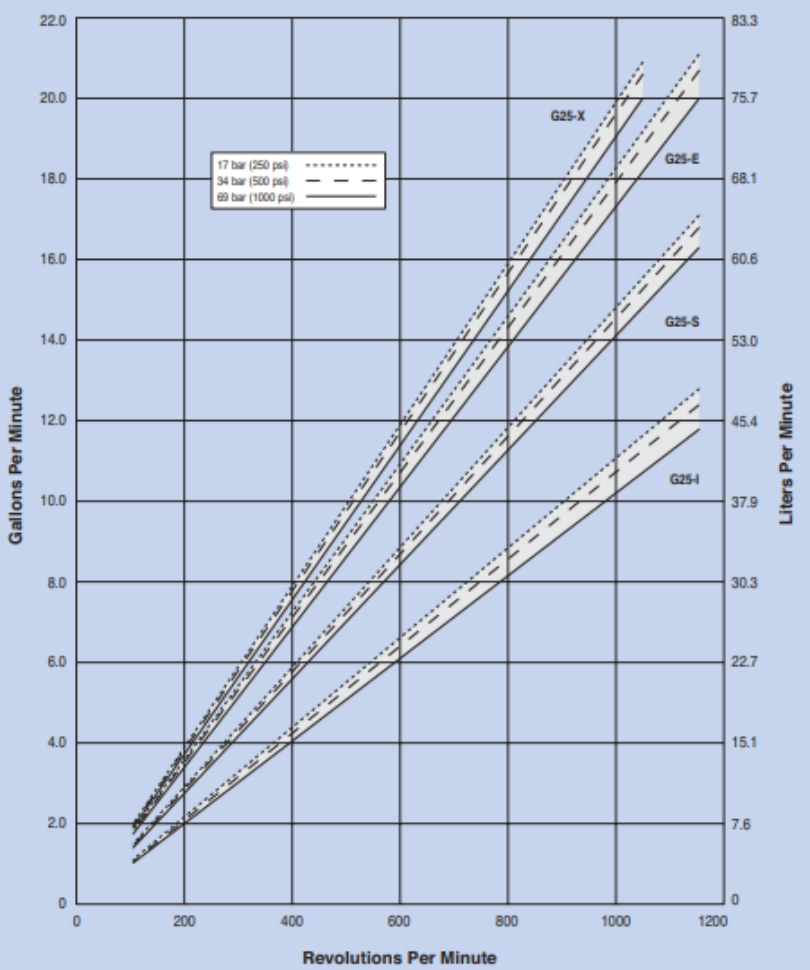

Figure 3.9: Pump's volumetric flow rate-rotational speed graph [107]

The developed function that describes the operation of the pump uses as input parameters the working fluid, the pressure of the stream that exits the pump, the mass flow rate and the thermodynamic properties of the entering stream, that have been already defined by the condenser, which is the previous component. Regarding the outlet pressure, it is equal to the existing pressure at the evaporator and is the cycle's upper pressure (p_{evap}).

From the above figure and the graph that refers to the selected pump, is estimated a polynomial function that fits the above given data. The polynomial fitting is demonstrated below in the corresponding function (equation (3.85)) from which derives the rotational speed (in rpm) with respect to the volumetric flow rate (in lt/min) for the working range set from the datasheet:

$$N_{pump} = 14.6574 \cdot \dot{V}_{pump} + 1.2586 \quad (3.85)$$

Since the inlet condition is defined as well as the circulating mass flow rate, is calculated the volumetric flow rate and using equation (3.85), the rotational speed (N_{pump}):

$$\dot{V}_{pump}^{in} = \frac{\dot{m}}{\rho^{in}} \quad (3.86)$$

According to the datasheet [107] the mechanical work produced by the pump can be computed using equation (3.87):

$$W_{mech,pump} = \frac{50 \cdot N_{pump}}{84428} \cdot \frac{\dot{V}_{pump}^{out} \cdot \Delta p}{511} \quad (3.87)$$

in which the work is calculated in kW, the flow rate in lt/min, the rotational speed in rpm, whereas $\Delta p = p^{out} - p^{in}$ is the pressure raise in bar.

Assuming that there are no energy losses in the pump, the produced mechanical work is transferred to the fluid leading to its enthalpy raise. Thus, the enthalpy for the pump's output derives from the equation below:

$$W_{mech,pump} = \dot{m}\left(h_{pump}^{out} - h_{pump}^{in}\right) \Rightarrow h_{pump}^{out} = h_{pump}^{in} + \frac{W_{mech,pump}}{\dot{m}} \quad (3.88)$$

In order to determine the properties of the output stream, as well as the work produced by the pump, an iterative procedure needs to be executed combining equations (3.85-3.88).

Since the outlet properties are defined, the isentropic enthalpy can be easily computed using the value of the entropy in the input and the high pressure and combine them in order to estimate the isentropic efficiency of the pump:

$$\eta_{is,pump} = \frac{h_{is,pump}^{out} - h_{pump}^{in}}{h_{pump}^{out} - h_{pump}^{in}} \quad (3.89)$$

Nevertheless, the electric power absorbed by the pump in order to achieve the desired pressure raise is not equal to the mechanical work as it derives from equation (3.87). The consumed energy depends on the electrical efficiencies of the motor and the inverter that are connected to the pump. The developed models for these two additional components are described below.

3.3.2 Motor and inverter modelling

The motor along with the inverter provide the required electric energy to the pump allowing at the same time the operation at a wide range of rotational speed. Their efficiency is estimated according to the expressions suggested by Ziviani [108]. The developed model calculates them as a polynomial approximation that depends on the speed, the power and the torque of the pump in their operating conditions with respect to the nominal ones.

In order to perform these calculations, the following variables should be introduced, regarding the speed, the power and the shaft's developed torque [109] respectively:

$$\widehat{N} = \frac{N}{N_{nom}} \quad (3.90)$$

$$\widehat{W} = \frac{W_{mech}}{W_{mech,nom}} \quad (3.91)$$

$$\hat{\tau} = \frac{\tau}{\tau_{nom}} \quad (3.92)$$

With $\tau = \frac{W_{mech}}{\frac{2\pi N}{60}}$ (3.93)

Combining equations (3.92) and (3.93): $\hat{\tau} = \frac{\frac{W_{mech}}{N}}{\frac{W_{mech,nom}}{N,nom}} = \frac{\widehat{W}}{\widehat{N}}$ (3.94)

For the motor's case, the correlation gives [108]:

$$\eta_{motor} = b_o + b_1 \cdot \ln \widehat{N} + b_2 \cdot \left(\ln \widehat{N}\right)^2 + b_3 \cdot \left(\ln \widehat{N}\right)^3 + b_4 \cdot (\ln \hat{\tau}) + b_5 \cdot (\ln \hat{\tau})^2 + b_6 \cdot (\ln \hat{\tau})^3 + b_7 \cdot \ln \hat{\tau} \cdot \ln \widehat{N} + b_8 \cdot (\ln \hat{\tau})^2 \cdot \ln \widehat{N} + b_9 \cdot \ln \hat{\tau} \cdot \left(\ln \widehat{N}\right)^2 + b_{10} \cdot (\ln \hat{\tau})^2 \cdot \left(\ln \widehat{N}\right)^2 \quad (3.95)$$

The constants in the above equation are presented in Table 3.6:

Table 3.6: Constants for the calculation of motor's efficiency

Coefficient	Value
$\boldsymbol{b_0}$	0.893747915
$\boldsymbol{b_1}$	0.0323048796
$\boldsymbol{b_2}$	-0.0191761519
$\boldsymbol{b_3}$	0.0152204756
$\boldsymbol{b_4}$	0.00732867448
$\boldsymbol{b_5}$	-0.031706182
$\boldsymbol{b_6}$	0.021641508
$\boldsymbol{b_7}$	0.0163125253
$\boldsymbol{b_8}$	0.00437556935
$\boldsymbol{b_9}$	-0.0411952262
$\boldsymbol{b_{10}}$	-0.0162681324

Furthermore, for the inverter, the corresponding expression gives [108]:

$$\eta_{invert} = a_o + a_1 \cdot \ln \widehat{N} + a_2 \cdot \left(\ln \widehat{N}\right)^2 + a_3 \cdot \left(\ln \widehat{N}\right)^3 + a_4 \cdot \left(\ln \hat{P}\right) + a_5 \cdot \left(\ln \hat{P}\right)^2 + a_6 \cdot \left(\ln \hat{P}\right)^3 \quad (3.96)$$

The constants in the above equation are presented in Table 3.7:

Table 3.7: Constants for the calculation of inverter's efficiency

Coefficient	Value
a_0	0.955726922
a_1	0.0260983262
a_2	0.0242349302
a_3	0.0121191602
a_4	0.0494828374
a_5	0.0334143316
a_6	0.022744636

Hence, the absorbed electric power is computed from the mechanical power divided by the above calculated efficiencies:

$$P_{el,pump} = \frac{W_{mech,pump}}{\eta_{motor} \cdot \eta_{invert}} \quad (3.97)$$

3.4. Expander

3.4.1 Expander type selection

The expander is the last major cycle's component that needs to be analyzed. It is placed after the evaporator and expands the high temperature and pressure exiting stream, producing in that way mechanical work that consequently drives a generator and gives electric power. Since it is responsible for power production it is closely linked to the overall yielded efficiency of the cycle

The most common alternatives for small-scale ORC systems are positive displacement (volumetric) machines, which decrease the fluid's pressure by increasing its volume. The expansion process is imposed either with the use of valves or by the machine's own geometry, as shown below in Figure 3.10, which depicts the main classification of volumetric expanders [110]. They are more appropriate for these applications because they can handle lower mass flow rates with relatively high expansion ratios [111]. From the categories presented the most suitable for power outputs lower than 50 kW, are piston, scroll and screw expanders, which are going to be evaluated below.

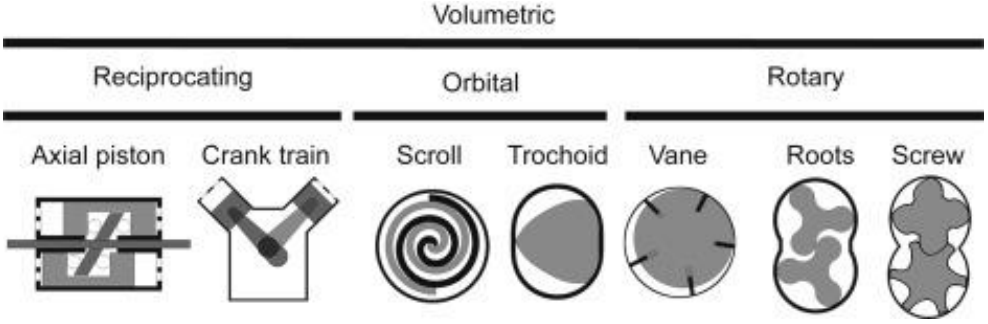

Figure 3.10: Classification of positive displacement expanders [110]

One of the most usually selected alternatives for small scale ORC systems is the scroll expander. In most cases it is a scroll compressor used in reverse operation and similar to all positive displacement machines, it has a fixed volumetric ratio. However, the main difference with the aforementioned categories is its complicated geometry [11]. It consists of two spirals, one being the central symmetry of the other. One of the spirals is fixed, whereas the other follows an orbital movement forming successively in that way the suction, expansion and discharge chambers [110].

The final selection of the expander that is going to be studied and integrated in the system depends basically on the power output and its thermodynamic performance. Lemort and Legros [112] have compared and evaluated the working range of the basic commercial models of the above types of expanders, which are shown in Figure 3.11. Scroll expanders show the best performance in a range that is limited to 10 kW, whereas for screw the working range is limited downward, starting from 2 kW. For the designed system the estimated power output lies around 6 kW, which does not insert any limitations based on the above power data.

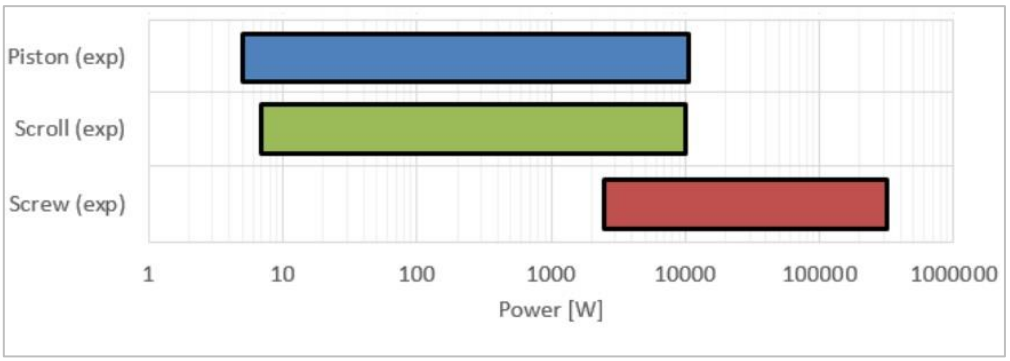

Figure 3.11: Working power range for piston, scroll and screw expanders [112, 113]

Regarding their isentropic efficiency, there are commercial models of each of the two categories that can perform equally effectively, in the whole range of their power output, with a maximum yielded efficiency of around 80% [114, 115]. Moreover, in most of the examined experimental rigs, the used volumetric ratio is quite similar for the two types of machines (around 5), although the maximum value is slightly higher in case of the screw one, which may lead to lower condensing pressure augmenting the cycle's efficiency [116].

A major limitation for the case of scroll expanders is the maximum temperature at its inlet. The approximate maximum is around 215 ^{o}C, which is close to the maximum developed temperature as calculated in the solar loop [117]. Because of that, screw expanders are selected and modeled as the most appropriate for the designed configuration, which enhances the flexibility of the system, since it allows a further extension of the study in case of higher collectors' surface and hence increased power output.

3.4.2 Screw expander modelling

The developed model is based on the experimental study held by Hsu et al. [118] and investigates the performance of a screw expander coupled with an ORC system for various working conditions. The pressure ratio takes values in a working interval that varies between 2.4 and 6.1, whereas the rotational speed is around 3600 rpm, which will be used as a nominal value in the expander's analysis.

The function that describes the expander's operation uses as inputs the thermodynamic properties of the working medium, along with its mass flow rate and the pressure of the exiting stream, which is already defined since it is equal to the low pressure of the cycle, in which takes place the condensation (p_{cond}).

From the experimental study and the graphs that refer to the isentropic efficiency of the expander can be estimated a polynomial function that fits the above obtained data. From 8 selected points is computed a polynomial fitting of 5th degree which is demonstrated below in Figure 3.12 as well as the corresponding function (equation (3.98)) from which can be calculated the efficiency of a screw expander given its pressure ratio (r_p).

$$\eta_{exp}^{is} = 0.001082 \cdot r_p^5 - 0.027767 \cdot r_p^4 + 0.2871 \cdot r_p^3 - 1.51052 \cdot r_p^2 + 4.06965 \cdot r_p - 3.78 \quad (3.98)$$

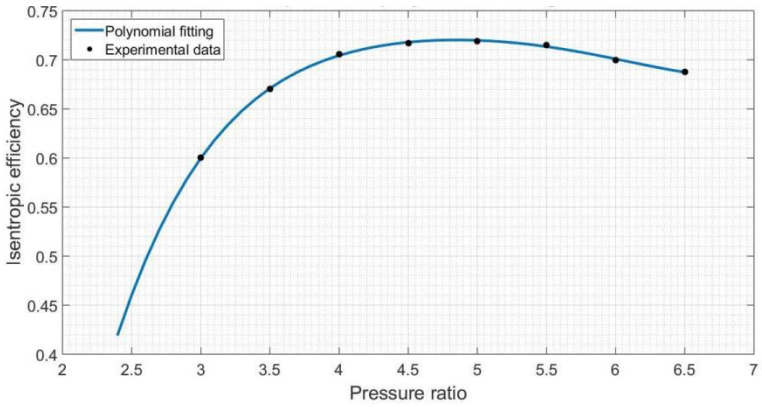

Figure 3.12: Expander's fitting on pressure ratio-isentropic efficiency graph

From the estimated expression and since are known the pressure values both at the input and output of the expander, it can be calculated the pressure ration and the isentropic efficiency:

$$r_p = \frac{p_{in}}{p_{out}} = \frac{p_{evap}}{p_{cond}} \quad (3.99)$$

As for the isentropic efficiency, in case of the expander it is equal to:

$$\eta_{is,exp} = \frac{h_{exp}^{in} - h_{exp}^{out}}{h_{exp}^{in} - h_{is,exp}^{out}} \quad (3.100)$$

From equation 3.101 derives the exiting enthalpy and from that all the other values of the fluid at the exiting state:

$$h_{exp}^{out} = h_{exp}^{in} - \eta_{is,exp} \cdot (h_{exp}^{in} - h_{is,exp}^{out}) \quad (3.101)$$

Assuming that the energy losses in the expander are negligible, the enthalpy raise of the working fluid is equal to the produced mechanical work, which is then transferred to the generator for the electric power production. Hence, the mechanical work derives from the following equation:

$$W_{mech,exp} = \dot{m}\left(h_{exp}^{in} - h_{exp}^{out}\right) \quad (3.102)$$

Apart from the thermal properties of the working fluid, is needed the volumetric displacement of the expander. Ideally it derives from the following equation:

$$V_s = \frac{60 \cdot \dot{m}}{N_{exp} \cdot \rho_{exp}^{in}} \quad (3.103)$$

Nevertheless, due to leakages between the two screws and the casing, the real value of the mass flow rate can be estimated by introducing the filling factor (ff). With the introduction of this parameter, equation (3.103) becomes:

$$V_s = \frac{60 \cdot \dot{m}}{N_{exp} \cdot \rho_{exp}^{in} \cdot ff} \quad (3.104)$$

In order to determine its value are used the experimental data presented in the analysis of Dumont et al. [114]. Based on this study, the data for the filling factor of screw expanders are fitted as shown in Figure 3.13, using a polynomial of 7th degree.

With the variables in equation (3.104) defined and the rotational speed in rpm, the volumetric displacement of the expander can finally be calculated.

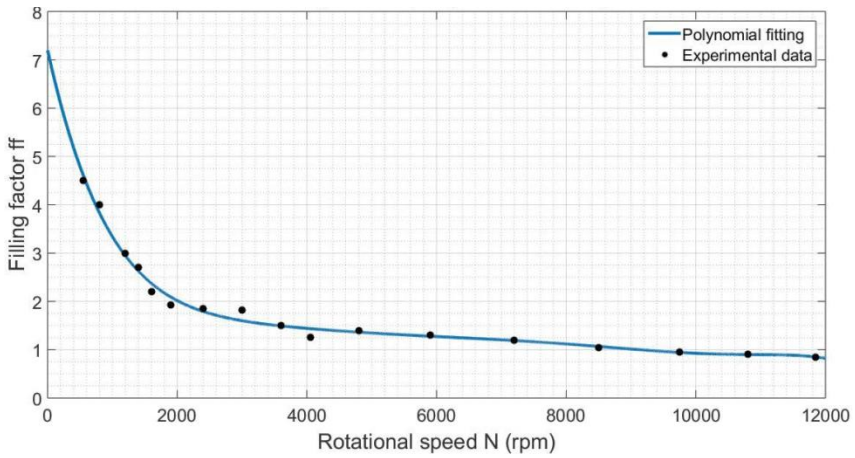

Figure 3.13: Expander's fitting on rotational speed-filling factor graph

As it has already been described in the case of the pump, there are some losses associated with the connection of the machines with the electric grid and the corresponding energy transfer. As a result, the produced energy is slightly lower than the calculated mechanical work and it derives by multiplying the work with the efficiencies of the inverter and the generator.

The function of the inverter is exactly the same as presented in the previous paragraph for the pump. As for the generator, is assumed that it functions in the same way as the motor but in reverse operation and therefore the same correlations as before can be applied.

Finally, the total energy output to the grid is equal to:

$$P_{el,exp} = W_{mech,exp} \cdot \eta_{gen} \cdot \eta_{invert} \quad (3.105)$$

3.5. Thermodynamic cycle modelling

3.5.1 Dry fluids

Based on the analysis of each of the components that has been presented above and the corresponding models, the developed functions are combined, in order to compose an overall function that describes the function of the ORC. The goal is to calculate the thermodynamic values in every state of the cycle and to perform the sizing of its components.

In order to execute the necessary calculations, there are some variables that characterize the cycle and need to be selected and externally assigned as operational parameters.

These variables are also presented in the table below, along with their abbreviations that are going to be used later in the description of the analysis.

Table 3.8: Working parameters for cycle modelling

Parameter	
Working fluid	f
Evaporator's absorbed power	Q_{evap}
Evaporator's superheating	ΔT_{sup}
Condenser's subcooling	ΔT_{sub}
HTF inlet temperature	T_{hi}
HTF inlet pressure	p_{hi}
HTF mass flow rate	$\dot{m}_h$
Cooling water inlet temperature	T_{ci}
Cooling water inlet temperature	p_{ci}
Cooling water mass flow rate	$\dot{m}_c$

With the above parameters defined in order to initiate the calculating procedure a value for the fluid's mass flow rate ($\dot{m}_f$) needs to be supposed. Subsequently, is determined the pressure and temperature of the evaporator and the condenser, which set the high and low limits for the cycle's working range. These calculations are carried out based on the inlet temperature of the secondary streams in both heat exchangers and on the corresponding pinch point that has been selected.

At first regarding the evaporator, a pinch point of 5 K is chosen, which is the minimum feasible temperature difference in heat exchange. It is obvious that as the pinch point increases, the cycle's maximum temperature and pressure decrease and there is an amount of the source's thermal content that remains unexploited. Therefore, the total thermal efficiency diminishes, as depicted in the indicative Figure 3.14, in which the evaporator's pinch point varies between 5-30 K.

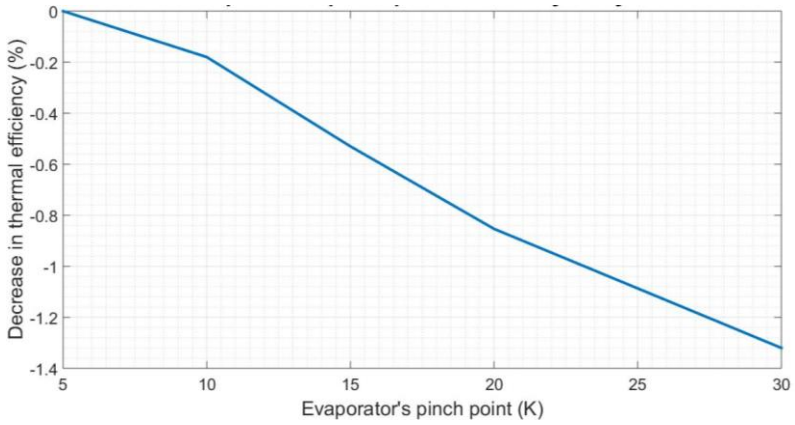

Figure 3.14: Reduction in cycle's thermal efficiency for increasing pinch point in the evaporator

As can be observed in Figure 3.5, the pinch point is located when the cold side is in state of saturated liquid. For the determination of the evaporation temperature is needed an iterative process:

Based on a guess for the value for the evaporation temperature (T_{evap}), is computed the corresponding evaporation pressure (p_{evap}). Taking into consideration the fluid's superheating and by using Coolprop it can be defined the enthalpy of the cold stream at its exit and at the point of saturated liquid and from that the transferred heat between these two states:

$$h_{c,1} = h(p = p_{evap}, T = T_{evap} + \Delta T_{sup}) \quad (3.106)$$

$$h_{c,2} = h(p = p_{evap}, x = 0) \quad (3.107)$$

$$H_c = \dot{m}_f \cdot (h_{c,1} - h_{c,2}) \quad (3.108)$$

For the hot stream is known the HTF inlet temperature (T_{hi}) and as already mentioned the pinch point is set at 5 K. Thus, for the above calculated transferred heat of the cold stream (H_c) the hot's fluid temperature is equal to 5 K higher than the evaporation temperature. Similar to the cold side and using the datasheet of the thermal fluid [45] are determined both enthalpies at the corresponding points of the hot one and from that the derived transferred heat:

$$h_{h,1} = h(\, T = T_{hi}) \quad (3.109)$$

$$h_{h,2} = h(T = T_{evap} + 5) \quad (3.110)$$

$$H_h = \dot{m}_h \cdot (h_{h,1} - h_{h,2}) \quad (3.111)$$

As stated previously, the above calculations are carried out for an assumed value of the evaporation temperature and hence the power given from equations (3.108), (3.111) are not equal. The iterative procedure continues for T_{evap} that varies between $(T_{hi} - 20 - \Delta T_{sup})$ and $(T_{hi} - 5 - \Delta T_{sup})$. Within this range is chosen the evaporation temperature that generated a minimum difference between H_c and H_h.

Concerning the condenser, the same process needs to be undertaken, so as to define the condensing temperature (T_{cond}) and the corresponding pressure (p_{cond}). For the condenser since the working temperature range is relatively low compared to the evaporator, is selected a pinch point equal to 10 K, which is the minimum allowable temperature difference that ensures an efficient heat transfer.

For the definition of the condensing conditions it needs to be taken into consideration the limitations inserted by the expansion machines. It was decided to insert at maximum two expanders whose maximum pressure ratio is equal to 6.1, as it has already been mentioned in the description of the expander's model. Assuming equal ratio in both expanders with its maximum value, in order to achieve the maximization of the thermal efficiency, and with the evaporation pressure already known it is considered:

$$p_{cond} = \frac{p_{evap}}{6.1^2} \quad (3.112)$$

With the major boundaries of the cycle already defined the next step includes the calculation and the sizing of its components based on the previously developed modelling functions:

I. Evaporator

The required inputs as mentioned are the thermodynamic properties (temperature and pressure) both at the inlet and outlet of the cold stream, the working fluid, the properties of the inlet of the hot stream and both mass flow rates. These variables are presented in Table 3.9:

Table 3.9: Inputs for the evaporator's function

Evaporator's input variables	
Working fluid	f
Fluid's inlet temperature	T_{evap}^{in}
Fluid's inlet pressure	p_{evap}
Fluid's outlet temperature	T_{evap}^{out}
Fluid's outlet pressure	p_{evap}
Fluid's mass flow rate	$\dot{m}_f$
HTF inlet temperature	T_{hi}
HTF inlet pressure	p_{hi}
HTF mass flow rate	$\dot{m}_h$

From these parameters those that remain undefined are the fluid's inlet and outlet temperature.

At this point are known all the necessary inputs and the evaporator's function can be applied. From this, derive the most suitable heat exchanger model along with the required number of plates, the exchange surface, the pressure drop of both streams and the final pinch point, all of which are shown in the table below:

Table 3.10: Outputs of the evaporator's function

Evaporator's output variables	
Heat exchanger model	k_{evap}
Required number of plates	N_{evap}
Required exchange surface	A_{evap}
Fluid's pressure drop	Δp_{evap}^{f}
HTF pressure drop	Δp_{evap}^{HTF}
Evaporator's pinch point	pp_{evap}

II. Expander

The component that follows the evaporator is the expander. Its function needs as inputs the thermodynamic properties (temperature and pressure) at the inlet, the working fluid, the mass flow rate and the outlet pressure. These are tabulated below:

Table 3.11: Inputs for the expander's function

Expander's input variables	
Working fluid	f
Fluid's inlet temperature	T_{exp}^{in}
Fluid's inlet pressure	p_{exp}^{in}
Fluid's outlet pressure	p_{exp}^{out}
Fluid's mass flow rate	$\dot{m}_f$

Since there are two consecutive expanders installed in the system, the function is applied twice. For the first one:

$$T_{exp,1}^{in} = T_{evap}^{out} \quad (3.113)$$

$$p_{exp,1}^{in} = p_{evap} - \Delta p_{evap}^{f} \quad (3.114)$$

with Δp_{evap}^{f} being the pressure losses due to the evaporator.

Finally, since the two expanders work on the same pressure ratio, the exiting pressure can be easily calculated:

$$p_{exp,1}^{out} = p_{mean} = \sqrt{p_{exp,1}^{in} \cdot p_{cond}} \quad (3.115)$$

With all the inputs specified, is used the expander's function, from which derive its characteristics (isentropic efficiency, rotational speed, volumetric displacement), the properties of the working fluid at the outlet, the mechanical work and the corresponding generator's produced power.

Subsequently, is reapplied the function in case of the second expander and the outputs are the same as previously, but this time for the second expander, all of which are demonstrated in the following table:

Table 3.12: Outputs of the expander's function

Expander's output variables		
	Expander 1	**Expander 2**
Isentropic efficiency	$\eta_{is,exp,1}$	$\eta_{is,exp,2}$
Rotational speed	$N_{rot,exp,1}$	$N_{rot,exp,2}$
Volumetric displacement	Vs_1	Vs_2
Fluid's outlet temperature	$T_{exp,1}^{out}$	$T_{exp,2}^{out}$
Fluid's outlet pressure	$p_{exp,1}^{out}$	$p_{exp,2}^{out}$
Mechanical work	$W_{mech,exp,1}$	$W_{mech,exp,2}$
Electric power	$Pel_{gen,1}$	$Pel_{gen,2}$

III. Condenser

Thereafter is examined the condenser's operation. The necessary inputs are similar to the evaporator's and are summarized below.

Table 3.13: Inputs for the condenser's function

Condenser's input variables	
Working fluid	f
Fluid's inlet temperature	T_{cond}^{in}
Fluid's inlet pressure	p_{cond}
Fluid's outlet temperature	T_{cond}^{out}
Fluid's outlet pressure	p_{cond}
Fluid's mass flow rate	$\dot{m}_f$
Cooling water inlet temperature	T_{ci}
Cooling water inlet temperature	p_{ci}
Cooling water mass flow rate	$\dot{m}_c$

With assigned values for the working fluid, its inlet pressure and mass flow rate, as well as for all the required characteristics of the cooling water and since the pressure inside the heat exchanger is considered constant, the only variables that need to be defined are the temperatures of the organic fluid as it enters and exits the condenser.

By implementing the appropriate function, derive as outputs the applicable heat exchanger model, the required number of plates, the exchange surface, the condenser's heat duty, the pressure drop of both streams and the final pinch point, all of which are shown in the table below:

Table 3.14: Outputs of the condenser's function

Condenser's output variables	
Heat exchanger model	k_{cond}
Required number of plates	N_{cond}
Required exchange surface	A_{cond}
Condenser's heat duty	Q_{cond}
Fluid's pressure drop	Δp_{cond}^{f}
Cooling water pressure drop	Δp_{cond}^{water}
Condenser's pinch point	pp_{cond}

IV. Pump

Exiting the condenser, the organic medium flows into the pump in which takes place the pressure elevation. Its modelling requires the inlet temperature and pressure, the working fluid, the mass flow rate and the outlet pressure. These are cited below:

Table 3.15: Inputs for the pump's function

Pump's input variables	
Working fluid	f
Fluid's inlet temperature	T_{pump}^{in}
Fluid's inlet pressure	p_{pump}^{in}
Fluid's outlet pressure	p_{pump}^{out}
Fluid's mass flow rate	$\dot{m}_f$

By applying the pump's function and its operational features are obtained (isentropic efficiency, rotational speed), along with the properties of the working fluid at the outlet, the mechanical work and the corresponding power absorbed by the motor, which are presented in the following table:

Table 3.16: Outputs of the pump's function

Pump's output variables	
Isentropic efficiency	$\eta_{is,pump}$
Rotational speed	$N_{rot,pump}$
Fluid's outlet temperature	T_{pump}^{out}
Fluid's outlet pressure	p_{pump}^{out}
Mechanical work	$W_{mech,pump}$
Electric power	Pel_{motor}

V. Recuperator

In Figure 3.15 is depicted an indicative curve of a simple cycle as already described without a recuperator. As the expansion ends at a state higher than the condensing one, then the exploitable heat increases and the use of a recuperator is more profitable.

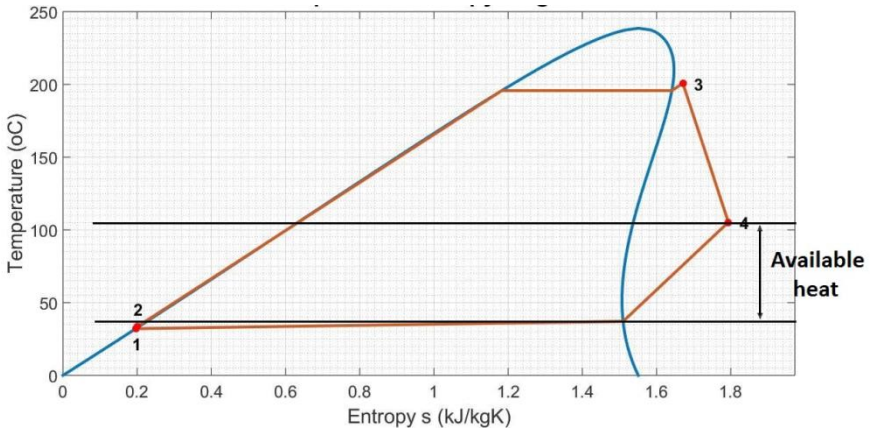

Figure 3.15: Heat availability for recuperator addition

In case this difference is greater than 20 K it was considered to be beneficial to insert this additional component to the system.

The inputs needed for the recuperator's function are presented below:

Table 3.17: Inputs for the recuperator's function

Recuperator's input variables	
Working fluid	f
Hot stream inlet temperature	$T_{h,rec}^{in}$
Hot stream inlet pressure	$p_{h,rec}^{in}$
Cold stream inlet temperature	$T_{c,rec}^{in}$
Cold stream inlet pressure	$p_{c,rec}^{in}$
Hot stream outlet temperature	$T_{h,rec}^{out}$
Hot stream outlet pressure	$p_{h,rec}^{out}$
Mass flow rate	$\dot{m}_f$

The outputs of the recuperator's function include the heat exchanger model, the required number of plates, the exchange surface, the total heat transferred, the temperature of the exiting cold stream and the pressure drop of both streams, which are shown in the table below:

Table 3.18: Outputs of the recuperator's function

Recuperator's output variables	
Heat exchanger model	k_{rec}
Required number of plates	N_{rec}
Required exchange surface	A_{rec}
Transferred heat	Q_{rec}
Cold stream outlet temperature	$T_{c,rec}^{out}$
Hot stream pressure drop	$\Delta p_{h,rec}$
Cold stream pressure drop	$\Delta p_{c,rec}$

With the recuperator the cycle calculations are completed and every state in it is fully specified.

As it was stated in the beginning of the cycle's modelling, in order to initiate the procedure, a guess value for the working fluid's mass flow rate ($\dot{m}_f$) is introduced. Based on this value the cycle was solved and were calculated the enthalpies at the inlet of the evaporator (h_{evap}^{in}) and the outlet of the recuperator's cold side ($h_{c,rec}^{out}$), or the outlet of the pump if there is no recuperator addition. If the initial assumption for $\dot{m}_f$ is correct the two enthalpies would have the same value. Otherwise, there is a repetition of the process with a new mass flow rates, until convergence:

$$\left|h_{evap}^{in} - h_{c,rec}^{out}\right| < 20\,\frac{J}{kg \cdot K} \tag{3.116}$$

The whole procedure that was described is presented in a flow chart in the following figure:

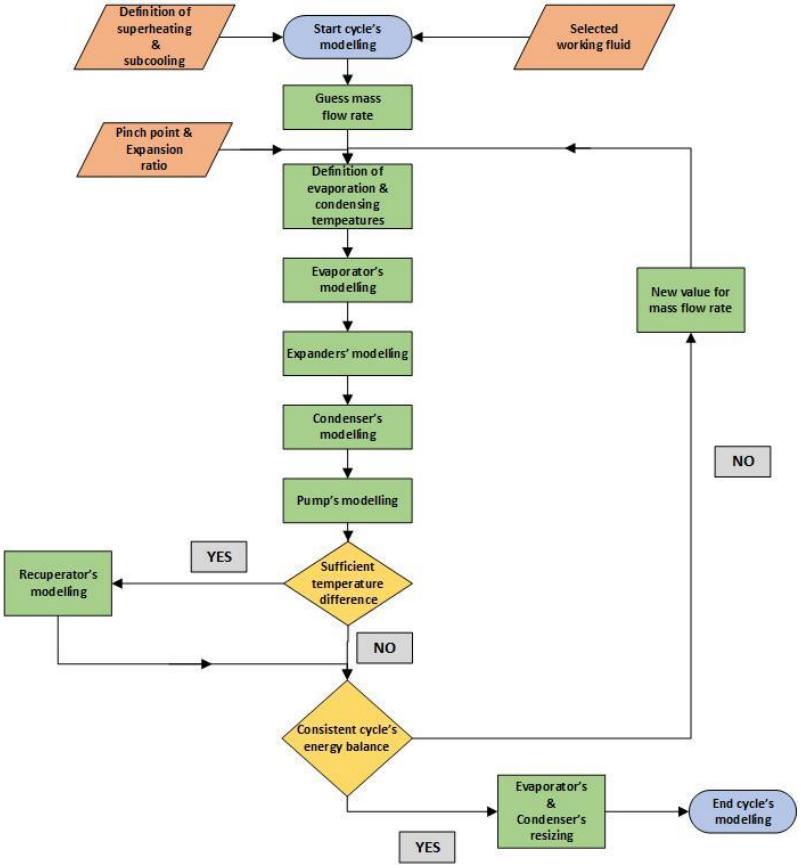

Figure 3.16: Flow chart of the ORC on-design modelling procedure

3.5.2 Wet fluids

The process described previously is applicable in case of dry fluids, in which the saturated gas line has a positive slope. On the contrary in case of a wet fluid, in which the slope is negative, there is a chance that the fluid enters the two-phase region after its expansion. Because of that the superheating in the evaporator cannot be determined in advance and imposed to the cycle, instead an estimation for the minimum value of superheating that leads to a single-phase flow after the expander has to be made, as shown in Figure 3.17:

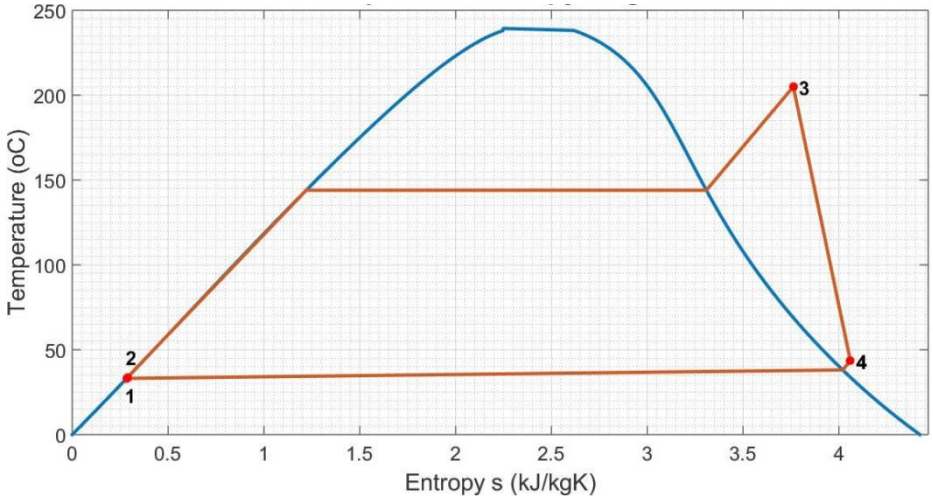

Figure 3.17: Indicative T-s diagram for an ORC system using wet organic fluid

3.6. Working fluid selection

As it has been mentioned in Chapter 1, the selection of the working fluid for an ORC is a crucial aspect of the system's design and relies on multiple factors that describe its performance, its thermodynamic characteristics as well as its chemical behavior.

In this study an initial screening of the fluids was performed based on the critical point and apply the cycle's model in order to identify which of them respond more efficiently to the available heat source and the selected configuration [116]. In most applications the maximum efficiency is attained with fluids whose critical temperature is close to the cycle's maximum temperature and slightly higher than that, in order to achieve maximum heat transfer from the heat source [119].

Since the maximum reached temperature on the solar loop is around 210 ^{o}C, for the pre-selection, only fluids with critical temperatures higher than this value were examined. Although, fluids with critical temperature higher than 300 ^{o}C will not be coupled effectively with the available heat level, for the sake of completeness some notable fluids with great commercial application that exceed this value were also assessed [41].

The list of the considered working fluids along with its critical properties and their type in terms of dry, wet or isentropic, are presented below [38]:

Table 3.19: Critical properties of selected organic fluids

Organic fluid	Critical temperature (^oC)	Critical pressure (bar)	Type
Isohexane	225	30.4	Dry
Acetone	235	47	Dry
Hexane	235	30.34	Dry
Cyclopentane	239	45.71	Dry
Methanol	240	82.16	Wet
Ethanol	242	62.68	Wet
Heptane	267	27.3	Dry
Cyclohexane	280	40.82	Dry
Benzene	289	48.9	Dry
MDM	291	14.1	Dry
Octane	296	25	Dry
Toluene	319	41.3	Dry
n-Nonane	321	22.7	Dry
p-Xylene	343	35.3	Dry
EthylBenzene	344	36.22	Dry
n-Decane	345	21.03	Dry

3.7. On-design operation

The final configuration of the system is depicted below in Figure 3.18, in which are incorporated both the recuperator as well as the second expander that were described previously.

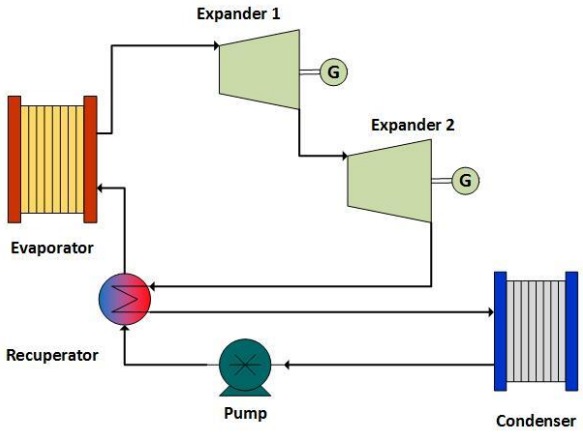

Figure 3.18: Final configuration of the studied ORC system

The heat source for the system is the solar circuit which receives and collects the solar irradiance as described before. Due to the stochasticity of the absorbed heat in an annual base, the feeding temperature varies as well. Therefore, an off-design model, based on the driving temperature, needs also to be developed for each hour of the year, which will be described in the following paragraph.

Regarding the working fluids, those listed in Table 3.19 were used. The power that absorbs the evaporator as heat duty is equal to 40 kW, the superheating and subcooling take a value equal to 5 K for dry fluids, which is also the minimum for the wet fluids' superheating. The hot fluid enters in state of 210 ^{o}C and 1.5 bar, whereas the cooling water 20 ^{o}C and 2 bar and their mass flow rates are 0.8 kg/s and 1 kg/s respectively.

All the assigned values are presented in the table below:

Table 3.20: Working parameters for on-design operation

On-design working parameters	
Working fluid	f
Evaporator's absorbed power	$Q_{evap} = 40\ kW$
Evaporator's superheating	$\Delta T_{sup} = 5\ K$
Condenser's subcooling	$\Delta T_{sub} = 5\ K$
HTF inlet temperature	$T_{hi} = 210\ ^{o}C$
HTF inlet pressure	$p_{hi} = 1.5\ bar$
HTF mass flow rate	$\dot{m}_h = 0.8\ \frac{kg}{s}$
Cooling water inlet temperature	$T_{ci} = 20\ ^{o}C$
Cooling water inlet pressure	$p_{ci} = 2\ bar$
Cooling water mass flow rate	$\dot{m}_c = 1\ \frac{kg}{s}$

For the 16 selected fluids the thermodynamic cycle is solved and the results deduced are presented in Table 3.21 below. The major indicator for the system's performance is the thermal efficiency which is computed using the equation below:

$$\eta_{th} = \frac{Pel_{gen,1} + Pel_{gen,2} - Pel_{motor}}{Q_{evap} - Q_{rec}} \quad (3.117)$$

with Pel_{gen} being the electric power produced by the generators, Pel_{motor} the power needed for the pump's function and $Q_{evap} - Q_{rec}$ the heat finally absorbed by the evaporator, which derives from the initially imposed Q_{evap} reduced by the heat duty of the recuperator.

Table 3.21: Cycle's results for the examined working fluids

Organic fluid	η_{th} (%)	$\eta_{is,pump}$ (%)	T_{evap} (ΔT_{sup}) (°C)	T_{cond} (°C)	P_{el} (kW)	Q_{rec} (kW)
Isohexane	17	69.55	198.16 (5)	42.23	5.16	11.67
Acetone	15.17	72.01	194.49 (5)	44.8	6.07	1.99
Hexane	16.78	67.17	196.94 (5)	45.65	5.14	11.1
Cyclopentane	17.24	71.82	195.71 (5)	37.09	6.17	6.28
Methanol	14.14	61.32	143.97 (61.03)	38.1	5.74	0
Ethanol	12.9	70.89	187.07 (17.93)	66.39	5.34	0
Heptane	16.02	56.52	195.71 (5)	56.46	4.7	11.78
Cyclohexane	17.02	61.85	194.18 (5)	47.44	5.52	8.71
Benzene	16.39	62.57	192.96 (5)	48.69	5.9	5.1
MDM	13.77	32.23	196.33 (5)	75.65	3.34	16.65
Octane	15.1	44.3	194.8 (5)	65.98	4.35	12.05
Toluene	15.71	49.86	192.35 (5)	58.63	5.37	6.58
n-Nonane	14.21	32.19	193.88 (5)	74.02	4.05	12.16
p-Xylene	14.88	36.74	191.73 (5)	67.37	4.92	7.53
EthylBenzene	14.96	37.89	192.04 (5)	66.87	4.91	7.81
n-Decane	13.35	22.04	193.27 (5)	81.31	3.8	12.12

The fluids are sorted in descending order based on their thermal efficiency and the results are shown in Figure 3.19, their pump's isentropic efficiency is depicted in Figure 3.20:

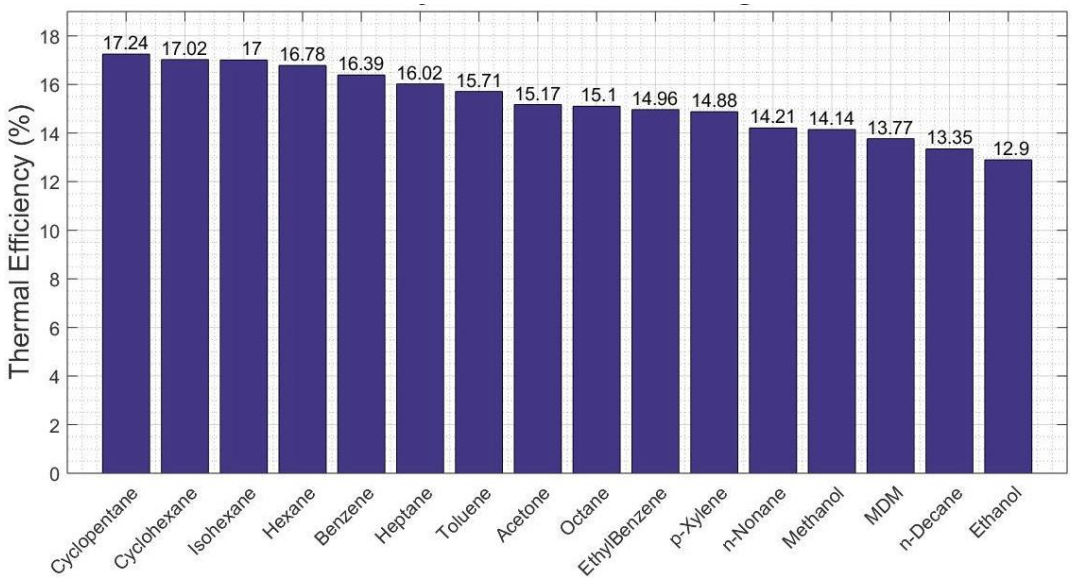

Figure 3.19: Thermal efficiency of the examined working fluids

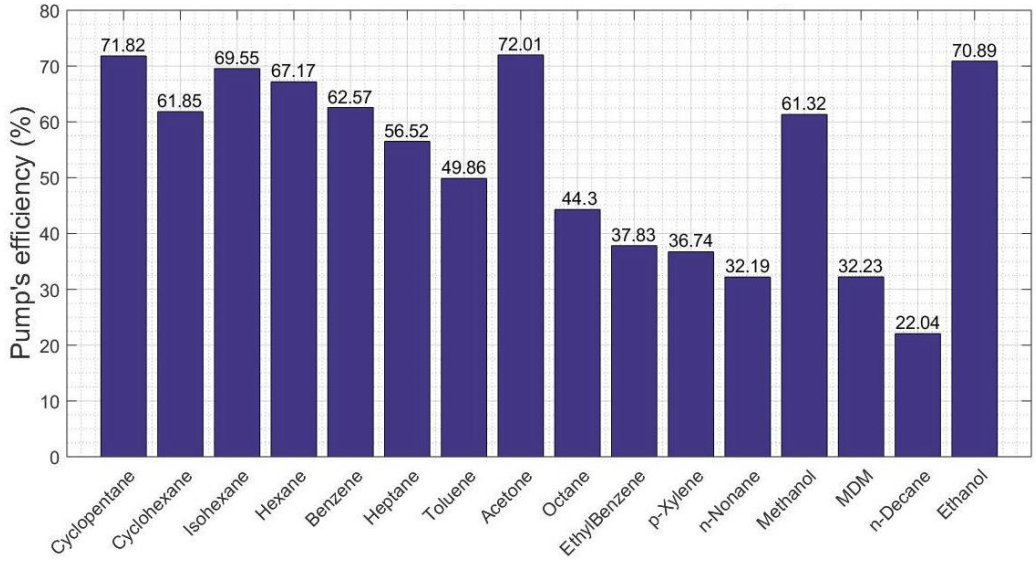

Figure 3.20: Pump's efficiency for the examined working fluids

Finally, in Figure 3.21-Figure 3.22 are illustrated their evaporation and condensation temperature. In case of the evaporation temperature, the bar's blue part corresponds to T_{evap}, whereas the yellow one to the superheating (ΔT_{sup}) while the labelled value is equal to T_{evap}.

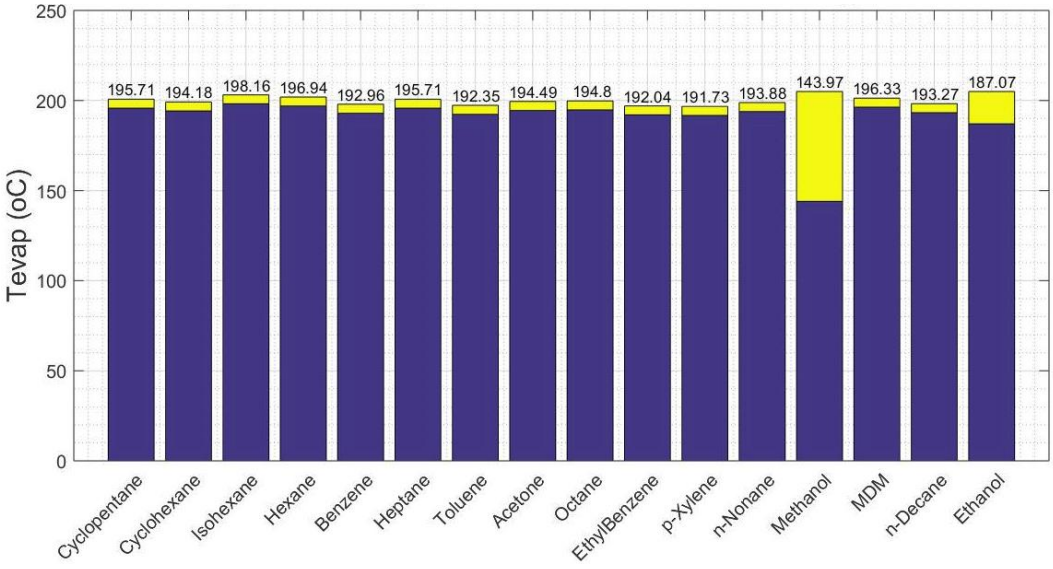

Figure 3.21: Evaporation temperature and superheating for the examined working fluids

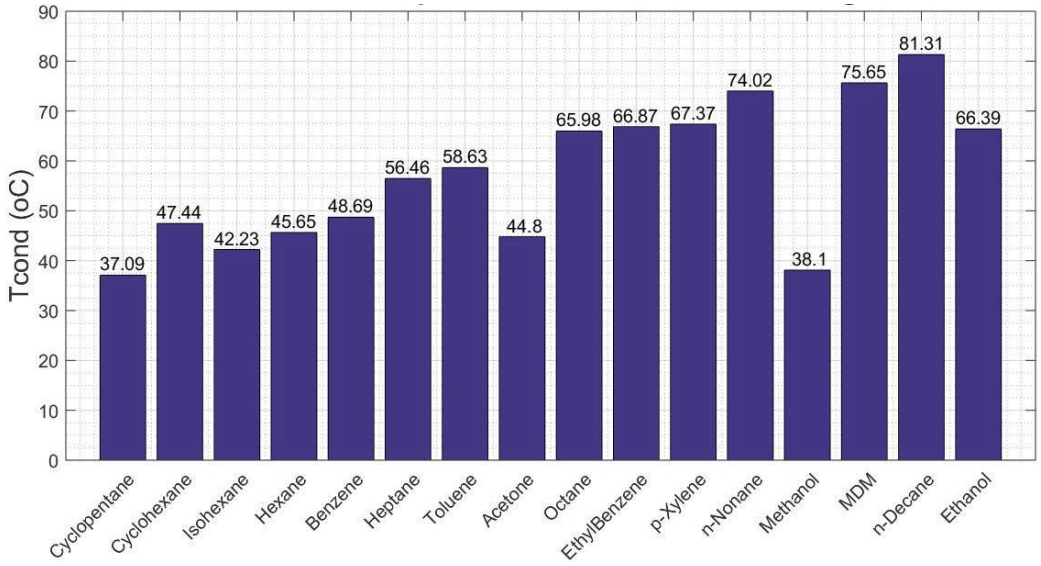

Figure 3.22: Condensation temperature for the examined working fluids

As observed in Figure 3.21, the maximum cycle's temperature is more or less of the same value for all the working fluids. However, in case of Methanol and Ethanol which the wet fluids, the superheating is much higher than 5 K, which leads to a decreased value of T_{evap} and thus reduces their efficiency as well.

As far as the expanders' function is concerned, a constant pressure ratio was considered. Due to that and according to equation (3.98), there are no fluctuations in the value of its isentropic efficiency which remains equal to:

$$\eta_{is,exp,1} = \eta_{is,exp,2} = 69.8\ \% \tag{3.118}$$

It is obvious that, as the expander's efficiency increases, a corresponding increase in the cycle's efficiency occurs. As shown in Figure 3.12, the studied expander has a maximum isentropic efficiency equal to around 72%, for expansion ratio equal to around 4.8. However, in this case in order to achieve the maximum isentropic efficiency a drop in the expansion ratio should be realized which affects negatively the overall thermal efficiency.

Because of that trade-off, a sensitivity analysis was conducted using cyclopentane as a reference fluid. As shown in the figure below, although the isentropic efficiency is reduced, the increase in the pressure limits elevates the total cycle's efficiency. It is therefore, profitable to select the maximum allowable value for the expansion ratio as already mentioned.

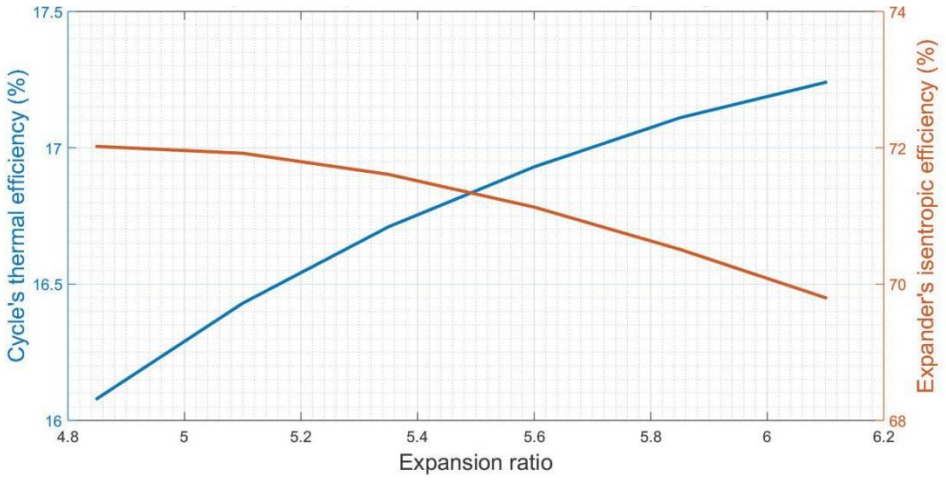

Figure 3.23: Variation of expander's efficiency and thermal efficiency with the expansion ratio

The selection of the working fluids for further investigation and an additional thermo-economic evaluation is based on their thermal efficiency. Hence, from the listed alternatives five fluids with the highest efficiency were selected. Additional to that Toluene was included, because it is highly applicable in ORC systems and has an extensive commercial use.

Thus, for the rest of the study only with these 6 organic fluids will be used:

- Cyclopentane
- Cyclohexane
- Isohexane
- Hexane
- Benzene
- Toluene

The on-design nominal characteristics of these six fluids are presented in the following tables for each one of them individually. These include the type of the heat exchangers (evaporator, condenser, recuperator) as well as the required number of plates. Additionally, are presented the pump's and expanders' characteristics (i.e. their isentropic efficiency, rotational speed and

electric power absorbed and produced respectively). Finally, are demonstrated the cycle's overall properties namely the evaporation and condensation temperatures, the thermal efficiency and the fluid's mass flow rate.

For the generator's total produced power, the sum of the power of each of the two expanders was determined:

$$P_{el,gen} = P_{el,gen,1} + P_{el,gen,2} \quad (3.119)$$

Table 3.22: On-design characteristics for Cyclopentane

Evaporator model	AC30EQ
Evaporator number of plates N_{evap}	83
Condenser model	CB30
Condenser number of plates N_{cond}	52
Recuperator model	CB20
Recuperator number of plates N_{rec}	30
Pump's isentropic efficiency $\eta_{is,pump}$ (%)	71.82
Pump's rotational speed $N_{rot,pump}$ (rpm)	79
Motor's consumed power $P_{el,motor}$ (kW)	0.3513
Expander's isentropic efficiency $\eta_{is,exp}$ (%)	69.8
Expander's rotational speed $N_{rot,exp}$ (rpm)	3600
Generator's produced power $P_{el,gen}$ (kW)	6.17
Evaporation temperature T_{evap} (^oC)	195.71
Condensation temperature T_{cond} (^oC)	37.09
Mass flow rate $\dot{m}_f$ $(\frac{kg}{s})$	0.0655
Thermal efficiency η_{th} (%)	17.24

Table 3.23: On-design characteristics for Cyclohexane

Evaporator model	AC30EQ
Evaporator number of plates N_{evap}	92
Condenser model	CB30
Condenser number of plates N_{cond}	25
Recuperator model	CB20
Recuperator number of plates N_{rec}	95
Pump's isentropic efficiency $\eta_{is,pump}$ (%)	61.85
Pump's rotational speed $N_{rot,pump}$ (rpm)	76
Motor's consumed power $P_{el,motor}$ (kW)	0.1913
Expander's isentropic efficiency $\eta_{is,exp}$ (%)	69.8
Expander's rotational speed $N_{rot,exp}$ (rpm)	3600
Generator's produced power $P_{el,gen}$ (kW)	5.52
Evaporation temperature T_{evap} (^oC)	194.18
Condensation temperature T_{cond} (^oC)	47.44
Mass flow rate $\dot{m}_f$ $(\frac{kg}{s})$	0.0642
Thermal efficiency η_{th} (%)	17.02

Table 3.24: On-design characteristics for Isohexane

Evaporator model	AC30EQ
Evaporator number of plates N_{evap}	75
Condenser model	CB30
Condenser number of plates N_{cond}	32
Recuperator model	CB30
Recuperator number of plates N_{rec}	134
Pump's isentropic efficiency $\eta_{is,pump}$ (%)	69.55
Pump's rotational speed $N_{rot,pump}$ (rpm)	90
Motor's consumed power $P_{el,motor}$ (kW)	0.3396
Expander's isentropic efficiency $\eta_{is,exp}$ (%)	69.8
Expander's rotational speed $N_{rot,exp}$ (rpm)	3600
Generator's produced power $P_{el,gen}$ (kW)	5.16
Evaporation temperature T_{evap} (^oC)	198.16
Condensation temperature T_{cond} (^oC)	42.23
Mass flow rate $\dot{m}_f$ $(\frac{kg}{s})$	0.0646
Thermal efficiency η_{th} (%)	17.00

Table 3.25: On-design characteristics for Hexane

Evaporator model	AC30EQ
Evaporator number of plates N_{evap}	72
Condenser model	CB30
Condenser number of plates N_{cond}	27
Recuperator model	CB20
Recuperator number of plates N_{rec}	100
Pump's isentropic efficiency $\eta_{is,pump}$ (%)	67.17
Pump's rotational speed $N_{rot,pump}$ (rpm)	88
Motor's consumed power $P_{el,motor}$ (kW)	0.2879
Expander's isentropic efficiency $\eta_{is,exp}$ (%)	69.8
Expander's rotational speed $N_{rot,exp}$ (rpm)	3600
Generator's produced power $P_{el,gen}$ (kW)	5.14
Evaporation temperature T_{evap} (^oC)	196.94
Condensation temperature T_{cond} (^oC)	45.65
Mass flow rate $\dot{m}_f$ $(\frac{kg}{s})$	0.0633
Thermal efficiency η_{th} (%)	16.78

Table 3.26: On-design characteristics for Benzene

Evaporator model	AC30EQ
Evaporator number of plates N_{evap}	98
Condenser model	CB30
Condenser number of plates N_{cond}	29
Recuperator model	CB20
Recuperator number of plates N_{rec}	21
Pump's isentropic efficiency $\eta_{is,pump}$ (%)	62.57
Pump's rotational speed $N_{rot,pump}$ (rpm)	69
Motor's consumed power $P_{el,motor}$ (kW)	0.1803
Expander's isentropic efficiency $\eta_{is,exp}$ (%)	69.8
Expander's rotational speed $N_{rot,exp}$ (rpm)	3600
Generator's produced power $P_{el,gen}$ (kW)	5.9
Evaporation temperature T_{evap} (^oC)	192.96
Condensation temperature T_{cond} (^oC)	48.69
Mass flow rate $\dot{m}_f$ $(\frac{kg}{s})$	0.066
Thermal efficiency η_{th} (%)	16.39

Table 3.27: On-design characteristics for Toluene

Evaporator model	AC30EQ
Evaporator number of plates N_{evap}	101
Condenser model	CB30
Condenser number of plates N_{cond}	25
Recuperator model	CB20
Recuperator number of plates N_{rec}	39
Pump's isentropic efficiency $\eta_{is,pump}$ (%)	49.86
Pump's rotational speed $N_{rot,pump}$ (rpm)	72
Motor's consumed power $P_{el,motor}$ (kW)	0.1208
Expander's isentropic efficiency $\eta_{is,exp}$ (%)	69.8
Expander's rotational speed $N_{rot,exp}$ (rpm)	3600
Generator's produced power $P_{el,gen}$ (kW)	5.37
Evaporation temperature T_{evap} (^oC)	192.35
Condensation temperature T_{cond} (^oC)	58.63
Mass flow rate $\dot{m}_f$ $(\frac{kg}{s})$	0.0676
Thermal efficiency η_{th} (%)	15.71

Finally, in the figure below are illustrated the temperature-entropy diagrams that describe the cycle that performs each of the organic fluids.

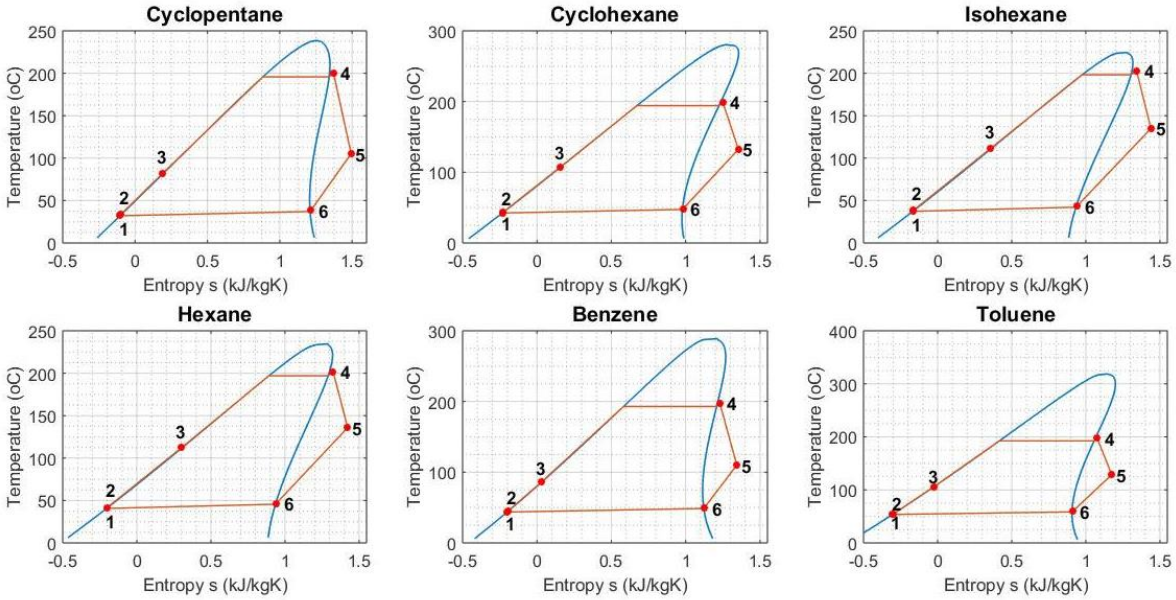

Figure 3.24: Temperature-entropy diagrams of the six selected organic fluids

3.8. Off-design operation

As it can be observed from the graphs of the previous chapter, the ORC's feeding temperature varies in an annual operation of the system. Thus, the HTF in the evaporator's hot side (T_{hi}) has variable inlet properties which affects the working conditions of the cycle and consequently its thermal performance. This temperature variation lies between 180 °C and 210 °C. The lower limit is the threshold temperature for HTF to flow into the ORC as declared in the previous chapter, whereas the upper one is the considered maximum value that was used for the on-design modelling.

For our analysis, an assumption was made that the fluctuation in the driving temperature affects the heat duty of the system, thus the power absorbed by the evaporator (Q_{evap}) which varies accordingly.

Therefore, $T_{hi}^{max} = 210\ ^oC$ corresponds to $Q_{evap}^{max} = 40\ kW$, whereas for $T_{hi}^{min} = 180\ ^oC$ it is supposed that the power is halved, $Q_{evap}^{min} = 20\ kW$. For the intermediate values there is a linear change for the heat duty:

$$Q_{evap} = Q_{evap}^{min} + \left(Q_{evap}^{max} - Q_{evap}^{min}\right) \cdot \frac{T_{hi} - T_{hi}^{min}}{T_{hi}^{max} - T_{hi}^{min}} \Rightarrow$$

$$Q_{evap} = 20 + 20 \cdot \frac{T_{hi} - 180}{30} \tag{3.120}$$

with T_{hi} the temperature of the HTF in ^{o}C and Q_{evap} the corresponding evaporator's heat duty in kW.

For each one of the six examined fluids the already calculated on-design results are used and remain steady throughout the rest of the study. These incude the models of the heat exchangers, the required number of plates as well as the nominal rotational speed and mechanical work for the expander and the pump.

Subsequently, for each value of T_{hi} scaling from its minimum up to the nominal, the evaporation temperature for a pinch point equal to 5 K is defined, in a way similar to the on-design strategy, described by equations (3.106-3.111). With a fixed inlet temperature of the cooling water equal to the on-design operation $T_{ci} = 20\ ^{o}C$ and the pinch point equal to 10K, fixed in fluid's state of saturated gas the condensation temperature (T_{cond}) and its pressure (p_{cond}) are set.

Based on these the pressure ratio (r_p) is computed. Depending on its value, three different cases can be distinguished, each one of which is characterized by a different approach in terms of the expanders' working rotational speed, aiming at a gradual incorporation of each component to the system:

1. For r_p lower than 6.1, one expander is used, with expansion ratio equal to r_p and rotational speed varying linearly from half of its nominal speed up to the nominal ($N_{rot,exp,1}^{nom}$), for T_{hi} between $180\ ^{o}C - 185\ ^{o}C$.
2. For r_p higher than 6.1 and up to 6.1^2, the second expander is introduced, with both of them operating with the same expansion ratio equal to $\sqrt{r_p}$. The first one works with its nominal speed ($N_{rot,exp,1}^{nom}$), whereas for the second varies between $\frac{N_{rot,exp,2}^{nom}}{2}$ and $N_{rot,exp,2}^{nom}$ for T_{hi} between $180\ ^{o}C - 195\ ^{o}C$.
3. For r_p higher than 6.1^2, the same strategy with the on-design is implemented, with both expanders working on their maximum allowable expansion ratio equal to 6.1 and with their nominal speeds. In that case the condensation temperature based on this maximum value has to be modified.

The cycle's computations are mainly the same as previously, starting with an initial guess for the mass flow rate and applying the components' functions successively, using their outputs as input variables for the following component. Concerning the heat exchangers, the inputs include the model and the number of plates and the received outputs are the streams' pressure drop. For the expanders and the pump, the nominal properties are used as input and the isentropic efficiency and the electric power produced or absorbed, respectively, are specified. The procedure ends when the mass flow rate takes a proper value that provides energy balance according to equation (3.116), as demonstrated in the figure below.

Contrary to the on-design estimations, the quantities calculated with equations (3.90-3.92) are not equal to one, but are determined based on the nominal point.

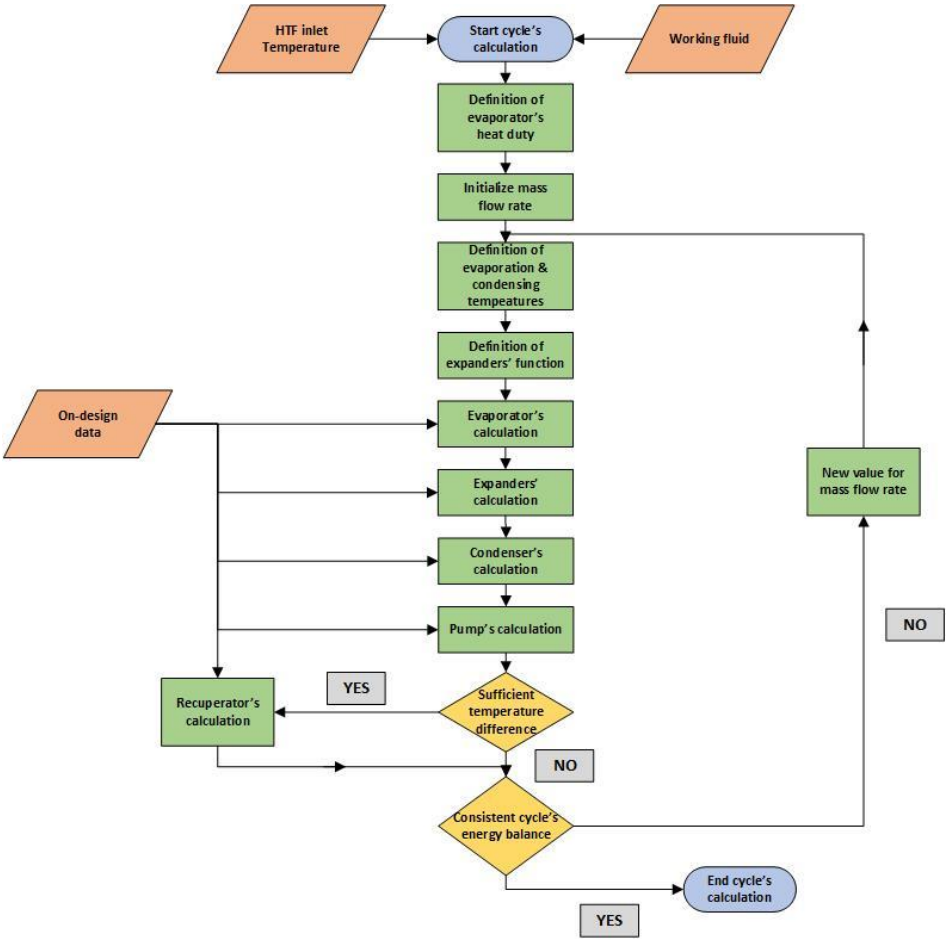

Figure 3.25: Flow chart of the ORC off-design modelling procedure

Indicatively, the results derived from this analysis regarding the cycle's thermal efficiency (η_{th}), are presented in the Figure 3.26 below, in which is depicted the variation of η_{th} for the six examined fluids with respect to the varying HTF temperature (T_{hi}).

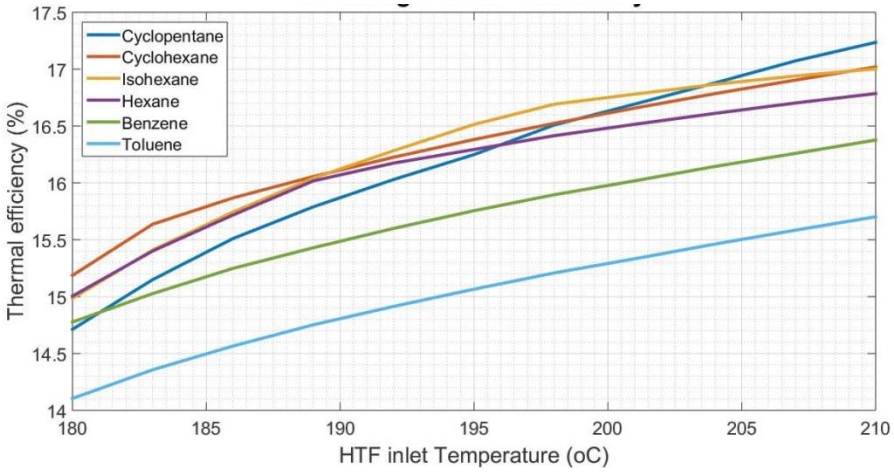

Figure 3.26: Variation of thermal efficiency with respect to HTF temperature in off-design operation

Chapter 4. Total system operation

As it has been described before, the total configuration consists of the solar and the ORC system which are coupled together. The solar loop functions as the source and provides heat to the ORC's evaporator, which subsequently is used for the power generation. The basic principle for the system's overall calculations is similar with the one presented for the solar circuit.

An hourly based fluctuation of the temperature and solar irradiance for an annual period of time is considered. As already explained, the irradiance's availability and the value of the sufficiency of the HTF temperature ($T_{threshold} = 180$ ℃), along with the total stored heat, produce four distinct cases. In each one of them the collectors and the ORC sub-systems are either opened and regularly functioning or closed, without altering the values of the previous time step. The main modification compared to the independent calculations of the collectors is in case of the functioning ORC system. In the previously developed initial model, the operation of the HTF loop considered a fixed value for the heat absorbed by the evaporator, and equal to $Q_{iorc} = 40\ kW$. However, at this point the cycle's thermodynamic data derive from the computations of the ORC's off-design operation.

The temperature of the HTF entering the evaporator is defined and is the ORC driving temperature. Therefore, for every fluid a polynomial fitting on the already calculated off-design results is introduced. A function in Matlab is developed that receives as inputs the examined working fluid and the evaporator's hot stream entering temperature (T_{hi}^{calc}). The function calls the results of the corresponding fluid and produces two polynomial functions of 5th degree that fit properly T_{hi} with respect to the evaporator's heat duty (Q_{evap}) and the cycle's thermal efficiency (η_{th}). The calculated T_{hi}^{calc} is the independent variable, which takes values between $180 - 210$ ℃, and thus derives the evaporator's heat and the efficiency for every hour of the year.

This procedure is repeated for each one of the six examined fluids, for the two types of collectors and the five selected cities. Thus, there are in total 60 cases that are going to be calculated. The described coupling process is demonstrated in the following flow chart as well.

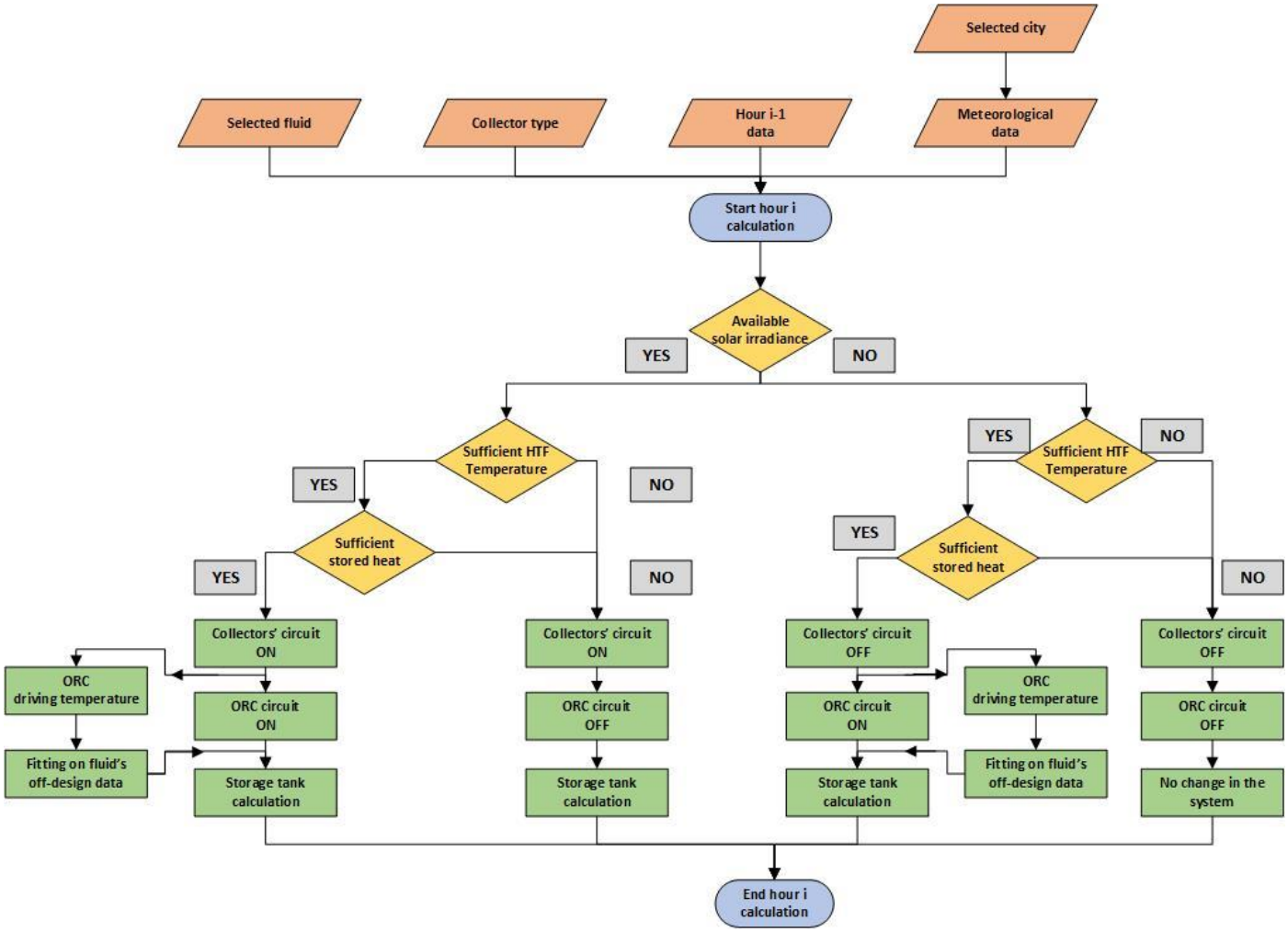

Figure 4.1: Flow chart of the collectors-ORC coupling procedure

The evaluation of the system's performance relies on two major parameters: its efficiency and its economic viability.

4.1. Efficiency analysis

In terms of thermodynamics, the most common expression used to describe the cycle's operation is the thermal efficiency. In our case it is calculated as already mentioned, by using the following equation:

$$\eta_{th} = \frac{Pel_{gen,1} + Pel_{gen,2} - Pel_{motor}}{Q_{evap}} = \frac{Pel_{net}}{Q_{evap}} \quad (4.1)$$

However, for the system's total energy efficiency the solar loop has to be attributed as well. Therefore:

$$\eta_{tot} = \frac{Pel_{net}}{Q_{sol}} \quad (4.2)$$

with $Q_{sol} = I_b \cdot A_{col}$ (4.3)

being the solar power at the collectors' surface.

In addition to that the exergy efficiency of the system is also calculated. Unlike the energy efficiency, the exergy one is an index that permits the comparison of power production systems that receive energy from different primary heat sources.

The exergy efficiency in this case, in which only electric power production takes place, derives from the following expression [120]:

$$\eta_{ex} = \frac{Pel_{net}}{Ex_{in}} \quad (4.4)$$

in which Ex_{in} is the total exergy used as input for the system. Since the heat source is the sun, this value is equal to the maximum solar exergy and can be determined with the following equation [121]:

$$Ex_{in} = Ex_{sol} = \left(1 - \frac{T_{amb}}{T_{sol}}\right) \cdot Q_{sol} \quad (4.5)$$

with T_{sol} being the apparent black body temperature of the sun and equal to 5770 K [122].

For each case, the calculations for every hour of the year are conducted from which, with the polynomial fitting, derive the thermal efficiency and the evaporator's heat. Using these values and equation (4.1), Pel_{net} is calculated in an hour basis and by summing them the total annual produced power (Pel_{net}^{annual}) is also specified. In a similar way, from the meteorological data for each location, the hourly based solar power and exergy production are calculated using equations (4.3), (4.5) and subsequently the corresponding annual values (Q_{sol}^{annual} and Ex_{sol}^{annual}).

Using the above annual results, from equations (4.2), (4.4) the two expressions for the system's efficiency can be determined.

4.2. Economic analysis

It is obvious that the appraisal of the designed system could not rely exclusively on thermodynamic parameters. The implementation of a power generation system is based also on its financial feasibility, which means whether the produced power is economically profitable compared to the other existing energy sources.

Because of that there is the need to incorporate in this study an assessment of the economic performance as well. At first, an estimation of the cost of each component and then an appropriate economic index to evaluate the results are implemented.

4.2.1 Components cost

The overall cost derives from the sum of the costs of the two sub-systems, the collectors and the ORC. All the values presented below are expressed in €:

I. Collectors' cost

Regarding the collectors' circuit, based on the equipment the following cost requirements are considered:

- Solar collectors: the cost for purchasing the solar panels. It varies depending on the type of collector and is expressed in $€/m^2$. For PTCs and PDCs the costs are displayed in the table below:

Table 4.1: Solar panels' cost

Type of collector	Cost
PTC [123]	$178\ €/m^2$
PDC [124, 125]	$235\ €/m^2$

Thus: $C_{sol}^{PTC} = 178 \cdot A_{col}$ and $C_{sol}^{PDC} = 235 \cdot A_{col}$ (4.6)

- Piping: includes the necessary pipes between the collectors as well as for the connection of the collectors' loop with the storage tank. It derives from the following equation [126]:

$$C_{pipe} = \left(0.89 + 0.21 \cdot D_{pipe}\right) \cdot L_{pipe} \quad (4.7)$$

with the pipes' diameter chosen equal to $D_{pipe} = 22.25\ mm$
and their length L_{pipe}, in m, chosen proportional to the collecting surface:

$$L_{pipe} \sim A_{col} \quad (4.8)$$

- Storage tank: its cost is computed based on a linear fitting on the costs of the commercially available tanks by OU Cerbos [127]. So, depending on its volume (V_{st} in m^3) the corresponding cost is:

$$C_{st,tank} = 231.87 + 312.97 \cdot V_{st} \quad (4.9)$$

- Heat transfer fluid: the cost of Therminol VP1 existing in both the storage tank as well as inside the collectors' and the HTF sub-circuits. The total volume of Therminol VP1 needed is assumed to be equal to the tank's volume plus 10 % of its volume that flows in the pipes. Based on that and for its market price derives:

$$C_{HTF} = 1.1 \cdot V_{st} \cdot 1000 \cdot 4.78 \quad (4.10)$$

Hence in total:

$$C_{col} = C_{sol} + C_{pipe} + C_{st,tank} + C_{HTF} \quad (4.11)$$

II. ORC cost

As for the ORC, the overall cost consists of numerous parts, since it includes various components. Thus:

- Hardware and control: cost of miscellaneous hardware and control mechanisms that ensure the proper function of the system. A fixed value is assigned [119]:

  $$C_{hard} = 800 \quad (4.12)$$

- Piping: corresponds to the necessary pipes for the connection of the components. It derives from the same equation as previously [126]:
  $$C_{pipe} = \left(0.89 + 0.21 \cdot D_{pipe}\right) \cdot L_{pipe} \quad (4.13)$$

  At this point though, two different cases depending on the phase of the fluid inside the pipes can be distinguished. For liquid fluids, a diameter equal to $D_{pipe} = 22.25\ mm$ was selected. However, for the part handling the working fluid in gas phase, the density is much lower and although the permissible velocity of the flow is higher, a greater pipe's cross-section is required. In that case the selection was $D_{pipe} = 44.45\ mm$. As for their length for both cases the same value was assumed, $L_{pipe} = 5\ m$.

- Feeding tank: for small-scale applications with low values of the fluid's mass flow rate, as in this study, a small feeding tank is necessary. In this case a tank with volume equal to $V_{feed} = 50\ l$ was considered.
  Its cost is computed based on a linear fitting on the costs of the data for the tanks provided by Zilmet [128], depending on its volume ($V_{feed}\ in\ l$):
  $$C_{feed,tank} = 150.46 + 4.48 \cdot V_{feed} \quad (4.14)$$

- Pump: the estimation of its cost relies on the nominal mechanical work of the pump ($W_{mech,pump}\ in\ W$) [126]:
  $$C_{pump} = 900 + \left(\frac{W_{mech,pump}}{300}\right)^{0.25} \quad (4.15)$$

- Expander: the cost correlation for the expander is expressed with respect to the volumetric displacement of the machine (V_s). Since there were two expanders in the on-design operation, the calculation of the corresponding cost for both of them was equal to:
  $$C_{exp} = 0.88 \cdot \left(3143.7 + 217423 \cdot V_{s,1}\right) + 0.88 \cdot \left(3143.7 + 217423 \cdot V_{s,2}\right) \quad (4.16)$$

- Generator and motor: their cost depends on the electric power that they produce or absorb respectively. Since the assumption was made that the generator and the motor are identical machines with reverse operation, the same expression is applied for both of them. With the power in kW the following applies [129]:

$$C_{gen} = 71.7 \cdot \left(P_{el,gen}\right)^{0.95}$$

$$C_{motor} = 71.7 \cdot \left(P_{el,motor}\right)^{0.95} \quad (4.17)$$

- Plate heat exchangers: their cost is proportional to their total surface and is calculated using the cost correlations below [119]:

$$C_{evap} = 190 + 310 \cdot A_{evap}$$
$$C_{cond} = 190 + 310 \cdot A_{cond}$$
$$C_{rec} = 190 + 310 \cdot A_{rec} \quad (4.18)$$

- Working fluid: similar to the HTF, the cost of the working fluid depends on the volume needed for the system's supply. The required amount of fluid is decided to be twice as much as the volume of the feeding tank. Thus, its cost is:

$$C_{fl} = 2 \cdot V_{feed} \cdot C_{fl}^{lt} \quad (4.19)$$

with C_{fl}^{lt} being the price of each fluid per liter ($€/l$). For the examined fluids the prices are shown in the table below:

Table 4.2: Cost of examined working fluids

Working fluid	Cost ($€/l$)
Cyclopentane	1.32
Cyclohexane	2.84
Isohexane	0.85
Hexane	0.82
Benzene	1.09
Toluene	0.92

Using the above equations and Table 3.22-Table 3.27 for all the required sizing data, the total cost of the ORC is equal to:

$$C_{ORC} = C_{hard} + C_{pipe} + C_{feed,tank} + C_{pump} + C_{exp} + C_{gen} + C_{motor} + C_{evap} + C_{cond} + C_{rec} + C_{fl} \quad (4.20)$$

Finally, in order to include the installation and equipment expenses, it is supposed that the overall cost is 20 % higher than the sum of the distinct costs. Hence:

$$C_{tot} = 1.2 \cdot (C_{sol} + C_{ORC}) \quad (4.21)$$

4.2.2 Economic indexes

In order to assess the viability of a system from a financial standpoint, the expenses needed for the energy production along with the profit generated from its exploitation have to be attributed.

In most cases, the initial investment and the installation expenses (Capital Expenditures-CAPEX) are not sufficient for the function of a working system, but additional operational and maintenance costs are required as well (Operating Expenses-OPEX). These additional expenses depend obviously on the project's lifetime, which therefore needs to be defined (n).

Furthermore, since both the income and the expenses are calculated in an annual period of time for as many years as the system's lifetime, it is crucial that a discount rate (i) is introduced. Because of the fact that the value of money alters as time passes, the discount rate is used in order to determine the present value of future cash flows.

Finally, as far as the income is concerned, an assumption that the energy generated is used for consumption by the producer was made. That means that is deducted from his overall energy consumption, reducing the energy that he receives from the grid. Hence, the income from the designed system can be calculated from the equation below:

$$INC = P_{el,net} \cdot C_{el} \quad (4.22)$$

with C_{el} being the cost of electricity which is highly dependent on the examined city, since each country has its own pricing policy.

There are several indexes that describe the economic performance of a system. The most commonly appearing ones are the Net Present Value (NPV), the Payback Period (PbP) and the Levelized Cost of Energy (LCoE).

Net Present Value is the sum of the present value of all the future inflows reduced by the present value of all the future outflows (operational costs and initial investment) and derives from the equation below. If its final value is positive, means that the investment will be financially profitable within its lifetime. On the contrary negative NPV represents a non-viable investing project.

$$NPV = -CAPEX + \sum_{t=1}^{t=n} \frac{(INC-OPEX)}{(1+i)^t} \quad (4.23)$$

With CAPEX and OPEX being the Capital and Operational Expenses as already mentioned and INC the income. Both OPEX and INC are calculated in an annual basis, whereas CAPEX is spent only at the time of the investment. The lifetime is equal to n, whereas i is the discount rate.

The Payback Period is defined as the lifetime in which a total NPV is equal to zero. In order for an investment to be profitable the computed PbP needs to be lower than the corresponding selected lifetime. Using equation (4.23) it is concluded:

$$NPV = -CAPEX + \sum_{t=1}^{t=PBP} \frac{(INC-OPEX)}{(1+i)^t} = 0 \Rightarrow PBP = -\frac{\ln\left(\frac{1-i\cdot CAPEX}{INC-OPEX}\right)}{\ln(1+i)} \quad (4.24)$$

Finally, the Levelized Cost of Energy calculates the cost of the produced energy within the system's lifetime. It is computed by dividing the production expenses, reduced in an annual period, by the corresponding annual energy and determines the cost of one electric kWh. The expression used is:

$$LCoE = \frac{\frac{CAPEX\cdot i}{1-(1+i)^{-n}}+OPEX}{P_{el,net}} \quad (4.25)$$

From the above performance indexes, it was selected to calculate LCoE, since it is the most commonly used and offers an independence in the economic evaluation of the system. Contrary to the other two, LCoE does not correspond only to this specific unit, but can be used for the comparison between energy production systems of various technologies [130].

Finally, in order to compare the designed configuration with others, additionally the cost per installed kW is calculated:

$$C_{kW} = \frac{CAPEX}{\max(power)} \quad (4.26)$$

4.3. Total system results

Based on the aforementioned methodology the desired values for all the examined cases were calculated, thus for two collector types, five cities and six organic fluids. At this point the whole layout has not been optimized yet in terms of the collectors' surface and the storage tank's volume. Therefore, the following results correspond to the preliminary design. The system's optimization is described in the following chapter along with the final results.

The parameters that need to be defined to perform these calculations are the collecting surface and the tank's volume as well as the assumptions regarding the economic assessment. For the first two the values assigned are the same as in chapter 2. Concerning the project's lifetime, is set equal to 25 years, the discount rate at 5 % and the annual operating expenses equal to 2 % of the initial investment. These values are also shown in the table below:

Table 4.3: Working parameters for preliminary total system calculations

Parameter	Value
Collectors' surface (A_{col})	50 m^2
Storage tank's volume (V_{st})	1.67 m^3
Investment's lifetime (n)	25 years
Discount rate (i)	5 %
OPEX	$0.02 \cdot CAPEX$

Furthermore, the price of electricity in each country is given by Eurostat for the second semesters of 2016-2018 and are shown below [131]. From the columns existing in the table the most recent values (2018) for household consumers were selected.

	Households (¹)			Non-households (²)		
	2016S2	2017S2	2018S2	2016S2	2017S2	2018S2
EU-28	0.2038	0.2042	0.2113	0.1129	0.1118	0.1149
Euro area	0.2179	0.2175	0.2242	0.1195	0.1184	0.1192
Belgium	0.2745	0.2877	0.2937	0.1158	0.1087	0.1142
Germany	0.2977	0.3048	0.3000	0.1492	0.1514	0.1516
Greece	0.1723	0.1620	0.1646	0.1115	0.1190	0.1059
Spain	0.2284	0.2177	0.2477	0.1029	0.1032	0.1098
Italy	0.2261	0.2080	0.2161	0.1556	0.1449	0.1434

eurostat

Figure 4.2: Electricity prices in the selected countries (€/kWh)

Since the examined cases are numerous, the discussion will focus on specific cases, which however are indicative of the system's function. For Athens with working fluid Cyclopentane and PTC as collectors, the thermal and economic results are presented in the following table:

Table 4.4: Preliminary results in case of Athens-Cyclopentane-PTC

Parameter	Value
Total efficiency	$7.72\ \%$
Exergy efficiency	$8.13\ \%$
LCoE	$0.6781\ €/kWh$
Cost per kW	$7.035 \cdot 10^3\ €/kW$
Total produced energy	$4.65\ MWh$
Total investment cost (CAPEX)	$34.68 \cdot 10^3\ €$

The distribution of the investment is better illustrated in the following figures. In the two pie charts below (Figure 4.3-Figure 4.4) is shown the percentage of the expenses for each one of the components of the two sub-systems, thus the collectors and the ORC. Moreover, the final chart in Figure 4.5 depicts the cost distribution in the whole unit.

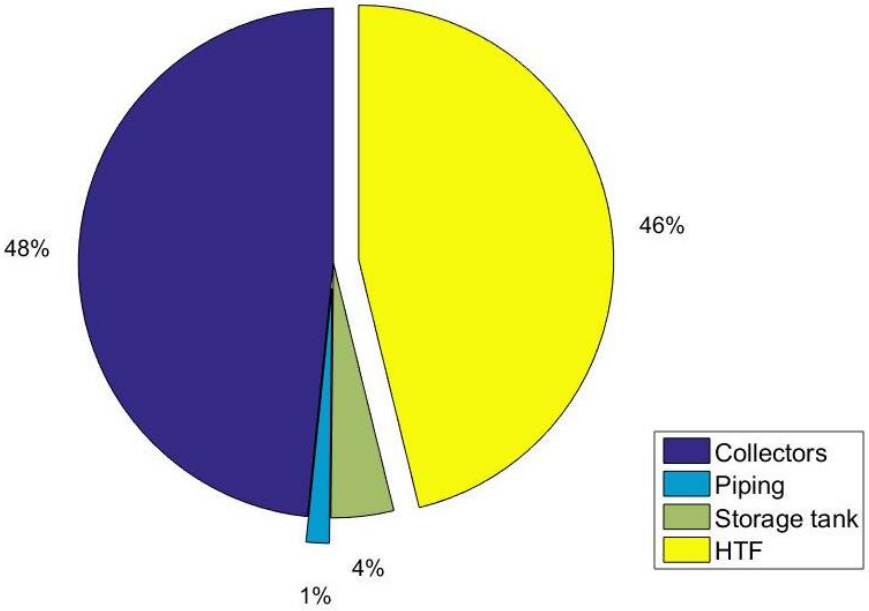

Figure 4.3: Cost distribution for the collectors' system

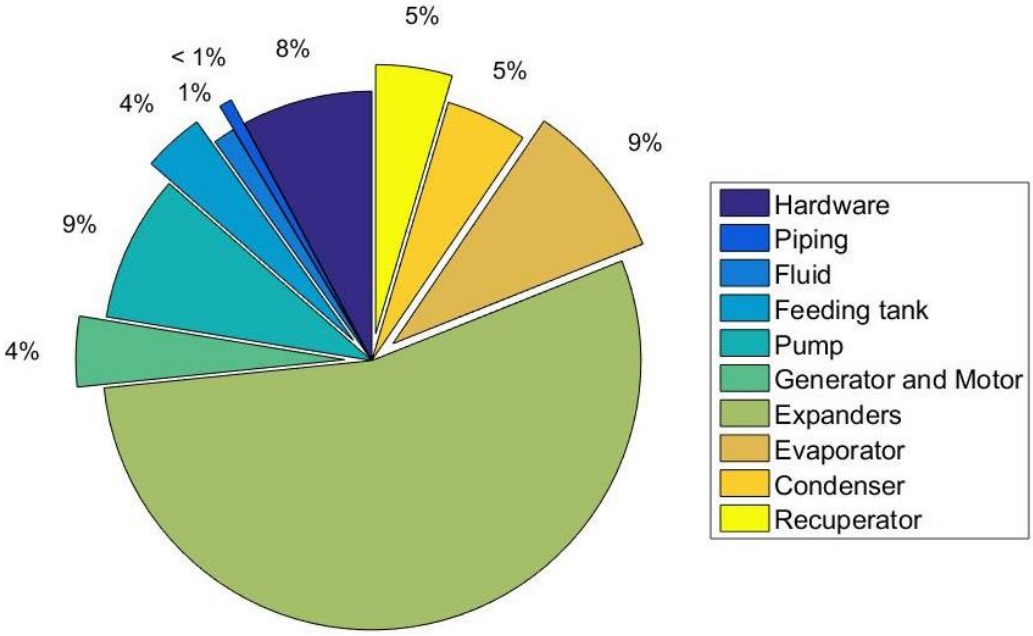

Figure 4.4: Cost distribution for the ORC system

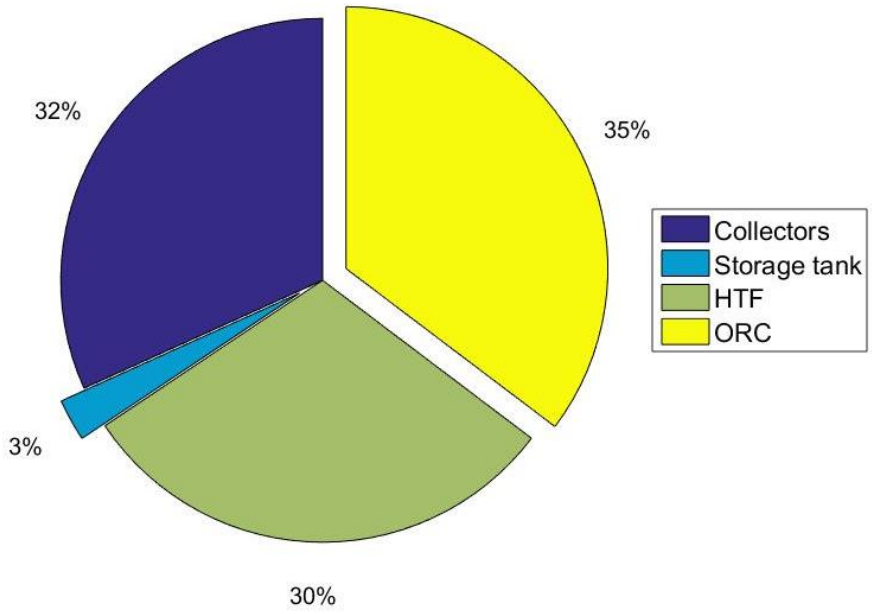

Figure 4.5: Cost distribution for the total system

As can be observed from the above Table 4.4, the cost of the produced power takes very high values compared to the electricity prices shown in Figure 4.2. As the last figure proves, that is because of the really high CAPEX of all the operating systems, since the investment cost is distributed almost equally between the ORC, the collectors and the HTF that fills the storage tank and flows inside the whole collectors' loop. Regarding the ORC itself the major components that increase its cost are the expanders.

For a more thorough presentation of the results, in the following two bar graphs are illustrated the efficiency and the LCoE in case of Athens and PTC for all the examined working fluids:

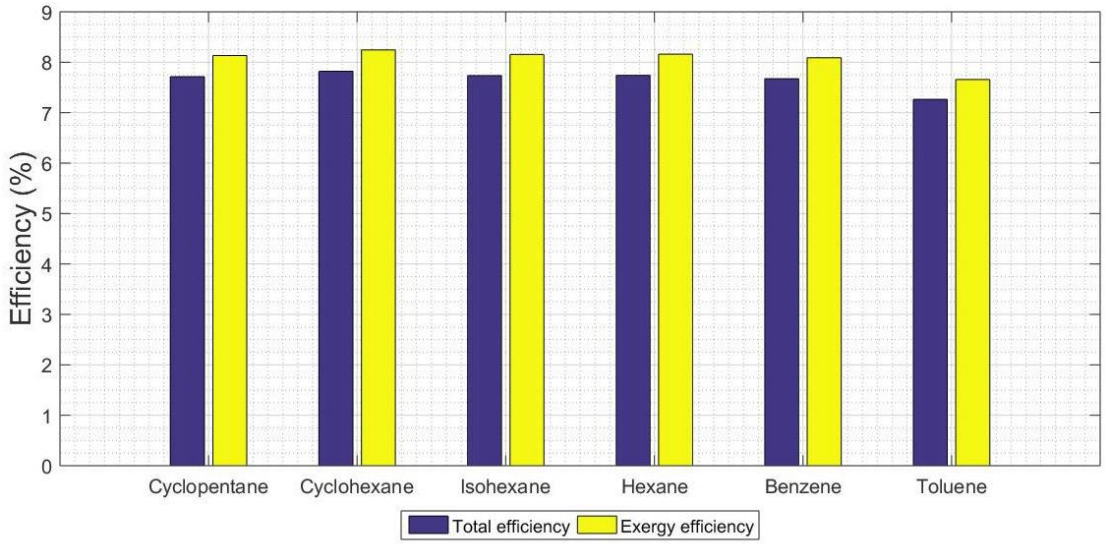

Figure 4.6: Preliminary efficiency results in case of Athens-PTC for all examined fluids

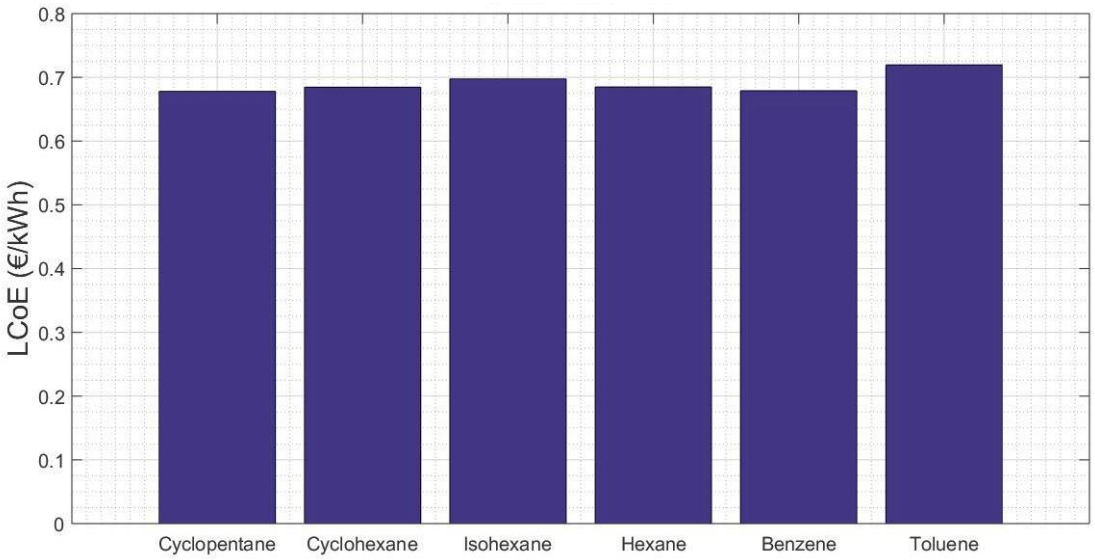

Figure 4.7: Preliminary LCoE results in case of Athens-PTC for all examined fluids

Finally, the same values are demonstrated in a similar way for the case of Cyclopentane and PTC for all the examined cities. It is obvious that in case of the northern cities, in which the total annual irradiance is lower, even though the sun's accumulation is more effective, the financial performance of the system is significantly lower.

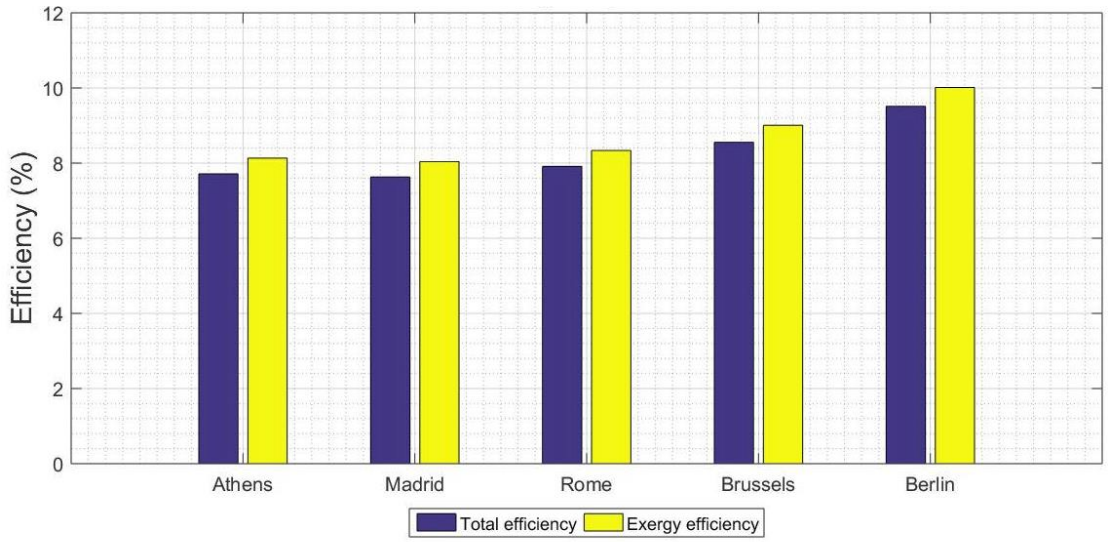

Figure 4.8: Preliminary efficiency results in case of PTC- Cyclopentane for all examined cities

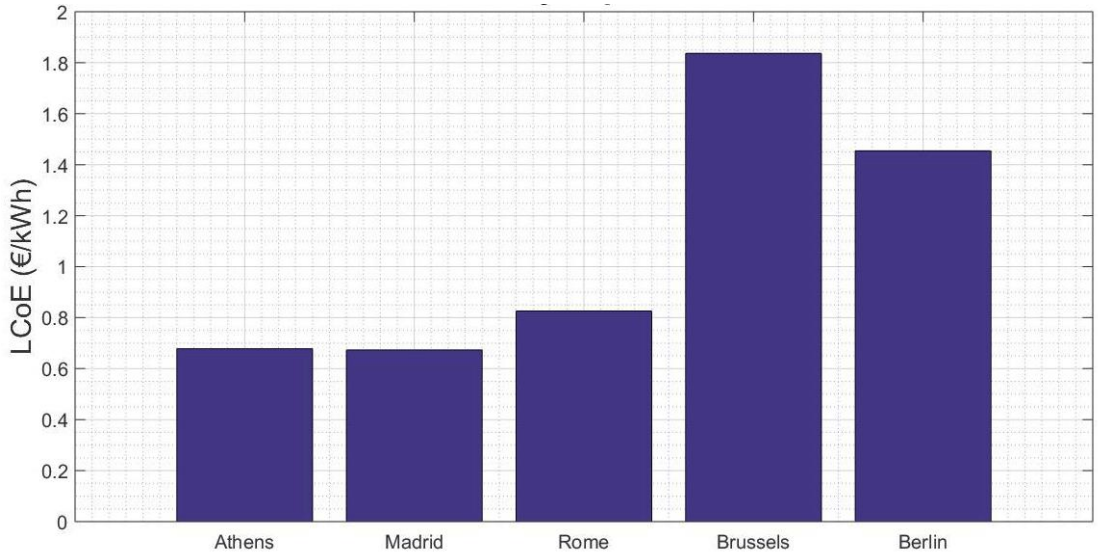

Figure 4.9: Preliminary LCoE results in case of PTC- Cyclopentane for all examined cities

Chapter 5. System Optimization

The main goal of this whole study is to thoroughly model and analyze the function of a solar driven ORC and to determine whether the implementation of this technology is profitable in terms of thermodynamics and economic viability. In order to answer unambiguously, the unit's structure and characteristics that yield their maximum results needs to be determined, thus to optimize the whole configuration. As already mentioned, this optimization should be done in terms of both efficiency and economic feasibility, hence for this study the selected optimization parameters are the system's total efficiency (η_{tot}) and its $LCoE$.

5.1. Genetic algorithm

The selection of two different parameters inserts also multiple criteria in the optimization procedure and requires more than one objective functions. This procedure needs to identify the maximum value of η_{tot}, while minimizing the corresponding $LCoE$. It is obvious that these two objectives are conflicting, since for example a small unit may achieve effective exploitation of the available solar power, but the produced electricity will not be sufficient in order to cover its investment cost, affecting severely its economic performance.

Hence, there is a trade-off between the optimization criteria and thus it cannot be determined one single solution to the problem. On the contrary, there are a number of solutions that each time optimize the problem, known as Pareto optimal solutions [132].

The identification of these solutions requires the use of a multi-objective algorithm. For that reason, it was developed in Matlab a multi-criteria genetic algorithm. The function of a genetic algorithm is based on the theory of evolution, according to which the most dominant solutions produce the next generation of prospective solutions [133].

In case of a problem with two objectives and a given search space of the changing variables, the computational process starts with a random selection of a number of variables from this space, which constitutes the first generation. For each of these variables the objectives are calculated and the results are evaluated. The variables that yield the most suitable results are more likely to reproduce and thus the variables of the next generation are more likely to belong to the same region of the search space [134]. In that way as the generations proceed, multiple Pareto optimal solutions are identified.

As already mentioned, two optimization parameters (objectives) were considered which are also the algorithm's output:

- The system's total efficiency (η_{tot})
- The Levelized Cost of Energy ($LCoE$)

These two values need to be optimized with respect to some of the system's variables, which function also as the inputs of the genetic algorithm. In this case these variables are:

- The collectors' surface (A_{col})
- The volume of the storage tank (V_{st}).

Furthermore, the range in which the two variables vary in order to set the algorithm's search space has to be determined:

- Regarding A_{col} the range of investigated range is between $10\ m^2$ and $400\ m^2$. It is obvious that collecting surface smaller than $10\ m^2$ does not have any practical meaning, whereas the upper limit was set in order to restrict the unit to a small-scale ORC structure.
- The volume of the storage tank V_{st} varies between $0.2\ m^3$ and $5\ m^3$ with both limits set on the same logic.

From the above search space, it was decided for the algorithm to select 50 possible solutions in each generation and to terminate when a total number of 10 generations have been produced.

5.2. Optimization results

Since the examined combinations are 60, the produced results are also numerous, which makes it necessary to group some of them in order to be presented. In the following paragraphs are shown the optimal solutions for each city and collector type for all the examined working fluids, with color differentiation for each of them.

In each case the first figure depicts all the optimal results defined by the genetic algorithm, thus the fluctuation in the optimized objectives, which combined constitute the Pareto front of the solutions. The second figure consists of four subplots. In each one of them is illustrated the variation of the two objectives (n_{tot} and $LCoE$) with respect to the two variables of the system (A_{col} and V_{st}).

I. Athens-PTC

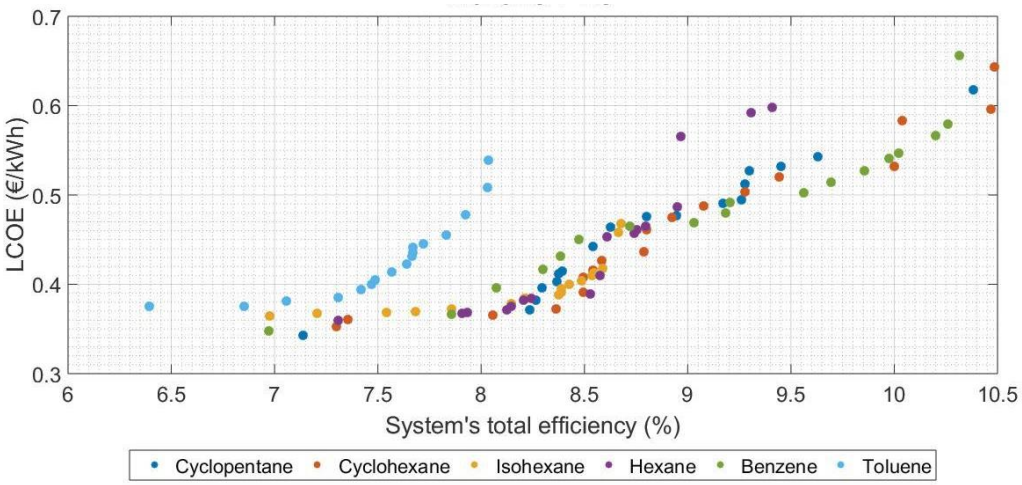

Figure 5.1: Optimization parameters for all the working fluids in case of Athens and PTCs

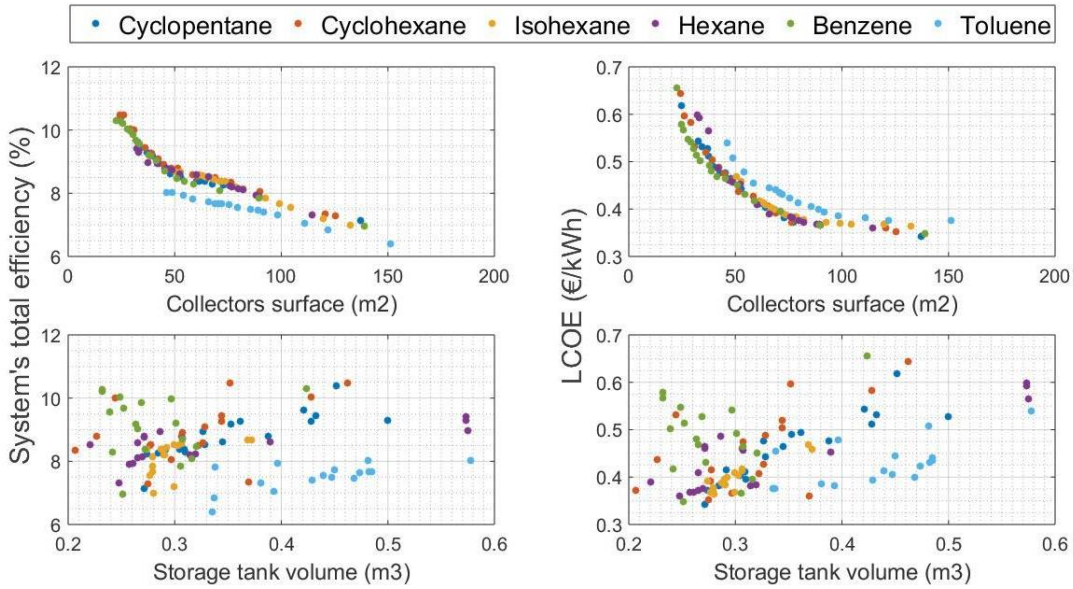

Figure 5.2: Optimization parameters with respect to input variables for all the working fluids in case of Athens and PTCs

II. Athens-PDC

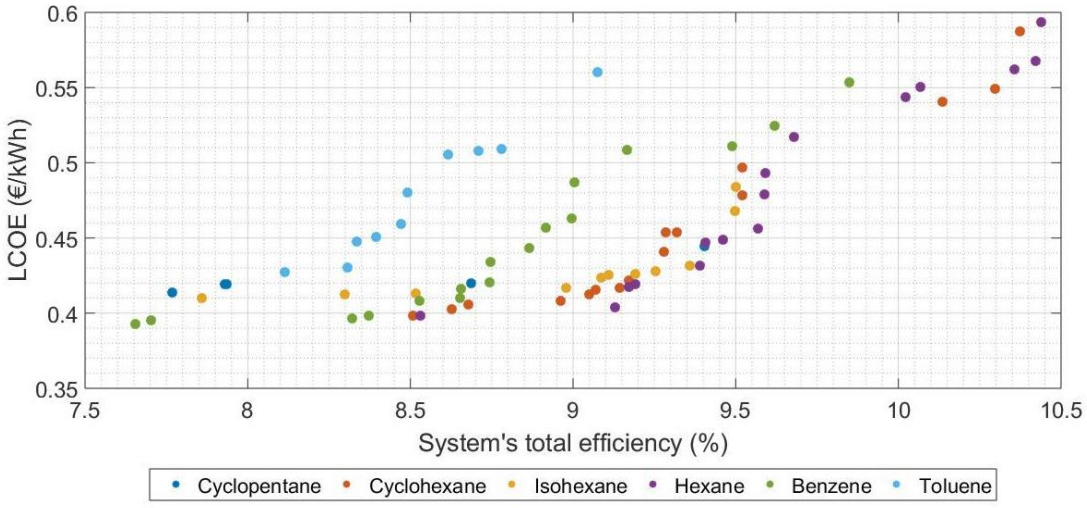

Figure 5.3: Optimization parameters for all the working fluids in case of Athens and PDCs

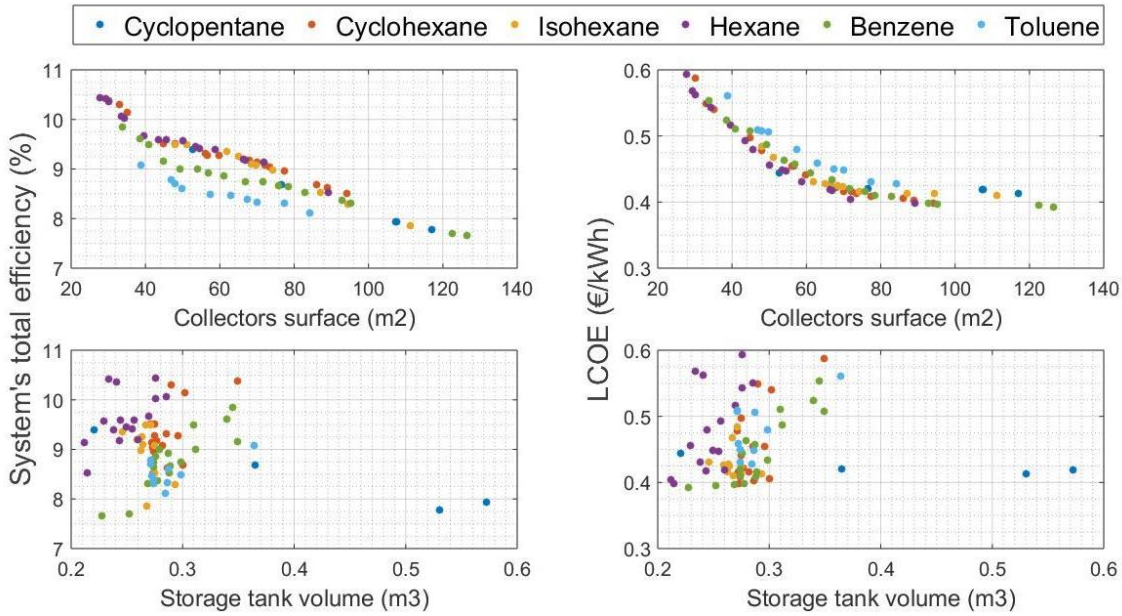

Figure 5.4: Optimization parameters with respect to input variables for all the working fluids in case of Athens and PDCs

III. Madrid-PTC

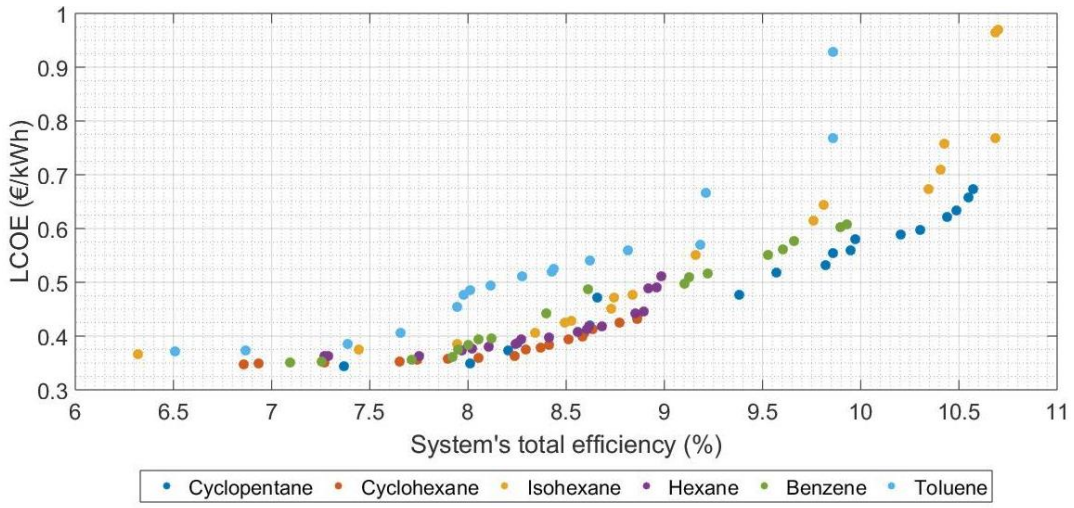

Figure 5.5: Optimization parameters for all the working fluids in case of Madrid and PTCs

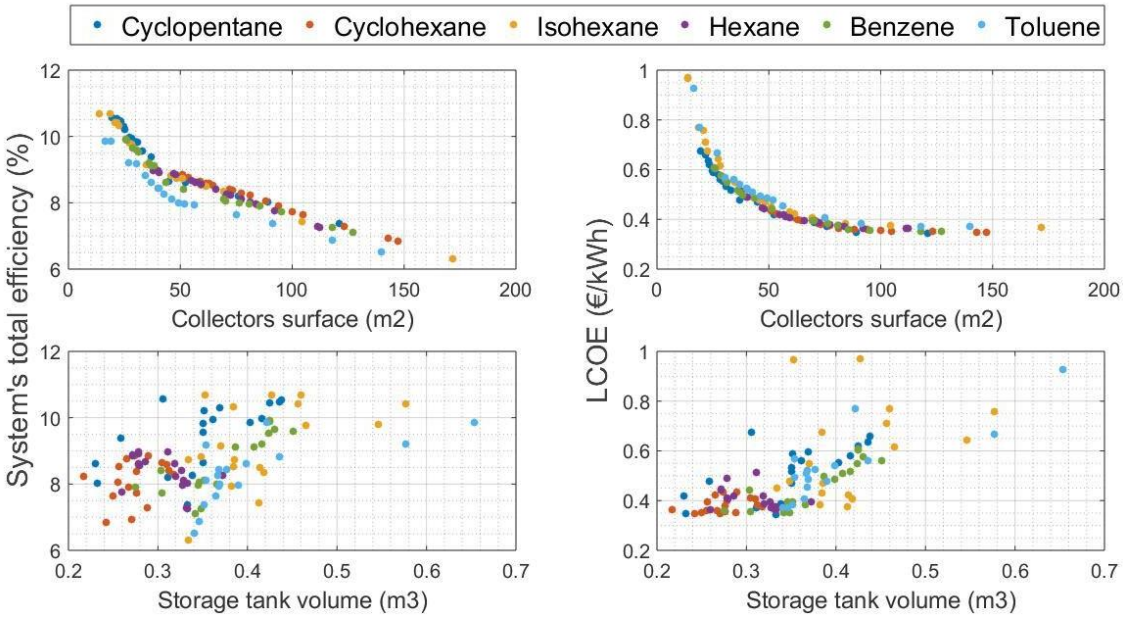

Figure 5.6: Optimization parameters with respect to input variables for all the working fluids in case of Madrid and PTCs

IV. Madrid-PDC

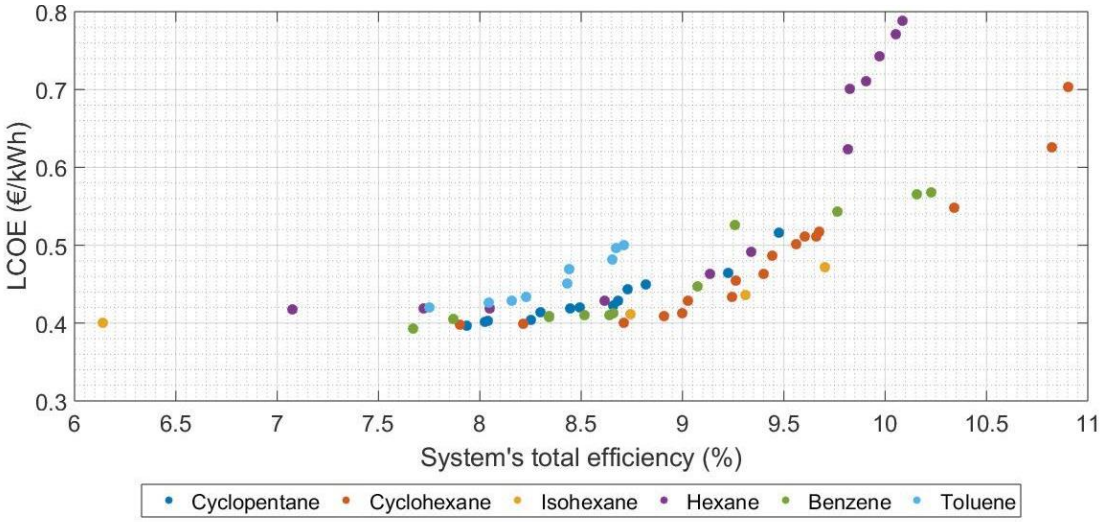

Figure 5.7: Optimization parameters for all the working fluids in case of Madrid and PDCs

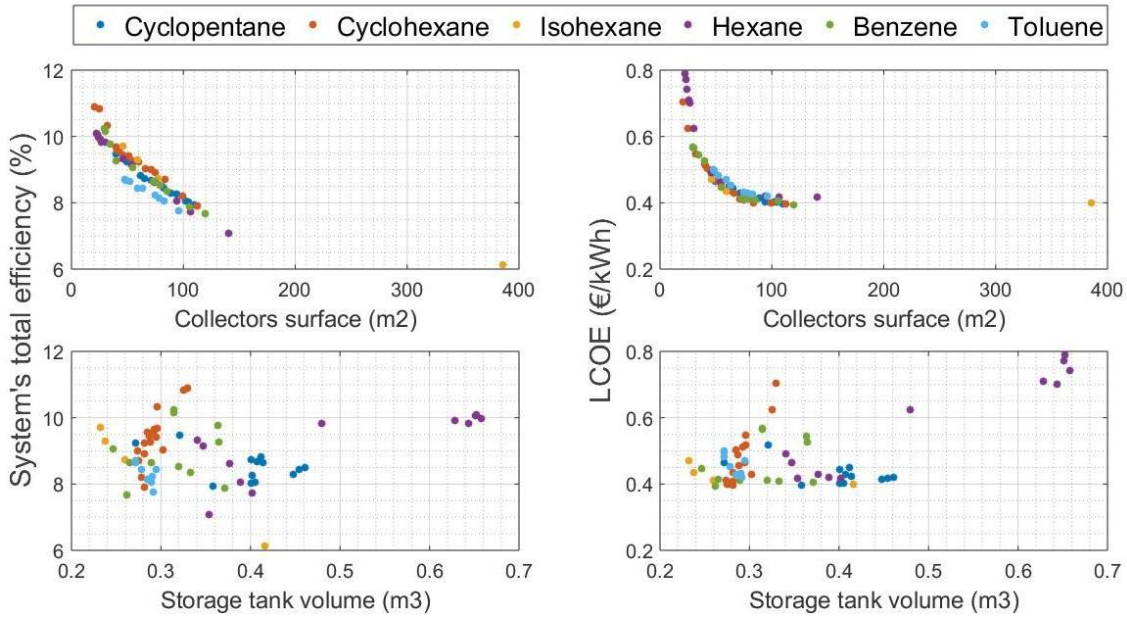

Figure 5.8: Optimization parameters with respect to input variables for all the working fluids in case of Madrid and PDCs

V. Rome-PTC

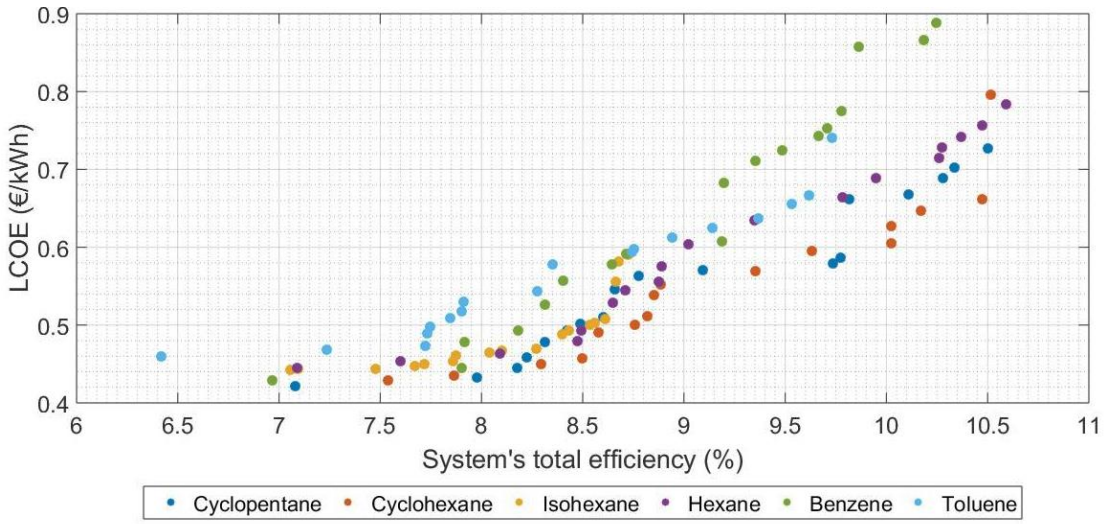

Figure 5.9: Optimization parameters for all the working fluids in case of Rome and PTCs

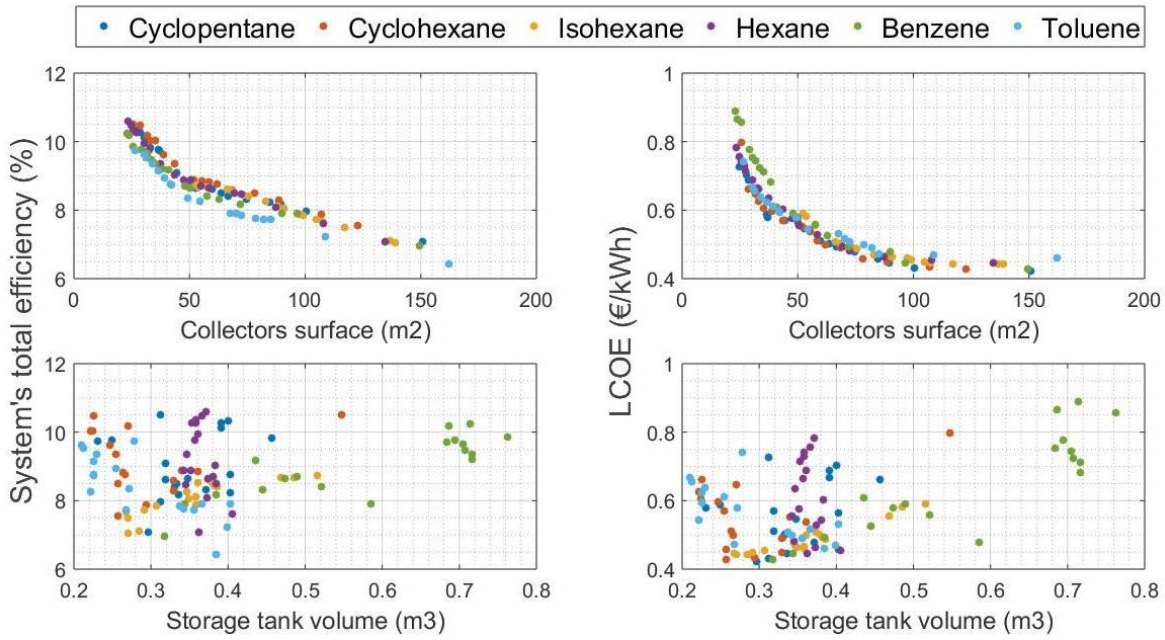

Figure 5.10: Optimization parameters with respect to input variables for all the working fluids in case of Rome and PTCs

VI. Rome-PDC

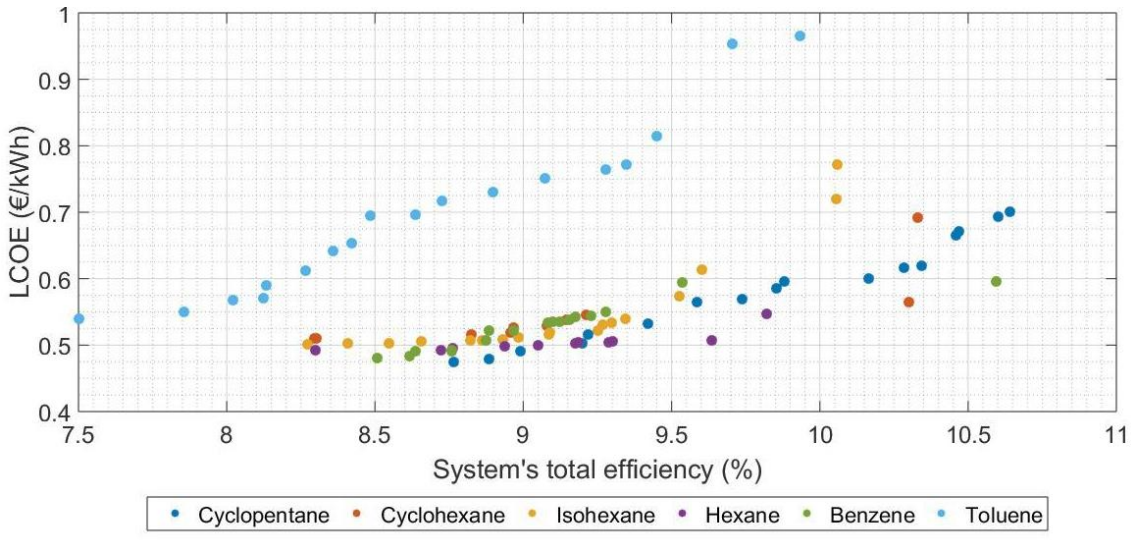

Figure 5.11: Optimization parameters for all the working fluids in case of Rome and PDCs

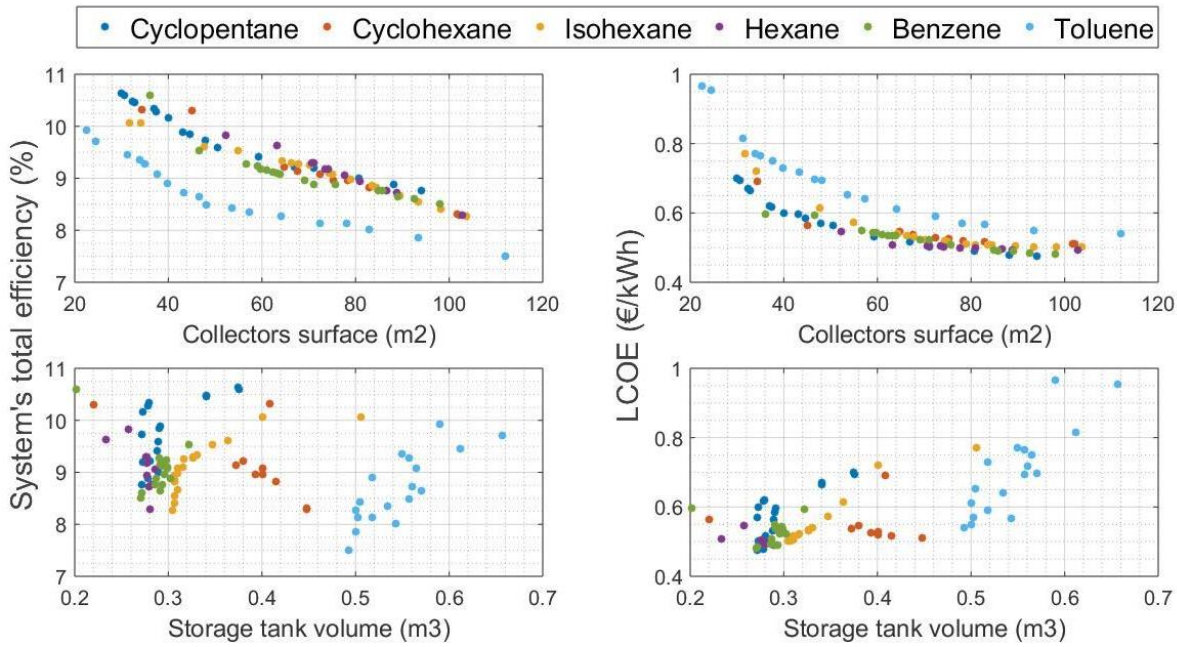

Figure 5.12: Optimization parameters with respect to input variables for all the working fluids in case of Rome and PDCs

VII. Brussels-PTC

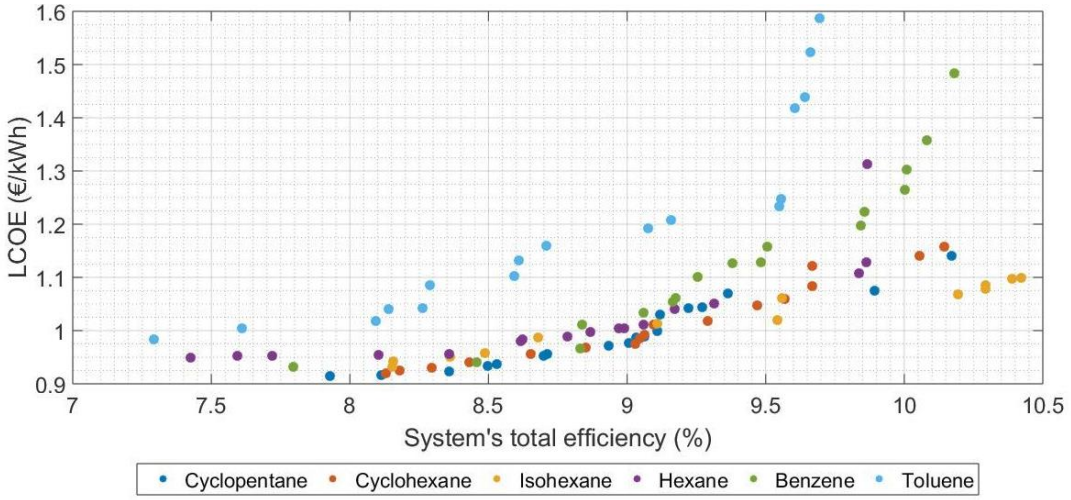

Figure 5.13: Optimization parameters for all the working fluids in case of Brussels and PTCs

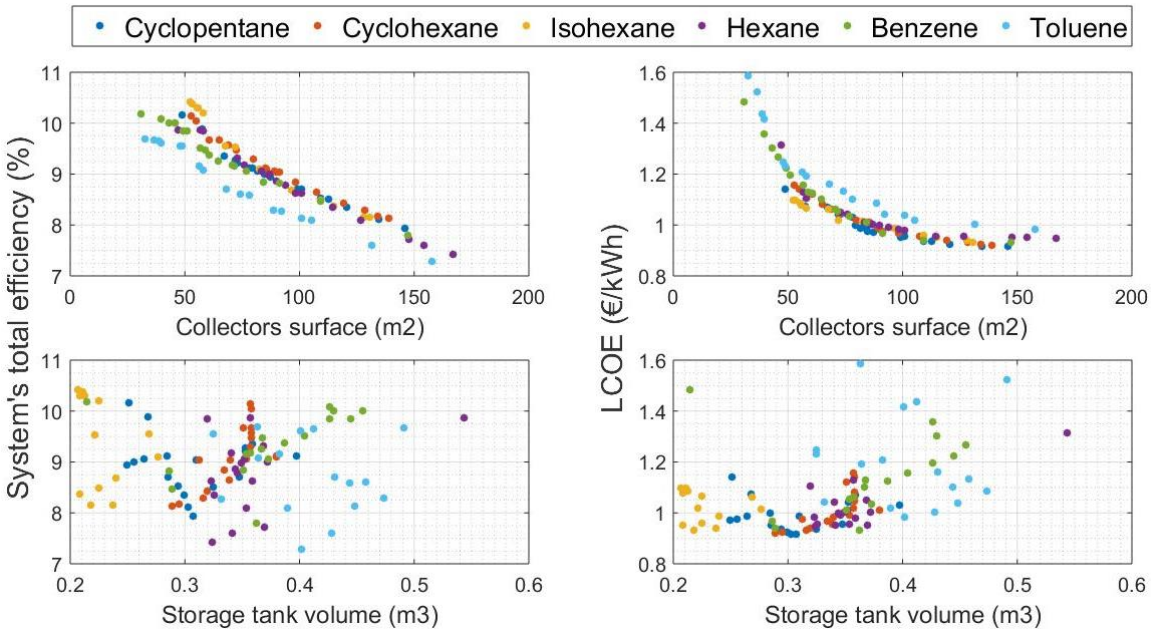

Figure 5.14: Optimization parameters with respect to input variables for all the working fluids in case of Brussels and PTCs

VIII. Brussels-PDC

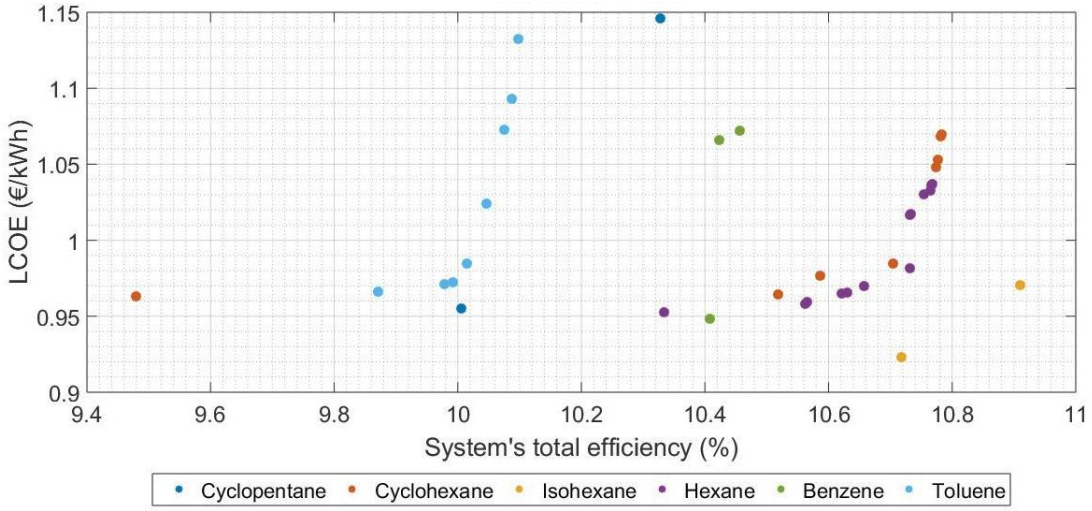

Figure 5.15: Optimization parameters for all the working fluids in case of Brussels and PDCs

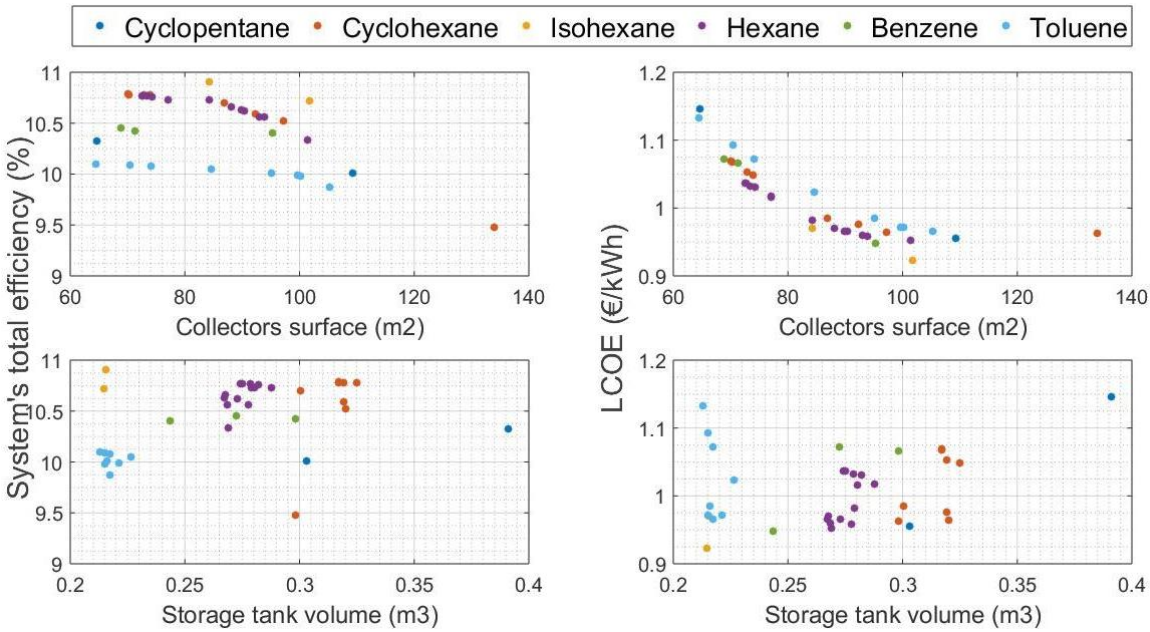

Figure 5.16: Optimization parameters with respect to input variables for all the working fluids in case of Brussels and PDCs

IX. Berlin-PTC

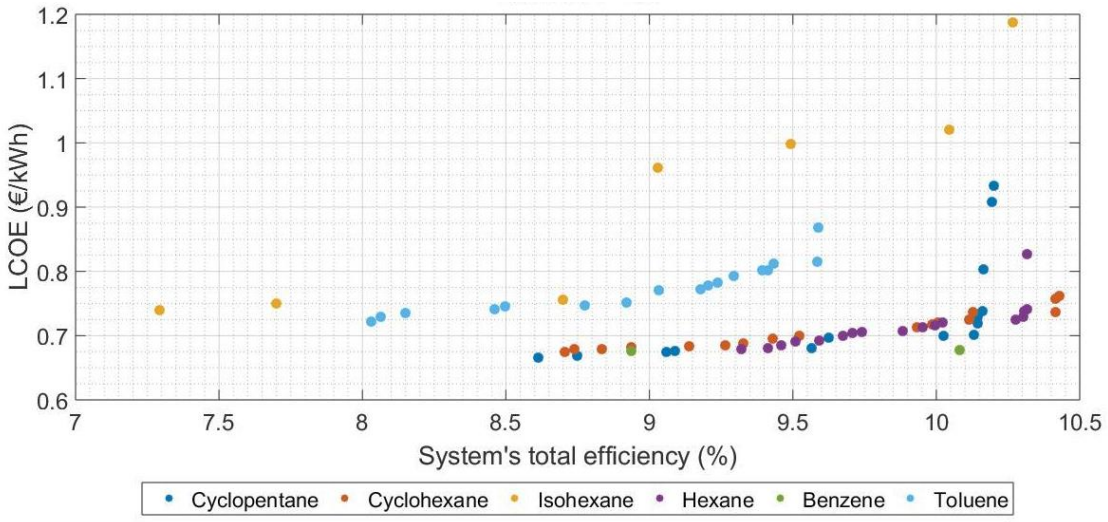

Figure 5.17: Optimization parameters for all the working fluids in case of Berlin and PTCs

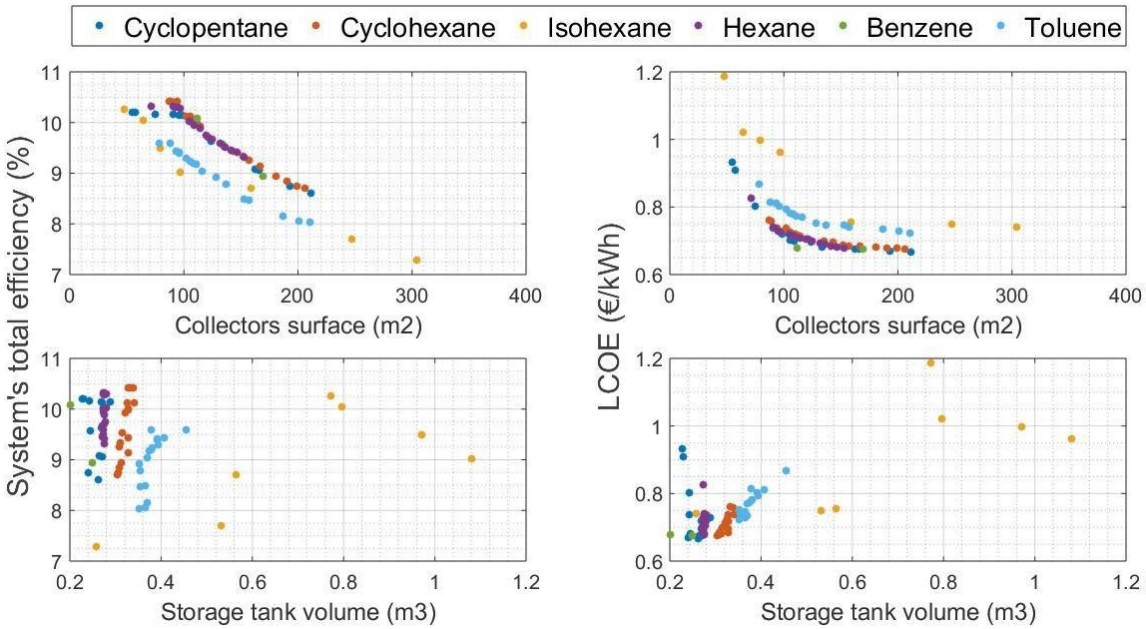

Figure 5.18: Optimization parameters with respect to input variables for all the working fluids in case of Berlin and PTCs

X. Berlin-PDC

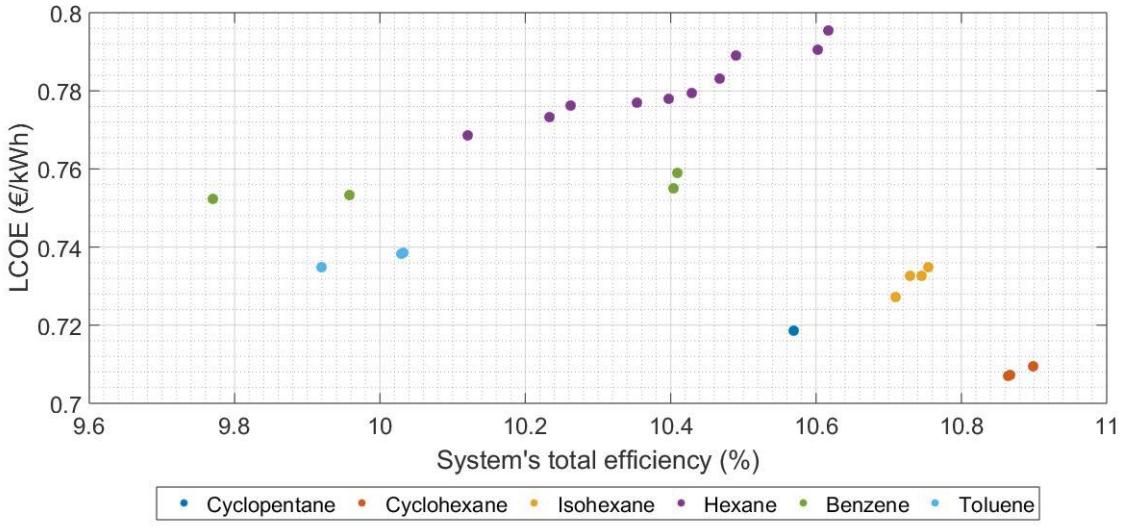

Figure 5.19: Optimization parameters for all the working fluids in case of Berlin and PDCs

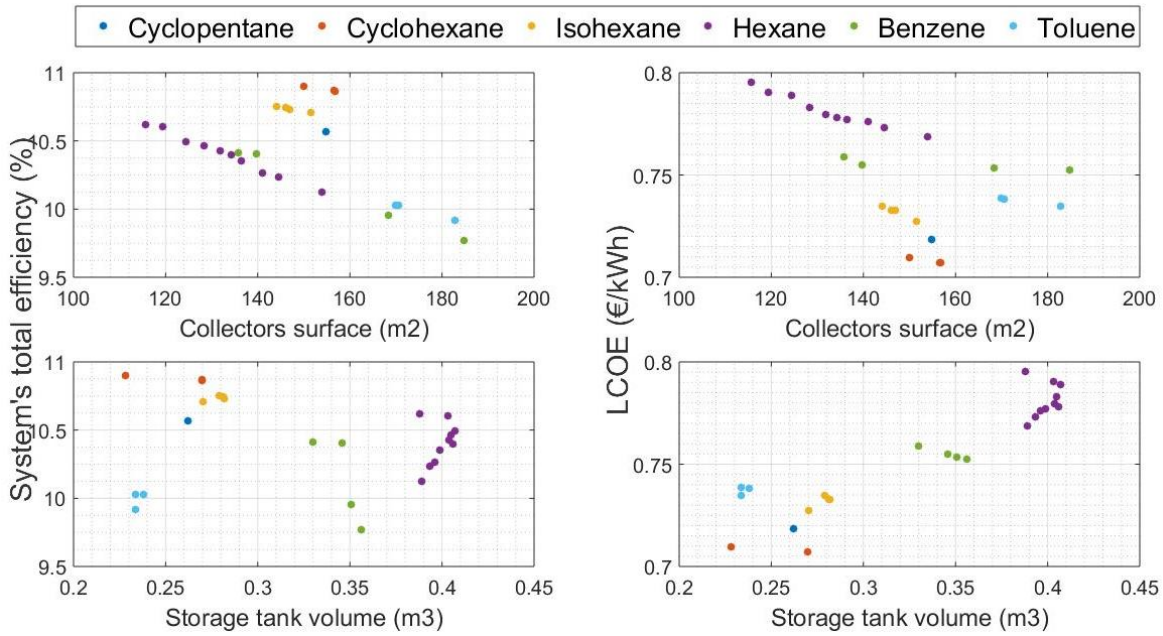

Figure 5.20: Optimization parameters with respect to input variables for all the working fluids in case of Berlin and PDCs

At first, concerning the upper graphs that show the derived Pareto front, it can be observed that in all cases and for all fluids, the form of the curve is similar. A simultaneous increase in the efficiency and the electricity cost can be identified, which justifies the objectives conflict and the trade-off in their optimization. In the right region of the figure the yielded efficiency is at its highest-level reaching values up to 11 %, which means that the available solar irradiance is effectively exploited by the system. At the same time the total cost is also significantly high meaning that there is not sufficiency power production in order to increase the cash inflows. As the efficiency decreases, a concurrent improvement in the economic performance of the system is realized, with LCoE moving towards its lowest values. This left region of the graph corresponds to higher collecting surface compared to the right one. As more collectors are introduced in the system the accumulated energy increases and leads to higher power production and thus higher income. Obviously after a certain number of collectors the addition of supplementary panels simply increases the CAPEX, without offering any benefit in terms of energy production. This region is not depicted in the diagrams since they correspond to both minimized efficiency and financial performance and thus are not approached by the genetic algorithm.

The correlation between the collecting surface and the optimization objectives is shown minutely in the second bottom figure. As it was explained, up to a degree the increase in the collectors' panels decreases both the system's efficiency and the cost of electricity. When the surface is significantly small, the received power is also limited which leads to an almost full use of the energy inflow in order to cover the thermal needs of the ORC. However, at the same time the power output is also limited and thus the total income. As the collecting surface

increases the energy received also augments and thus more energy remains unexploited reducing in that way the overall efficiency. Nevertheless, as it was described above the economic characteristics are improved. Because of that in all the cases shown, the optimization parameters have a descending tendency with respect to the collectors' surface.

As can be seen from the graphs depicting the change with respect to the collectors' surface, the interval given by the algorithm is significantly shorter than the search space that was initially assigned. There are two cases (Madrid-PDC and Berlin-PTC) in which appear very few individual points beyond $250\ m^2$, probably as a result of optimal results identified in the first generation. However, apart from these, the rest of the points in the Pareto fronts do not extend beyond $150 - 200\ m^2$. This comes as a result of the on-design sizing of the system's components. Since the whole unit is relatively small-scale, the heat duty in the evaporator is rather low and can be covered with a small collecting surface. Additional panels would just increase the collected power without improving the power production and thus would deteriorate the optimization objectives.

At this point the characteristics of the curves that show the influence of the storage tank's volume in the optimization parameters have to be discussed. The main fact that is observed is the concentration of all the optimal results in a range of relatively small storage tanks similar to what just mentioned about the collectors' size. Even though the inspected range is between $0.2 - 5\ m^3$ in all cases the derived points correspond to tank capacity lower than $1.2\ m^3$.

This is justified both in terms of efficiency as well as in terms of economic performance. It is obvious that the requirement for a storage tank of higher volume increases its capital cost and thus affects the CAPEX of the total configuration. That can be observed also from the $LCoE - V_{st}$ figures in which there is a tendency of increase in $LCoE$ as V_{st} takes higher values. However, apart from that a larger tank increases the thermal inertia of the system. Larger tanks would demand much higher thermal power from the collectors in order to increase their temperature since they contain larger quantities of HTF and have greater losses towards the environment. Because of that, a smaller storage tank is preferable.

Regarding the geographical comparison of the derived results, the order in which the graphs are presented above is of increasing latitude, which also implies a decrease in the total annual solar irradiance. The graphs that correspond to southern locations (mainly Athens and Madrid) correspond to lower total efficiency and lower LCoE compared to the northern cities (Brussels and Berlin). That happens because in the case of the northern cities the available solar energy is limited, which leads to lower power input in the first place and to almost complete power exploitation from the ORC. Due to that the system's efficiency is relatively high, however, the net generated electricity is reduced along with the cash inflow, and that increases the final LCoE. On the contrary, for southern and more sunny cities, although the accumulated solar irradiance is not used with the same efficiency the net generated electricity is higher and the LCoE decreases.

Concerning the examined working fluids, it can be observed that there is no significant difference between the presented cases. In most of the above diagrams the various curves are relatively close to each other without any substantial difference in favor or against a specific fluid. Because the studied fluids are all hydrocarbons and have in general similar price,

their cost is not a critical parameter in the optimization process, contrary to several refrigerants studied in other ORC systems. Therefore, the main factor that differs them is their thermodynamic performance and, in most cases, their order of preference is similar to the one illustrated in the preliminary Figure 3.19, with Cyclopentane and Cyclohexane being usually the optimal choices and Toluene the least.

Finally, an overall evaluation of the results is presented in the table below, in which for each city are shown the two combinations that lead to the optimization of the two objectives. Concerning the total efficiency, the maximum values yielded vary around $10.5 - 11\ \%$, which is relatively sufficient for this type of systems.

However, the main hindrance for the implementation of this technology is obviously its financial viability. As shown in the table, the optimum LCoE for each city takes values between $0.34 - 0.91\ €/kWh$. In any case these values are higher than the corresponding price of electricity. That means that in terms of economics solely, it is not profitable to install this system. Moreover, since the main criterion for the economic feasibility is the total amount of produced energy, it is obvious that the lowest values of LCoE are achieved in the southern locations where the solar availability, and thus the total production, are higher.

Table 5.1: Optimal working combinations for each city

		Working fluid	Collectors' type	n_{tot} (%)	$LCoE$ $(€/kWh)$	A_{col} (m^2)	V_{st} (m^3)	Electricity price $(€/kWh)$
Athens	**max n_{tot}**	Cyclohexane	PTC	10.49	0.6432	24.37	0.46	0.1646
	min $LCoE$	Cyclopentane	PTC	7.14	0.3432	137.32	0.27	
Madrid	**max n_{tot}**	Cyclohexane	PDC	10.9	0.7034	20.81	0.33	0.2477
	min $LCoE$	Cyclopentane	PTC	7.37	0.3444	120.84	0.33	
Rome	**max n_{tot}**	Cyclopentane	PDC	10.64	0.7010	29.9	0.37	0.2161
	min $LCoE$	Cyclopentane	PTC	7.08	0.4214	150.84	0.30	
Brussels	**max n_{tot}**	Isohexane	PDC	10.91	0.9706	84.22	0.22	0.2937
	min $LCoE$	Cyclopentane	PTC	7.93	0.9146	146.1	0.31	
Berlin	**max n_{tot}**	Cyclohexane	PDC	10.9	0.7096	149.92	0.23	0.3000
	min $LCoE$	Cyclopentane	PTC	8.61	0.6661	211.69	0.26	

5.3. Operational improvements

The main modification in the already studied system is the change in Q_{evap}. The system described so far, when operating at its nominal point, had a heat duty in the evaporator equal to $Q_{evap} = 40\ kW$. For the examined cases below, the nominal heat duty will become the designing variable.

With a new value for Q_{evap}, the ORC analysis and sizing process have to be conducted again from the beginning. The focus lies only in the case of Athens-PTC-Cyclopentane which

provides the minimum cost of energy. As for the variation of Q_{evap} four additional cases were examined with values equal to $25\ kW - 32.5\ kW - 60\ kW - 80\ kW$.

As the value of Q_{evap} decreases an absorption of smaller quantities of power from the system is observed and thus lower energy production in the generators. However, the temperature sink in the collectors and the storage tank is relatively low, and therefore the ORC circuit is more frequently open and in operation. On the contrary, for higher values of Q_{evap} higher energy production is faced in the expanders.

In the following figures are demonstrated the results produced by the genetic algorithm, in a way similar to the previous cases.

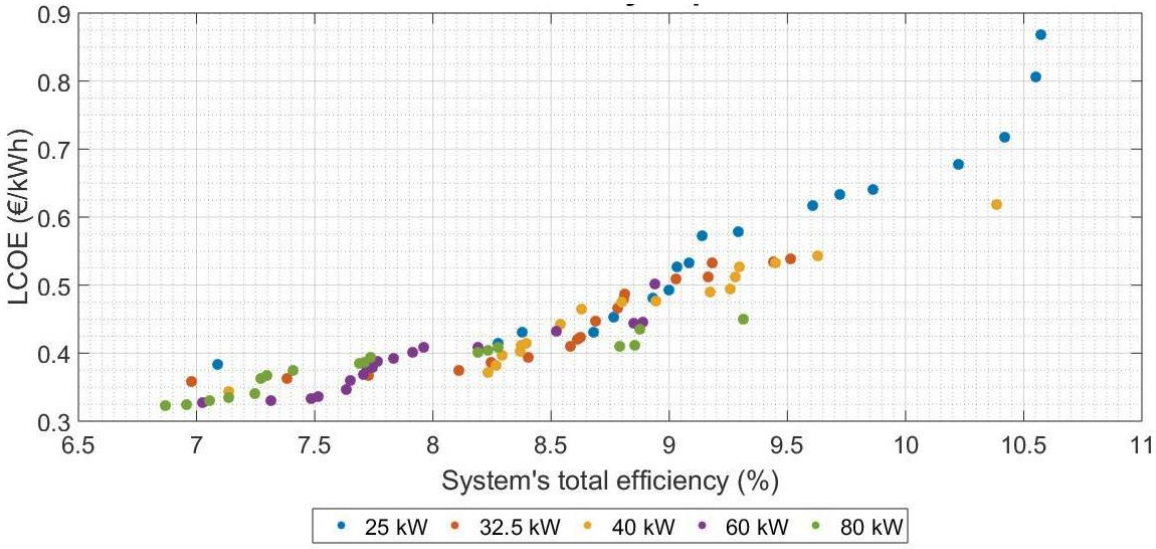

Figure 5.21: Optimization parameters for various nominal Q_{evap} in case of Athens, PTC, Cyclopentane

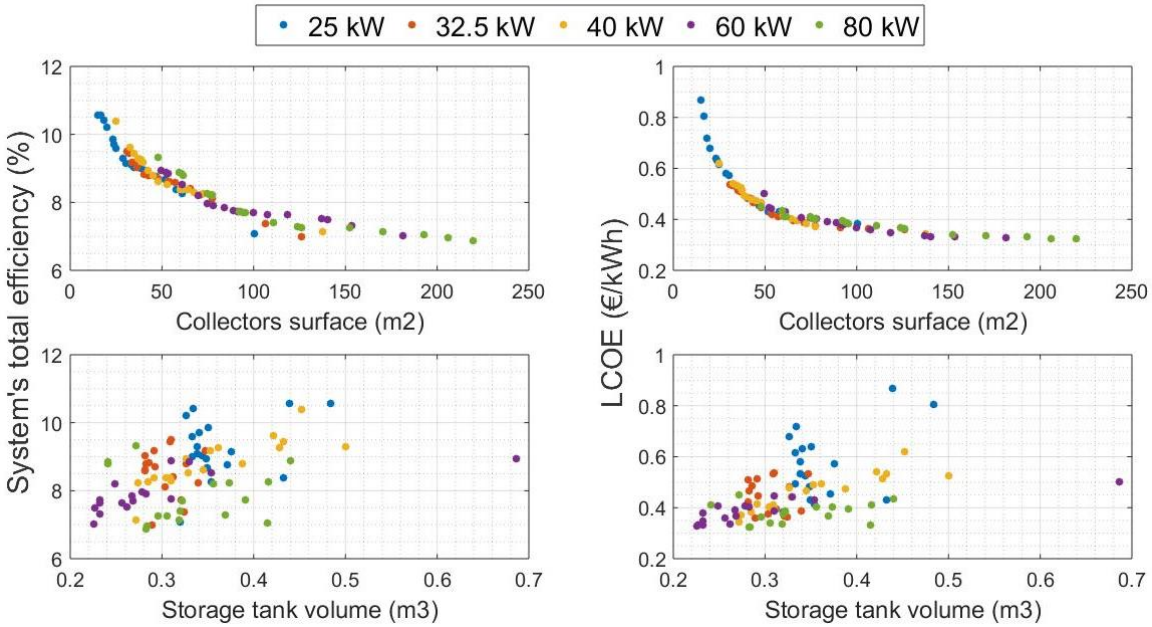

Figure 5.22: Optimization parameters with respect to input variables for various nominal Q_{evap} in case of Athens, PTC, Cyclopentane

Table 5.2: Optimal working combinations for various nominal Q_{evap} in case of Athens, PTC, Cyclopentane

Q_{evap}^{nom}	min $LCoE$ $(€/kWh)$	n_{tot} (%)	A_{col} (m^2)	V_{st} (m^3)
25 kW	0.3839	7.09	100.16	0.32
32.5 kW	0.3588	6.98	126.23	0.29
40 kW	0.3432	7.14	137.32	0.27
60 kW	0.3276	7.03	181.12	0.23
80 kW	0.3229	6.87	219.64	0.28

As one can observe, both from the diagrams and the table, the increase in the evaporator's heat transfer leads also to an increase in the economic viability of the system. However, at the same time the total collectors' surface is increasing, since there are higher needs in the primary energy supply from the heat source. This augmentation of the system's structure is not present in the case of the storage tank which in all the scenarios is relatively small in order to avoid a cost increase due to the higher HTF volume and a raise in its thermal inertia.

Nevertheless, even though there is an improvement in the cost of the produced energy, the final results for the optimal examined case do not ensure the financial feasibility of the system.

The minimum LCoE is equal to $0.3229\ €/kWh$, which is almost double the corresponding price in Greece.

Finally, it can be concluded that a further increase in Q_{evap}^{nom}, with the necessary increase in the collecting surface, may eventually lead to even lower costs of power and even economically profitability of the system. It was attempted to examine the operation for higher values close to $100\ kW$ but the heat load could not be handled by the system's components. However, that is logical and expected since the initial design corresponds to a small-scale unit without excessively high power output.

Chapter 6. Conclusion

6.1. Discussion of key findings

In this study took place the techno-economic analysis of a solar driven ORC system, with relatively low power capacity, using heat sources of medium to high temperature grade. The goal of this assessment was to optimize the configuration and evaluate its energetic and economic performance in five different European cities.

For the solar system two different types of concentrating collectors were modelled, whose characteristics and efficiencies were compared. As for the ORC system, its function was investigated using various working fluids applicable to the examined temperature range of the heat source.

The overall system was optimized using a genetic algorithm and based on the results of the study is concluded that:

- The use of concentrating collectors (PTC and PDC) requires the integration of a sun tracking system, which increases the total solar irradiance absorbed by the collectors, by roughly 7.5% in an annual basis
- In most cases systems using PDCs yield higher energy efficiency, whereas PTCs are linked to financially more profitable results. However, there are no significant differences between the systems with respect to the type of collector used
- The selection of the working fluid is strongly correlated to the temperature of the heat source. The optimum performance is achieved in most cases by working fluids which have critical temperature slightly higher than the cycle's top temperature. In the examined system Cyclopentane and Cyclohexane give the optimal results
- The maximum total energy efficiency in an annual base is around 10.5%-11%. The best results are obtained for northern locations (e.g. Brussels) and lower values of the collecting surface
- On the contrary, the cost of the produced energy is minimized for southern locations (e.g. Athens) and higher values of the collecting surface. However, its minimum value is at least around 1.5 times higher than the current commercial cost of energy
- An improvement of the economic performance of the system can be achieved by increasing its power production

6.2. Suggestions for future work

The current study allows the further investigation of a system similar to the one already examined. With regards to future work, the following topics could be of significant interest:

- A sensitivity analysis of the economic performance of the system with respect to the fluctuations in the cost of various components as for example the solar collectors, the heat transfer fluid or the screw expander as well as with respect to the cost of electricity in each city

- The study of various different cities with alternate meteorological characteristics and different cost of energy
- The investigation of the system's operation with multiple outputs (incorporation of heat or/and cooling production)
- The extension of the system's power capacity. Analysis of a unit with upgraded power output, in order to improve the economic performance and design a profitable energy production system
- The examination of a similar configuration in which the storage tank is substituted by a smaller tank used simply as a buffer in order to decrease the amounts of the needed heat transfer fluid and reduce the total cost.

References

1. W. Black, J.H., *Εφαρμοσμένη Θερμοδυναμική*. 1995: Εκδόσεις Ίων
2. Ε. Κακαράς, Σ.Κ., *Αποκεντρωμένα Θερμικά Συστήματα*. 2015: Εκδόσεις Τσότρας.
3. Ε. Κακαράς, Σ.Κ., *Αντιρρυπαντική Τεχνολογία Θερμικών Σταθμών*. 2013: Εκδόσεις Τσότρας.
4. Μαθιουδάκης, Κ., *Λειτουργία Αεριοστροβίλων και Ατμοστροβίλων*. 2007: Ε.Μ.Π.
5. Quoilin, S., et al., *Techno-economic survey of Organic Rankine Cycle (ORC) systems.* Renewable and Sustainable Energy Reviews, 2013. **22**: p. 168-186.
6. Tartière, T. and M. Astolfi, *A World Overview of the Organic Rankine Cycle Market.* Energy Procedia, 2017. **129**: p. 2-9.
7. Vélez, F., et al., *A technical, economical and market review of organic Rankine cycles for the conversion of low-grade heat for power generation.* Renewable and Sustainable Energy Reviews, 2012. **16**(6): p. 4175-4189.
8. S. Karellas, T.C.R., *Solar Thermal Power Plants, Chapter 7 in Hydrogen Production from Solar Energy.*
9. Delgado-Torres, A.M. and L. García-Rodríguez, *Analysis and optimization of the low-temperature solar organic Rankine cycle (ORC).* Energy conversion and Management, 2010. **51**(12): p. 2846-2856.
10. Braimakis, K., et al., *Comparison of Environmentally Friendly Working Fluids for Organic Rankine Cycles*, in *Advances in New Heat Transfer Fluids*. 2017, CRC Press. p. 377-426.
11. Bao, J. and L. Zhao, *A review of working fluid and expander selections for organic Rankine cycle.* Renewable and sustainable energy reviews, 2013. **24**: p. 325-342.
12. Imran, M., et al., *Thermoeconomic analysis of Organic Rankine Cycle using zeotropic mixtures*. 2015.
13. Colonna, P., et al., *Organic Rankine cycle power systems: from the concept to current technology, applications, and an outlook to the future.* Journal of Engineering for Gas Turbines and Power, 2015. **137**(10): p. 100801.
14. Roumpedakis, T., K. Braimakis, and S. Karellas, *Investigation and efficiency maximization of the operation and design of a small scale experimental trigeneration system powered by a supercritical ORC*. 2015.
15. Karellas, S., A. Schuster, and A.-D. Leontaritis, *Influence of supercritical ORC parameters on plate heat exchanger design.* Applied Thermal Engineering, 2012. **33-34**: p. 70-76.
16. Boz, B. and A. Diez, *Comparative Study of Sub-Critical and Supercritical ORC Applications for Exhaust Waste Heat Recovery.* World Academy of Science, Engineering and Technology, International Journal of Energy and Power Engineering, 2018. **12**(2): p. 119 - 127.
17. Peñate, B. and L. García-Rodríguez, *Current trends and future prospects in the design of seawater reverse osmosis desalination technology.* Desalination, 2012. **284**: p. 1-8.
18. Delgado-Torres, A.M. and L. García-Rodríguez, *Preliminary assessment of solar organic Rankine cycles for driving a desalination system.* Desalination, 2007. **216**(1-3): p. 252-275.
19. Delgado-Torres, A.M., L. García-Rodríguez, and V.J. Romero-Ternero, *Preliminary design of a solar thermal-powered seawater reverse osmosis system.* Desalination, 2007. **216**(1-3): p. 292-305.
20. Delgado-Torres, A.M. and L. García-Rodríguez, *Comparison of solar technologies for driving a desalination system by means of an organic Rankine cycle.* Desalination, 2007. **216**(1-3): p. 276-291.

21. Bruno, J.C., et al., *Modelling and optimisation of solar organic rankine cycle engines for reverse osmosis desalination.* Applied Thermal Engineering, 2008. **28**(17): p. 2212-2226.
22. Quoilin, S., et al., *Performance and design optimization of a low-cost solar organic Rankine cycle for remote power generation.* Solar Energy, 2011. **85**(5): p. 955-966.
23. Desai, N.B. and S. Bandyopadhyay, *Thermo-economic analysis and selection of working fluid for solar organic Rankine cycle.* Applied Thermal Engineering, 2016. **95**: p. 471-481.
24. Pikra, G., et al., *Development of small scale concentrated solar power plant using organic Rankine cycle for isolated region in Indonesia.* Energy Procedia, 2013. **32**: p. 122-128.
25. Calise, F., et al., *Design and simulation of a prototype of a small-scale solar CHP system based on evacuated flat-plate solar collectors and Organic Rankine Cycle.* Energy Conversion and Management, 2015. **90**: p. 347-363.
26. Patil, V.R., et al., *Techno-economic comparison of solar organic Rankine cycle (ORC) and photovoltaic (PV) systems with energy storage.* Renewable energy, 2017. **113**: p. 1250-1260.
27. Chacartegui, R., et al., *Analysis of two heat storage integrations for an Organic Rankine Cycle Parabolic trough solar power plant.* Energy Conversion and Management, 2016. **125**: p. 353-367.
28. Nafey, A. and M. Sharaf, *Combined solar organic Rankine cycle with reverse osmosis desalination process: energy, exergy, and cost evaluations.* Renewable Energy, 2010. **35**(11): p. 2571-2580.
29. Nafey, A., M. Sharaf, and L. García-Rodríguez, *Thermo-economic analysis of a combined solar organic Rankine cycle-reverse osmosis desalination process with different energy recovery configurations.* Desalination, 2010. **261**(1-2): p. 138-147.
30. Casati, E., A. Galli, and P. Colonna, *Thermal energy storage for solar-powered organic Rankine cycle engines.* Solar energy, 2013. **96**: p. 205-219.
31. Kumar, A. and S. Shukla, *Analysis and performance of ORC based solar thermal power plant using benzene as a working fluid.* Procedia Technology, 2016. **23**: p. 454-463.
32. Alvi, J.Z., et al., *Thermodynamic comparison and dynamic simulation of direct and indirect solar organic Rankine cycle systems with PCM storage.* Energy Procedia, 2017. **129**: p. 716-723.
33. Ferrara, F., A. Gimelli, and A. Luongo, *Small-scale concentrated solar power (CSP) plant: ORCs comparison for different organic fluids.* Energy Procedia, 2014. **45**: p. 217-226.
34. Xu, G., et al., *Performance evaluation of a direct vapor generation supercritical ORC system driven by linear Fresnel reflector solar concentrator.* Applied Thermal Engineering, 2015. **80**: p. 196-204.
35. Bellos, E. and C. Tzivanidis, *Investigation of a hybrid ORC driven by waste heat and solar energy.* Energy conversion and management, 2018. **156**: p. 427-439.
36. Sharaf, M.A., A.S. Nafey, and L. García-Rodríguez, *Exergy and thermo-economic analyses of a combined solar organic cycle with multi effect distillation (MED) desalination process.* Desalination, 2011. **272**(1): p. 135-147.
37. Sharaf, M.A., A.S. Nafey, and L. García-Rodríguez, *Thermo-economic analysis of solar thermal power cycles assisted MED-VC (multi effect distillation-vapor compression) desalination processes.* Energy, 2011. **36**(5): p. 2753-2764.

38. Maraver, D., J. Uche, and J. Royo, *Assessment of high temperature organic Rankine cycle engine for polygeneration with MED desalination: A preliminary approach.* Energy Conversion and Management, 2012. **53**(1): p. 108-117.
39. Αντωνόπουλος, Κ., *Θερμικά Ηλιακά Συστήματα*, ed. Ε. Ε.Μ.Π. 2015.
40. Tian, Y. and C.-Y. Zhao, *A review of solar collectors and thermal energy storage in solar thermal applications.* Applied energy, 2013. **104**: p. 538-553.
41. Roumpedakis, T., *Techo-economic investigations of a solar driven ORC-sorption system for combined cooling, heating and power*. 2018, Delft University of Technology.
42. Zhu, G., et al., *History, current state, and future of linear Fresnel concentrating solar collectors.* Solar Energy, 2014. **103**: p. 639-652.
43. Suman, S., M.K. Khan, and M. Pathak, *Performance enhancement of solar collectors—A review.* Renewable and Sustainable Energy Reviews, 2015. **49**: p. 192-210.
44. EASTMAN, C.C. *Therminol D-12, Technical Data Sheet, Available: https://www.therminol.com/products/Therminol-d12*. 2016.
45. EASTMAN, C.C. *Therminol VP-1, Technical Data Sheet, Available: https://www.therminol.com/products/Therminol-VP1*. 2016.
46. Sefa, I., M. Demirtas, and I. Çolak, *Application of one-axis sun tracking system.* Energy conversion and Management, 2009. **50**(11): p. 2709-2718.
47. Crawley, D.B., et al., *Energy plus: energy simulation program.* ASHRAE journal, 2000. **42**(4): p. 49-56.
48. Ferreira, C.I. and D.-S. Kim, *Techno-economic review of solar cooling technologies based on location-specific data.* International Journal of Refrigeration, 2014. **39**: p. 23-37.
49. Coccia, G., G. Di Nicola, and M. Sotte, *Design, manufacture, and test of a prototype for a parabolic trough collector for industrial process heat.* Renewable energy, 2015. **74**: p. 727-736.
50. Sotte, M., *Design, test and mathematical modeling of parabolic trough solar collectors.* 2012.
51. Yılmaz, I., et al. *Performance testing of a parabolic trough collector array*. in *The 6th international congress of energy and environment engineering and management (CIIEM15). Paris (France)*. 2015.
52. Arasu, A.V. and T. Sornakumar, *Design, manufacture and testing of fiberglass reinforced parabola trough for parabolic trough solar collectors.* Solar Energy, 2007. **81**(10): p. 1273-1279.
53. Venegas-Reyes, E., et al., *Design, construction, and testing of a parabolic trough solar concentrator for hot water and low enthalpy steam generation.* Journal of renewable and sustainable energy, 2012. **4**(5): p. 053103.
54. Kasaeian, A., et al., *Performance evaluation and nanofluid using capability study of a solar parabolic trough collector.* Energy Conversion and Management, 2015. **89**: p. 368-375.
55. Jaramillo, O., et al., *Parabolic trough concentrators for low enthalpy processes.* Renewable Energy, 2013. **60**: p. 529-539.
56. Murphy, L.M. and E.K. May, *Steam generation in line-focus solar collectors: a comparative assessment of thermal performance, operating stability, and cost issues*. 1982, Solar Energy Research Inst., Golden, CO (USA).
57. Brooks, M. and T. Harms, *Design, construction and testing of a parabolic trough solar collector for a developing-country application.* 2005.
58. Hurtado, P. and M. Kast, *Experimental study of direct in-situ generation of steam in a line focus solar collector. Final report*. 1984, Research Engineering Associates, Palo Alto, CA (USA).

59. Rosado Hau, N. and M. Escalante Soberanis, *Efficiency of a parabolic trough collector as a water heater system in Yucatán, Mexico.* Journal of Renewable and Sustainable Energy, 2011. **3**(6): p. 063108.
60. Kalogirou, S.A., et al., *Design and performance characteristics of a parabolic-trough solar-collector system.* Applied energy, 1994. **47**(4): p. 341-354.
61. Kalogirou, S., *Parabolic trough collector system for low temperature steam generation: design and performance characteristics.* Applied Energy, 1996. **55**(1): p. 1-19.
62. Subramani, J., et al., *Efficiency and heat transfer improvements in a parabolic trough solar collector using TiO2 nanofluids under turbulent flow regime.* Renewable energy, 2018. **119**: p. 19-31.
63. Jaramillo, O., et al., *Parabolic trough solar collector for low enthalpy processes: An analysis of the efficiency enhancement by using twisted tape inserts.* Renewable energy, 2016. **93**: p. 125-141.
64. Cabrera, F., et al., *Use of parabolic trough solar collectors for solar refrigeration and air-conditioning applications.* Renewable and Sustainable Energy Reviews, 2013. **20**: p. 103-118.
65. N.E.P., S., *Technical data for the polytrough 1200B*. 2011.
66. Zadeh, P.M., et al., *Hybrid optimization algorithm for thermal analysis in a solar parabolic trough collector based on nanofluid.* Energy, 2015. **82**: p. 857-864.
67. Dudley, V.E., et al., *Test results: SEGS LS-2 solar collector.* Nasa Sti/recon Technical Report N, 1994. **96**.
68. Forristall, R., *Heat transfer analysis and modeling of a parabolic trough solar receiver implemented in engineering equation solver*. 2003, National Renewable Energy Lab., Golden, CO.(US).
69. Hachicha, A., et al., *Heat transfer analysis and numerical simulation of a parabolic trough solar collector.* Applied energy, 2013. **111**: p. 581-592.
70. Moloodpoor, M., A. Mortazavi, and N. Ozbalta, *Thermal analysis of parabolic trough collectors via a swarm intelligence optimizer.* Solar Energy, 2019. **181**: p. 264-275.
71. Wu, S.-Y., et al., *A parabolic dish/AMTEC solar thermal power system and its performance evaluation.* Applied Energy, 2010. **87**(2): p. 452-462.
72. Moradi, M. and M. Mehrpooya, *Optimal design and economic analysis of a hybrid solid oxide fuel cell and parabolic solar dish collector, combined cooling, heating and power (CCHP) system used for a large commercial tower.* Energy, 2017. **130**: p. 530-543.
73. Loni, R., et al., *Experimental and numerical study on dish concentrator with cubical and cylindrical cavity receivers using thermal oil.* Energy, 2018. **154**: p. 168-181.
74. Bianchini, A., et al., *Performance assessment of a solar parabolic dish for domestic use based on experimental measurements.* Renewable Energy, 2019. **133**: p. 382-392.
75. Stefanovic, V.P., et al., *A detailed parametric analysis of a solar dish collector.* Sustainable Energy Technologies and Assessments, 2018. **25**: p. 99-110.
76. Duffie, J.A., W.A. Beckman, and W. Worek, *Solar engineering of thermal processes*. Vol. 3. 2013: Wiley Online Library.
77. Wischhusen, S. *An enhanced discretization method for storage tank models within energy systems*. in *Proc. of the 5-th International Modelica Conference*. 2006.
78. Rahman, A., A.D. Smith, and N. Fumo, *Performance modeling and parametric study of a stratified water thermal storage tank.* Applied Thermal Engineering, 2016. **100**: p. 668-679.

79. Bellos, E., C. Tzivanidis, and K.A. Antonopoulos, *Exergetic and energetic comparison of LiCl-H2O and LiBr-H2O working pairs in a solar absorption cooling system.* Energy conversion and management, 2016. **123**: p. 453-461.
80. Bellos, E., C. Tzivanidis, and K.A. Antonopoulos, *Exergetic, energetic and financial evaluation of a solar driven absorption cooling system with various collector types.* Applied Thermal Engineering, 2016. **102**: p. 749-759.
81. Tzivanidis, C., et al., *Thermal and optical efficiency investigation of a parabolic trough collector.* Case Studies in Thermal Engineering, 2015. **6**: p. 226-237.
82. Fernández-García, A., et al., *Parabolic-trough solar collectors and their applications.* Renewable and Sustainable Energy Reviews, 2010. **14**(7): p. 1695-1721.
83. Kalogirou, S.A., *Solar thermal collectors and applications.* Progress in energy and combustion science, 2004. **30**(3): p. 231-295.
84. Α. Στέγγου, Ζ.Σ., *Μετάδοση Θερμότητας*. 2016: Ε.Μ.Π.
85. Bejan, A. and A.D. Kraus, *Heat transfer handbook*. Vol. 1. 2003: John Wiley & Sons.
86. Rohsenow, W.M., J.P. Hartnett, and Y.I. Cho, *Handbook of heat transfer*. Vol. 3. 1998: McGraw-Hill New York.
87. Thulukkanam, K., *Heat exchanger design handbook*. 2013: CRC press.
88. Alfa_Laval. *Brazed plate heat exchanger AC30EQ, Available: https://www.alfalaval.com/globalassets/documents/products/heat-transfer/plate-heat-exchangers/brazed-plate-heat-exchangers/ac/ac30eq--ach30eq.pdf*. 2016.
89. Bell, I.H., et al., *Pure and Pseudo-pure Fluid Thermophysical Property Evaluation and the Open-Source Thermophysical Property Library CoolProp, Available: http://www.coolprop.org/.* Industrial & Engineering Chemistry Research, 2014. **53**(6): p. 2498-2508.
90. Walraven, D., B. Laenen, and W. D'haeseleer, *Comparison of shell-and-tube with plate heat exchangers for the use in low-temperature organic Rankine cycles.* Energy conversion and management, 2014. **87**: p. 227-237.
91. Alfa_Laval. *Brazed plate heat exchanger AC70X, Available: https://www.alfalaval.com/globalassets/documents/products/heat-transfer/plate-heat-exchangers/brazed-plate-heat-exchangers/ac/ac70x--ach70x.pdf*. 2016.
92. Alfa_Laval. *Brazed plate heat exchanger AC112, Available: https://www.alfalaval.com/globalassets/documents/products/heat-transfer/plate-heat-exchangers/brazed-plate-heat-exchangers/ac/ac112-ach112.pdf*. 2016.
93. Alfa_Laval. *Brazed plate heat exchanger CB200, Available: https://www.alfalaval.com/globalassets/documents/products/heat-transfer/plate-heat-exchangers/brazed-plate-heat-exchangers/cb/cb200--cbh200.pdf*. 2016.
94. Martin, H., *A theoretical approach to predict the performance of chevron-type plate heat exchangers.* Chemical Engineering and Processing: Process Intensification, 1996. **35**(4): p. 301-310.
95. Donowski, V.D. and S.G. Kandlikar. *Correlating evaporation heat transfer coefficient of refrigerant R-134a in a plate heat exchanger*. in *Engineering Foundation Conference on Pool and Flow Boiling, Anchorage, AK, Apr*. 2000.
96. Yan, Y.-Y. and T.-F. Lin, *Evaporation heat transfer and pressure drop of refrigerant R-134a in a plate heat exchanger.* Journal of Heat Transfer, 1999. **121**(1): p. 118-127.
97. Focke, W., J. Zachariades, and I. Olivier, *The effect of the corrugation inclination angle on the thermohydraulic performance of plate heat exchangers.* International Journal of Heat and Mass Transfer, 1985. **28**(8): p. 1469-1479.
98. Hsieh, Y.Y. and T.F. Lin, *Saturated flow boiling heat transfer and pressure drop of refrigerant R-410A in a vertical plate heat exchanger.* International Journal of Heat and Mass Transfer, 2002. **45**(5): p. 1033-1044.

99. Shah, R. and W. Focke, *Plate heat exchangers and their design theory.* Heat transfer equipment design, 1988. **227**: p. 254.
100. Alfa_Laval. *Brazed plate heat exchanger CB30, Available: https://www.alfalaval.com/globalassets/documents/products/heat-transfer/plate-heat-exchangers/brazed-plate-heat-exchangers/cb/cb30-cbh30_productleaftlet_che00025en.pdf*. 2016.
101. Thonon, B. and A. Bontemps, *Condensation of pure and mixture of hydrocarbons in a compact heat exchanger: experiments and modelling.* Heat transfer engineering, 2002. **23**(6): p. 3-17.
102. Thonon, B., R. Vidil, and C. Marvillet, *Recent research and developments in plate heat exchangers.* Journal of Enhanced Heat Transfer, 1995. **2**(1-2).
103. Han, D.-H., K.-J. Lee, and Y.-H. Kim, *The characteristics of condensation in brazed plate heat exchangers with different chevron angles.* JOURNAL-KOREAN PHYSICAL SOCIETY, 2003. **43**(1): p. 66-73.
104. Alfa_Laval. *Brazed plate heat exchanger CB10, Available: https://www.alfalaval.com/globalassets/documents/products/heat-transfer/plate-heat-exchangers/brazed-plate-heat-exchangers/cb/cb10-cbh10_productleaflet_che00021en.pdf*. 2016.
105. Alfa_Laval. *Brazed plate heat exchanger CB20, Available: https://www.alfalaval.com/globalassets/documents/products/heat-transfer/plate-heat-exchangers/brazed-plate-heat-exchangers/cb/cb20_productleaflet_che00024en.pdf*. 2016.
106. Alfa_Laval. *Brazed plate heat exchanger CB60, Available: https://www.alfalaval.com/globalassets/documents/products/heat-transfer/plate-heat-exchangers/brazed-plate-heat-exchangers/cb/cb60-cbh60_productleaflet_che00026en.pdf*. 2016.
107. Wanner_Engineering_Hydra_Cell. *Hydra cell pumps G25 Series, Available: https://www.hydra-cell.co.uk/docs/Sales-Lit-Extranet-Datasheets/G25-Datasheet.pdf*.
108. Ziviani, D., et al., *Characterizing the performance of a single-screw expander in a small-scale organic Rankine cycle for waste heat recovery.* Applied Energy, 2016. **181**: p. 155-170.
109. Zeleny, Z., et al., *Gear pump for low power output ORC–an efficiency analysis.* Energy Procedia, 2017. **129**: p. 1002-1009.
110. Macchi, E. and M. Astolfi, *Organic rankine cycle (ORC) power systems: technologies and applications*. 2016: Woodhead Publishing.
111. Lemort, V., et al., *Testing and modeling a scroll expander integrated into an Organic Rankine Cycle.* Applied Thermal Engineering, 2009. **29**(14-15): p. 3094-3102.
112. Lemort, V. and A. Legros, *Positive displacement expanders for Organic Rankine Cycle systems*, in *Organic Rankine Cycle (ORC) Power Systems*. 2017, Elsevier. p. 361-396.
113. Dumont, O., *Investigation of a heat pump reversible in an organic Rankine cycle and its application in the building sector*. 2017, Université de Liège, Liege, Belgique.
114. Dumont, O., R. Dickes, and V. Lemort, *Experimental investigation of four volumetric expanders.* Energy Procedia, 2017. **129**: p. 859-866.
115. Nikolov, A. and A. Brümmer, *Investigating a small oil-flooded twin-screw expander for waste-heat utilisation in organic rankine cycle systems.* Energies, 2017. **10**(7): p. 869.
116. Quoilin, S., et al. *Working fluid selection and operating maps for Organic Rankine Cycle expansion machines*. in *Proceedings of the 21st international compressor conference at Purdue*. 2012.

117. Lemort, V., I.V. Teodorese, and J. Lebrun, *Experimental study of the integration of a scroll expander into a heat recovery Rankine cycle.* 2006.
118. Hsu, S.-W., H.-W. Chiang, and C.-W. Yen, *Experimental investigation of the performance of a hermetic screw-expander organic Rankine cycle.* Energies, 2014. **7**(9): p. 6172-6185.
119. Quoilin, S., et al., *Thermo-economic optimization of waste heat recovery Organic Rankine Cycles.* Applied thermal engineering, 2011. **31**(14-15): p. 2885-2893.
120. Darvish, K., et al., *Selection of optimum working fluid for organic Rankine cycles by exergy and exergy-economic analyses.* Sustainability, 2015. **7**(11): p. 15362-15383.
121. Akyuz, E., et al., *A novel approach for estimation of photovoltaic exergy efficiency.* Energy, 2012. **44**(1): p. 1059-1066.
122. Kalogirou, S.A., et al., *Exergy analysis of solar thermal collectors and processes.* Progress in Energy and Combustion Science, 2016. **56**: p. 106-137.
123. Kurup, P. and C. Turchi, *Parabolic Trough Collector Cost Update for the System Advisor Model (SAM)*. 2015.
124. Mancini, T., et al., *Dish-Stirling systems: An overview of development and status.* Journal of Solar Energy Engineering, 2003. **125**(2): p. 135-151.
125. Poullikkas, A., G. Kourtis, and I. Hadjipaschalis, *Parametric analysis for the installation of solar dish technologies in Mediterranean regions.* Renewable and Sustainable Energy Reviews, 2010. **14**(9): p. 2772-2783.
126. Lecompte, S., et al., *Part load based thermo-economic optimization of the Organic Rankine Cycle (ORC) applied to a combined heat and power (CHP) system.* Applied Energy, 2013. **111**: p. 871-881.
127. OÜ_Cerbos. *Storage tanks, Available: https://www.cerbos.ee/en/20-storage-tanks*. 2019.
128. Zilmet. *Expansion Vessels, Available: https://zilmet.it/en/Expansion-vessels*. 2016.
129. Boyaghchi, F.A. and P. Heidarnejad, *Thermoeconomic assessment and multi objective optimization of a solar micro CCHP based on Organic Rankine Cycle for domestic application.* Energy conversion and Management, 2015. **97**: p. 224-234.
130. Ueckerdt, F., et al., *System LCOE: What are the costs of variable renewables?* Energy, 2013. **63**: p. 61-75.
131. Eurostat, *Electricity price statistics for household consumers, second semester, Available: https://ec.europa.eu/eurostat/statistics-explained/index.php/Electricity_price_statistics.* 2018.
132. Deb, K., et al., *A fast and elitist multiobjective genetic algorithm: NSGA-II.* IEEE transactions on evolutionary computation, 2002. **6**(2): p. 182-197.
133. Koza, J.R., *Genetic programming.* 1997.
134. Whitley, D., *A genetic algorithm tutorial.* Statistics and computing, 1994. **4**(2): p. 65-85.